Status and Prospect of *In Situ* and *Operando* Characterization of Solid-State Batteries

Marm B. Dixit [*] Jun-Sang Park[†] Peter Kenesei[†] Jonathan Almer[†]
Kelsey B. Hatzell [*‡§]

Manuscript Accepted At
Energy and Environemental Science
July 2021

[*]Department of Mechanical Engineering, Vanderbilt University, Nashville, TN, 37240, USA
[†]X-ray Science Division, Argonne National Laboratory, 9700 South Cass Avenue, Lemont, Illinois 60439, USA
[‡]Chemical and Biomolecular Engineering, Vanderbilt University, Nashville, TN, 37240, USA
[§]Department of Interdisciplinary Material Science, Vanderbilt University, Nashville, TN, 37240, USA, Email: kelsey.b.hatzell@vanderbilt.edu

Abstract

Electrification of the transportation sector relies on radical re-imagining of energy storage technologies to provide affordable, high energy density, durable and safe systems. Next generation energy storage systems will need to leverage high energy density anodes and high voltage cathodes to achieve the required performance metrics (longer vehicle range, long life, production costs, safety). Solid-state batteries (SSBs) are promising materials technology for achieving these metrics by enabling these electrode systems due to the underlying material properties of the solid electrolyte (viz. mechanical strength, electrochemical stability, ionic conductivity). Electro-chemo-mechanical degradation in SSBs detrimentally impact the Coulombic efficiencies, capacity retention, durability and safety in SSBs restricting their practical implementation. Solid | solid interfaces in SSBs are hot-spots of dynamics that contribute to the degradation of SSBs. Characterizing and understanding the processes at the solid | solid interfaces in SSBs is crucial towards designing of resilient, durable, high energy density SSBs. This work provides a comprehensive and critical summary of the SSB characterization with a focus on *in situ* and *operando* studies. Additionally, perspectives on experimental design, emerging characterization techniques and data analysis methods are provided. This work provides a thorough analysis of current status of SSB characterization as well as highlights important avenues for future work.

1 Introduction

Transportation accounts for 28% of greenhouse emissions in 2018 (1869 million metric tons of CO_2 equivalent) arising from combustion of fossil fuels[1]. Electrification of the transportation sector is crucial in order to achieve the emission goals set in place by the climate change agreement[2]. Numerous studies have showcased a high electrification potential (61 %) for the transportation sector[3,4,5,6,7]. Technology roadmaps for transportation electrification emphasize the need for next generation energy storage systems with high energy density anodes (Li, Si, and Na among others), high voltage cathodes (S and Nickel Cobalt Aluminium Oxide (NCA) among others) and optimized battery pack engineering[8,9]. Adoption of electric-mobility alternatives are contingent on the range offered, durability, charging times, and safety[9].

Over the recent years, introduction and diffusion of electric vehicles (EVs) in the automotive market has steadily increased to 7.2 million EVs in 2019, showing a 40% increase between 2018 and 2019[10]. These EVs are equipped with conventional Li-ion technology that employs a NMC (lithium nickel manganese cobalt Oxide) or NCA (lithium nickel cobalt aluminium oxides) cathode, graphitic anode, and a liquid electrolyte yielding a typical battery capacity between 5 - 95 kWh and ranges up to 300 miles[8]. US Department of Energy's Vehicle Technology Office projects 750 Wh/L cell packs (>1000 mAh/g anode, >300 mAh/g cathode, and >5 V cell voltage) for the next generation EVs[11,12]. Solid state battery (SSB) technologies employ a solid electrolyte (SE) that can leverage energy dense anodes and high voltage cathodes that offer a promising route towards realization of battery chemistries that can achieve the required performance metrics. Furthermore, transitioning to SSBs can significantly reduce battery pack volumes due to lower anode volumes and bipolar stacking which is crucial for automotive applications. To this end, SSBs are envisioned as a key technology for high energy density storage systems that can lead to an extended range of electric vehicles coupled with safer operations.

Conventional Li-ion battery systems have retained their basic architecture and material systems since they were introduced in the 1970s (Fig. 1a). These systems use a host material (e.g. graphite anode, layered cathode) to reversibly insert ions (Li^+) within their matrix during charging and discharging[13]. Traditional electrodes are solution-processed porous architectures with active material, electron conducting and binder additives which is flooded by liquid electrolyte[14]. On the other hand, SSBs replace the porous anode with a dense metallic alternative and the liquid electrolyte with a solid counterpart which leads to a significant decrease in the cell volume. SSBs employ a solid electrolyte that has comparable ion conduction properties to the liquid electrolyte and ion transference properties and relatively high mechanical strength. Similarly, composite cathode typically have dense architecture comprising of active material, ion conductor, electron conductor and binder matrix[15]. Transitioning from a conventional Li-ion architecture to an SSB with a metallic anode (viz. Li) can lead to almost a 3x increase in energy density[16].

Transport properties, electrochemical stability and scalable processing are key technological criteria for solid electrolytes that impact the adoption of SSBs. There are three different categories of solid electrolytes: (a) organic, (b) inorganic, and (c) hybrid (Fig. 1b-f)[17?] . Hybrid electrolytes are solid electrolytes comprising of a mixture of inorganic and organic solid electrolytes. Ionic conductivity of several material families are comparable to conventional

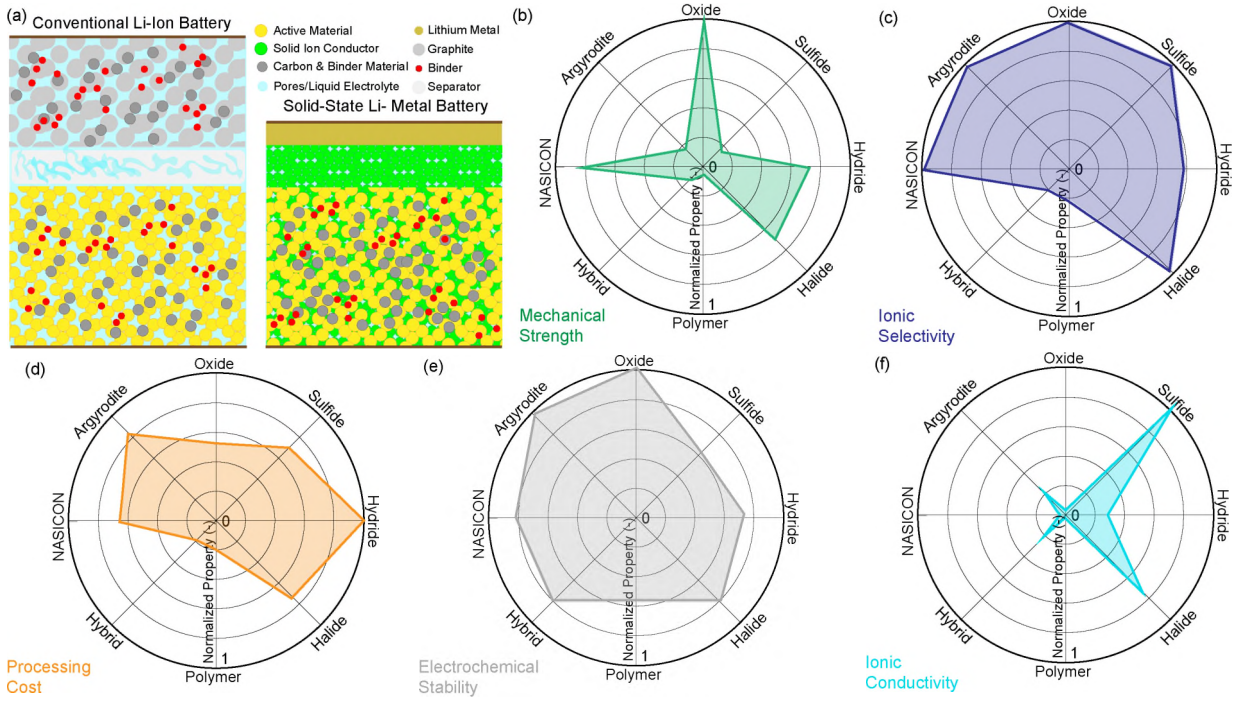

Figure 1: Solid-State Battery Technology Overview. (a) Schematic diagram showing differences in cell architecture between conventional Li-ion battery and solid-state Li metal battery. (b-f) Radar plot highlighting differences in material properties for a range of solid electrolyte materials. All physical quantities are normalized to one to enable comparison.

liquid electrolyte conductivities. Notably, room temperature conductivity of thio-LISICON type solid electrolyte ($Li_{10}GeP_2S_{12}$) is 12 mS cm^{-1}, with a low activation energy of 0.25 eV[18]. Argyrodites, perovskites, sulfides, anti-perovskites, NASICONs, and oxides have all shown mS cm^{-1} range ionic conductivities[19,20,17,21,22,23]. Most inorganic solid electrolytes show very high ion selectivity reflecting a transference number of nearly 1 (Fig. 1b-f). This decreases the presence of concentration gradients inside the battery and improves the rate performance of the system. In comparison, organic and hybrid electrolytes show comparably lower ionic conductivity ($\approx 10^{-3}$ mS cm^{-1} for polymer and $\approx 10^{-1}$ mS cm^{-1} for hybrid) and transference numbers ($\approx$ 0.1-0.5)[22]. Electrochemical stability is also typically higher for these solid electrolytes governed by their chemical affinity to lithium and stability against high voltage cathode material. Garnet oxides are typically most stable against lithium metal, while materials like sulfides and polymers generally undergo reduction reactions and form a mixed conducting interphase. Similarly, oxides are generally more stable against high voltage cathodes compared to other electrolyte materials. Inorganic solid electrolytes typically have significant processing costs due to multi-step and high temperature processing[23?] . Polymer and hybrid type SEs have lower processing and integration cost due to available commercial benchmarks for polymer manufacturing and assembly. Several other characteristics like mechanical properties (Young's modulus and fracture strength), electronic and ionic area specific resistance, thermal stability that dictate the electrochemical performance of the system show significant differences based on material family[24? ,25].

The goal of this review is to provide a summary of material challenges of today's SSBs

and - in particular - *in situ* and *operando* characterization tools to study these systems. The review is organized as follows. First, we summarize the materials challenge associated with SSBs and describe the key characterization techniques used today to address the challenge. We also describe the advantages and limitations of these techniques. The subsequent sections offer in-depth review of literature categorized by the type of characterization employed. This is followed by a section that describes the limitations of current *in situ* and *operando* measurements. We offer several recommendations on future experimental design and measurements. Subsequently, we have included a section on data analysis and analytics is provided that focuses on highlighting the need for leveraging characterization results above and beyond merely phenomenological representation. We emphasize on obtaining quantitative information from characterization and coupling of data-based and physics-based models to generate novel insights into material systems. The present review offers a comprehensive, critical summary of the current state of SSB characterization and identifies future directions for *in situ* and *operando* characterization of SSBs.

2 Material Challenges of Solid-State Batteries

Solid-state batteries rely on the ability to work with high energy density anodes (viz. Li), and high voltage cathodes to achieve techno-economic feasibility (Fig. 2a). Specifically, morphology control of anode during electrodeposition and electrodissolution is imperative in order to achieve high energy density batteries[16]. However, achieving ≈5 mAh cm^{-2} reversible cycling capacity at 5 mA cm^{-2} plating current density with high Coulombic efficiency is far from realization[26,27]. The primary concern with metallic anodes is their propensity to form filaments that grow through the electrolyte thickness causing cell failure[28,29,30,31]. Filament formation can significantly limit the rate performance, power density as well as Coulombic efficiencies of the solid state batteries[16,32]. In addition to filament formation, side reactions of anode with SE can lead to ionically insulating products as well as formation of electrochemically isolated anode (dead), both of which cause unrecoverable capacity loss[33,34,35]. In this context, interphase is defined as the region of SE|electrode interface that undergoes a chemical reaction to form a ternary phase. Interfacial kinetics of various anodes with SE is still a significant challenge limiting the high rate performance of the SSBs. High rate electrodissolution from the metallic anode can lead to formation of pores that can cause onset of failure[29,31]. Mass transport within the anode is also a key challenge and understanding creep and flow behavior of metallic anode is necessary to tune the performance of the system[36,37]. SE materials that show ion transport metrics (ionic conductivity, transference number) comparable to the state-of-the-art liquid electrolytes have been identified. However, their integration into high-performance battery packs is still far from realization[26]. Unstable transformation at the various solid|solid interfaces within SSBs contribute to non-optimal material utilization and poor ion transport. A wide range of SE materials are being investigated to maximize ionic conductivity, transference number and critical current density of the materials[20,38,22]. However, electro-chemo-mechanical degradation of the SE still remains one of the key concerns[39,34]. Operational stresses generated in the system from electrodeposition and electrodissolution of anode[40] and/or the composite cathode volume modulation[41] can lead to significant deterioration of the SE. Primary challenges associated with SEs are

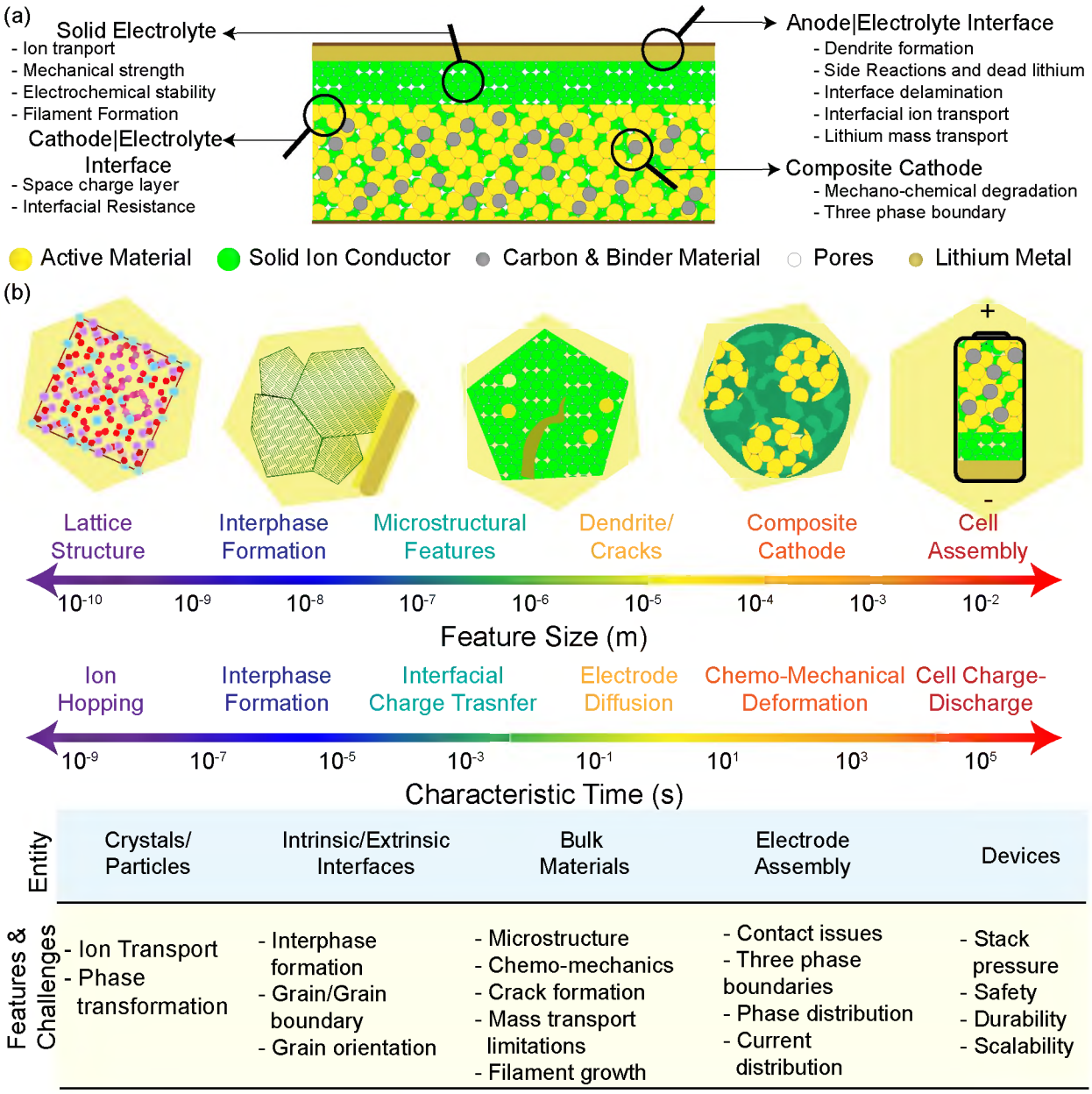

Figure 2: Summary of Challenges in Solid State Batteries. (a) Schematic diagram highlighting challenges at various components in a solid-state battery cell. (b) Temporal and spatial distribution of features and processes occurring in solid-state batteries. Physical entity in solid-state battery and corresponding features and challenges are also highlighted.

similar to those discussed for the anode and concern filament propagation[42,43,44,45]. Composite cathodes also offer significant challenges towards realization of high energy density solid state batteries[46]. Literature indicates the need for high active material loading cathode (>70 %) with areal capacities of 5 mAh m^{-2} [26]. The required composite cathode architecture for achieving a stable three-phase boundary within the cathode is largely unresolved. In contrast to conventional cathodes where the pores are filled with an ionically conducting liquid electrolyte, a composite cathode needs to function with a SE with its pores acting

as ion blocking domains[47,48]. Interfacial transport and kinetics of these solid|solid interfaces are largely unexplored[49,48]. Integration of high voltage cathode with solid electrolytes can lead to the formation of space-charge layers that can impede ion motion through the electrode|electrolyte interfaces[50,51,52,53].

While significant work has been carried out in the field of SSBs in the recent years, several fundamental challenges still need to be resolved. One of these is to understand the kinetic, transport, and chemo-mechanical responses of SSBs to cycling as well as dynamic external conditions (pressure, temperature). Characterizing and diagnosing these responses are pivotal for designing high-performance energy storage systems. A majority of these challenges are manifested at the multitude of solid | solid interfaces occurring in solid state batteries (SSBs): (i) anode | electrolyte, (ii) cathode | electrolyte, (iii) active material | electrolyte | carbon, (iv) solid electrolyte | defect/void, among others. A fundamental understanding of interfacial design with regards to these physical processes is needed to rationally engineer a high performance SSB.

3 Characterization Challenges for Solid-State Batteries

As noted in the earlier section, SSBs exhibit a variety of chemical, mechanical and electrochemical transformations both at quiescent and operating conditions[16]. *Ex situ* characterization can provide global information regarding system state and material transformations within SSBs. While this information can provide global understanding of degradation and failure mechanisms, *in situ* and *operando* measurements are required to understand the onset and growth of such mechanisms[? ?] . In addition, dynamic processes occurring in batteries are typically in the ms time scale, and only under certain electrochemical boundary conditions making it difficult to capture in ex-situ conditions. For these reasons, it is important to pursue *in situ* and *operando* characterization of SSBs. Most transformations which limit the performance of SSBs occur at the electrode | electrolyte interfaces. These solid | solid interfaces are difficult to probe experimentally and are thus referred to as 'buried interfaces'. Buried interfaces can be probed using a range of techniques and characterization tools. However, all characterization techniques operate with limited temporal and spatial resolutions and are compatible with materials showcasing specific properties(Table 1). SSBs consist of a range of materials and associated properties, often with multi-dimensional gradients, making experimental characterization challenging. The cascading length- and time-scales associated with the physical processes at these interfaces make them extremely challenging to investigate (Fig. 2b). Length-scales considered in SSBs range from nano-scale (lattice structure, interphase formation), micro-scale (grain structure, porosity), to the meso-scale (component assembly, cathode architecture). These materials can have markedly different degrees of long- and short-range order (from amorphous to crystalline), refractive indices, densities, optical transparencies and electronic conductivities, and these differences can dictate the effectiveness of a given characterization technique (Fig 3a). Material structure and properties as well as their evolution have to be match the contrast mechanism employed by the characterization technique (Fig. 3b). Additionally, constraints regarding sample ge-

ometry and working environments dictate what techniques can be used to study particular phenomena. It should be noted that significant work has been carried out in characterization of conventional battery systems. However, the material differences (gravimetric density, electronic density, absorption contrast, elemental make up, among others) between liquid electrolyte and solid electrolyte typically render direct translation of technical know-how from conventional batteries to SSBs difficult. As an example, a sample environment for in situ TEM measurements for conventional batteries cannot be used for solid-state batteries directly, or X-ray energy used for imaging a conventional cell could potentially not work for a solid-state battery cell. While underlying mechanisms can prove similar, it is generally found that application of a characterization technique used in conventional batteries to solid-state battery system requires modifications of experimental cell design, operating parameters and acquisition conditions.

In this review we focus on non-destructive microstructural characterization techniques which can be classified into three major categories: (a) real-space imaging, (b) reciprocal space characterization, (c) spectroscopy/others (Fig. 3c). Imaging techniques use reductions in incident beam intensity to directly map the material density/morphology and are used most widely of the three techniques. Reciprocal space techniques use the scattered signals to acquire information on the scattering entity such as constituent crystal structure, strain, and phase. Scattering techniques like X-ray diffraction (XRD) are extensively used for for *ex situ* structural characterization, and have hitherto seen limited application in *in situ*/*operando* measurements for SSBs. It should be noted that while conventional scattering techniques are used for probing bulk material properties, appropriate instrumentation and analysis tools can be leveraged to retrieve spatial information from scattering techniques[54,55]. Spectroscopy technique measure the energies of particles that are absorbed or emitted by the sample and is often used to characterize the electro-chemical state of the sample or probed region. Over the years, significant advancement has been made in characterizing physical and chemical transformations at solid|solid interfaces from optical images to techniques like atom-probe tomography[56,57].

Optical/scanning electron microscopy techniques have been extensively used for imaging of the solid state battery systems[58?,59,34,60,30]. The optical cell can be used for planar/sectional imaging of the solid state battery and can resolve μm-scale features. Synchronizing electrochemical signatures during cycling to *operando* optical microscopy can provide insights into growth and morphology of Li filaments[61,59,60]. Optical cells are generally easier to construct and are economical. However, optical studies require the material to be transparent/translucent in the visible light spectrum which is typically only possible with a small number of solid electrolyte materials. Smaller spatial features (micron to nm- level) are investigated through scanning/transmission electron microscopy (SEM/TEM)[62]. SEM images are generated by capturing reflected/knocked off electrons from the sample surface and thus can provide information regarding morphological features of the investigated material. Similar to SEM, TEM provides morphology information but down to a smaller (sub-nm) length scale. TEM images are generated by capturing electrons transmitted through the sample. TEM can inform information related to material morphology and local atomic configurations. Experimental geometry and sample preparation differs drastically between different imaging approaches (optical, electron, X-ray). Energy dispersive spectroscopy (EDS)[63] and focused ion beam milling (FIB)[64] can provide additional elemental and three dimensional

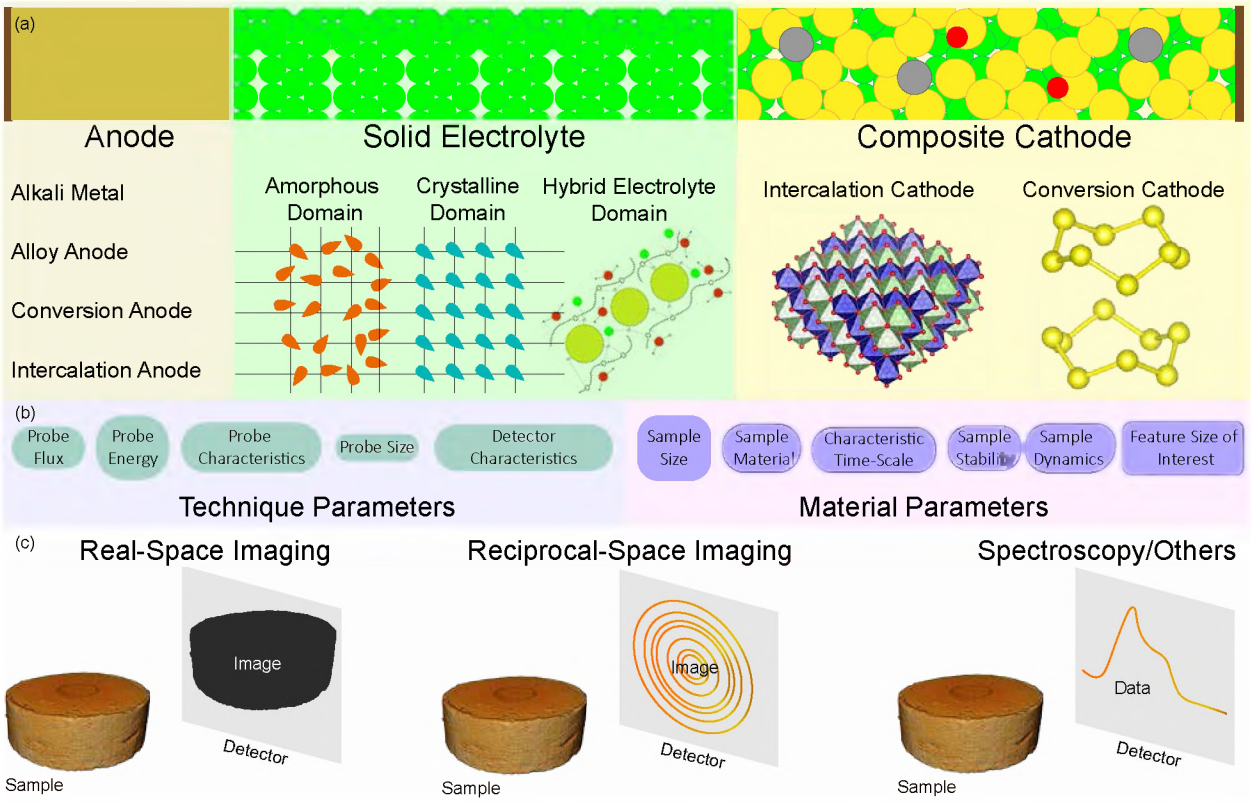

Figure 3: Overview of characterization techniques to study SSBs. (a) Schematic diagram showing material types for different components of the solid state battery. (b) Sample and technique parameters that influence measurement. (c) Schematic illustrating non-destructive SSB characterization techniques.

information regarding the sample. However, the latter is a destructive technique and cannot be employed for *in situ* or *operando* tests. TEM can also be coupled with EDS as well as other analytical tools like selected area electron diffraction (SAED)[65] or electron energy loss spectroscopy (EELS)[66] that can provide information about structure and chemical moieties of the sample over and above the morphological information. The key challenge with microscopy studies is developing a technique compatible with an *operando* solid state battery cell. Planar and sectional batteries, as well as particle-scale electrochemical cells are investigated with optical as well as scanning electron microscopy. *In situ* and *operando* studies on TEM are carried out on thin film batteries as well as using custom built biasing cells. Adequate care needs to be taken in design of SSB systems for microscopy studies to ensure that the field profiles in the *in situ* cells resemble the anticipated field patterns in a laminar battery cell. Edge and surface effects at the electrode|SE interface can significantly alter the local field configurations dictating the observed electrochemical performance. TEM, SEM, and optical microscopy cover a wide range of spatial length scales from atomic to macroscopic.

Table 1: Summary of relevant diagnostic tools for solid state batteries

Technique	**(Spatial)/ (Temporal) Resolution**	**Mechanisms**	**Attainable Sample Size**	**In-situ or Ex-situ**	**Ref.**
Optical Microscopy	(≈10 μm)/ (1-10 s)	Morphology, electrodeposition/dissolution	≈3-5 mm	*In situ*	58
Scanning Electron Microscopy	(10 nm)/ (1-10 s)	Morphology, Chemical Composition, Electrodeposition/dissolution	≈1 mm	*In situ*	67
TEM	(<1 nm) / -	Morphology, Chemical Composition, Interface stability	≈100 nm	*In/ex-situ*	62
Electron Holography	(<1 nm) / -	Electrostatic Fields	≈100 nm	*In/ex-situ*	68
Atom Probe Tomography	(<1 nm) / -	Chemical composition	≈100 nm	*Ex-situ*	69,70
Synchrotron Tomography	(0.5 μm)/ (1-10 min)	Morphology, electrodeposition/dissolution	≈3 mm to macro-scale objects	*In/ex-situ*	71,72
Benchtop Tomography	(10-20 μm)/ (10-60 min)	Morphology, electrodeposition/dissolution	≈mm-cm	*In/ex-situ*	73
Neutron Tomography	(30-40 μm)/ (7-8 hours)	Morphology, electrodeposition/dissolution	≈10 mm	*In/ex situ*	74
TOF-SIMS	(≈200 nm) /-	Chemical composition, interfacial Stability	≈50x50 μm^2	*Ex-situ*	75,76
Neutron Depth Profiling	(≈10-15 nm)/ (1-10 min)	Li concentration, electrodeposition/dissolution	8-10 mm	*In situ*	77
NMR/MRI	(200+ μm)/ (10s min)	Li concentration, electrodeposition/dissolution	≈4-5 mm	*In situ*	78
Atomic Force/Scanning Probe Microscopy	(≈1-10 nm)/ (1-10 min)	Mechanical properties, interface stability	≈200x200 μm^2	*In situ*	79
XRD	(2.5 μm)/ (1-10 min)	Phase, Lattice Structure, interface stability/strain	≈3-5 mm to macro-scale objects	*In/Ex situ*	80

X-rays interact with materials proportionally to the electron cloud density resulting in minimal interaction with low Z elements and strong interactions with high Z elements[81]. X-rays can be used for all three characterization categories: (i) imaging, (ii) scattering, and (iii) spectroscopy[82]. Traditional X-ray imaging typically leverages absorption or (for partially or fully coherent synchrotron sources) phase contrast mechanisms to enable reconstructions of three dimensional structures of the probed material[83]. Depending on the X-ray energy, flux and optics, resolution from μm[71,84,85] down to nm range[79,86] can be obtained. Scattering methods typically probe materials and yield structural information in reciprocal space. X-ray diffraction (XRD) is a scattering technique that probes the Bragg reflection peaks for ordered, crystalline materials within a material system and provides information regarding structure and phase of the material investigated[87]. XRD at synchrotrons can provide spatially and temporally resolved information within the samples[88]. XRD combined with tomographic data acquisition, often referred as diffraction tomography or scattering tomography, can be used to assess three dimensional phase distribution within the investigated battery materials[89]. X-ray spectroscopy (XPS) is widely used to investigate the local coordination environment of materials using absorption, florescence or photo-electron spectroscopy[90,91,92,93]. X-ray absorption spectroscopy (XAS) yields insight into oxidation state, site symmetry, bond strength, short-range local structure, coordination number, bond distances and nearest neighbor atom identities. X-ray photo-electron spectroscopy, similarly can provide insight into surface composition, near surface variation composition, and oxidation state[94]. While some soft X-ray spectroscopy requires ultra high vacuum (UHV) conditions, there is a potential for studying materials in near ambient conditions with a variety of environments with ambient pressure XPS[95]. The ability to select the wide X-ray energy available from syncrhotron sources with a suitable monochromator enables X-ray Absorption Fine Structure (XAFS) or X-ray absorption near edge structure (XANES) that can provide spatially-resolved elemental information[96].

Typically, neutron experiments are analogous to X-ray scattering and imaging experiments but with significant longer data acquisition time. X-ray and neutron diffraction are extensively used in complementary fashion for structure determination of novel materials[97,98,99]. Small angle and wide angle neutron scattering (SANS, WANS) are also used in conjunction with isotope labelling to investigate polymer structures for organic electrolytes[100]. Quasi-elastic neutron scattering (QENS) is a relaxation technique used extensively to probe ion diffusion pathways in solid electrolytes[101,102]. Neutron imaging typically shows lower resolution compared to X-rays but improved chemical specificity and larger field of view makes it a highly desirable technique especially for low -Z elements due to non-linear scattering cross-section[103,104]. Further, the scattering cross-section is isotope dependent with different element isotopes showing vastly different scattering cross sections (^{6}Li = 2.00-0.261i, ^{7}Li =-2.22). Neutron reflectometry (NR) is a technique that is used to ascertain scattering length density with nm-scale depth precision. Reflectometry profile shapes can provide information regarding the thickness, density, and roughness of thin film architectures. NR has been used to extensively to investigate solid electrolyte interphase in conventional Li-ion batteries[105,106,107,108], however has so far seen limited use in SSBs. A similar technique, neutron depth profiling (NDP) is used extensively in the solid state battery community[109,110]. Thermal neutrons are bombarded on a planar sample, and the charged particles emitting from the interaction of neutron with ^{6}Li (α and ^{3}He) are detected and energy discriminated. Between

production and detection, the emitted charge particles lose energy due to interaction with the sample. Sample knowledge and stopping power can be used to computationally obtain depth profile density with the obtained energy spectrum with nm precision.

In situ and *operando* characterization of SSBs require careful experimental design both in terms of material/cell design and the experimental setup. The broad overview of techniques provided here is expected to highlight the applicability and limitations of key characterization techniques. Subsequently, this review discusses results from the current state-of-the-art characterization tools for solid state batteries. As discussed earlier, characterization technique are divided into three categories : (a) real space, (b) reciprocal space and (c) spectroscopic studies. The structure of the review follows these categories with an additional section for techniques that did not strictly fall into these categories. Real space characterization is further divided into direct imaging (optical, SEM/TEM, X-Ray Tomography (XRT) and indirect imaging (neutron depth profiling, atomic force microscopy, scanning probe microscopy) depending on how the information is obtained from the characterization method. Spectroscopic techniques are divided into absorption, photoelectron, RAMAN and NMR spectroscopy sections.

4 Real Space Imaging

4.1 Optical Microscopy

Optical microscopy is typically carried out under two configurations: (a) through-plane and (b) in-plane (Fig. 4). Depending on the configuration, the electric field lines through the system can be significantly different which can impact the electrochemical behavior of the cell (Fig. 4c). In the case where electrodes are significantly smaller than the electrolyte diameter/thickness through-plane and in-plane configurations show similar field concentration at the electrode edges[30]. However, in most practical cases electrode size is comparable to electrolyte diameter, leading to minimal edge effects in through-plane configurations with planar field lines. It is vital to elucidate and differentiate geometry effects from inherent material response for reliable interpretation of experimental data. Through plane visualization suffers from several experimental challenges. Primarily, inhomogenities associated with edge-effects lead to localization of failure features near the viewing edge. Additionally, in order to achieve adequate signal thick electrolyte layers must be used, which are typically not employed in realistic applications. To overcome these challenges, filament formation was studied *in situ* using an in-plane orientation for the Li | $Li_7La_3Zr_2O_{12}$ (LLZO) | Li system. The study revealed several nuances of Li penetration in garnet solid electrolytes[30]. Several different morphologies of Li filaments were identified (straight, branching, spalling, and diffused) suggesting multiple mechanisms at play in filament formation (Fig. 4d). These studies showcased the reversibility of filaments as well as mechanisms through which dead lithium was formed. A similar study identified local deposition of Li metal which generates high local stresses leading to the mechanical cracking of the electrolyte (Fig. 5c)[112]. Li filament propagates through the extending crack and leads to short-circuit of the cell. It was proposed that high local currents in the filament lead to Joule heating and melting of the Li metal which can disperse in form of droplets. The melting and droplet formation mechanism

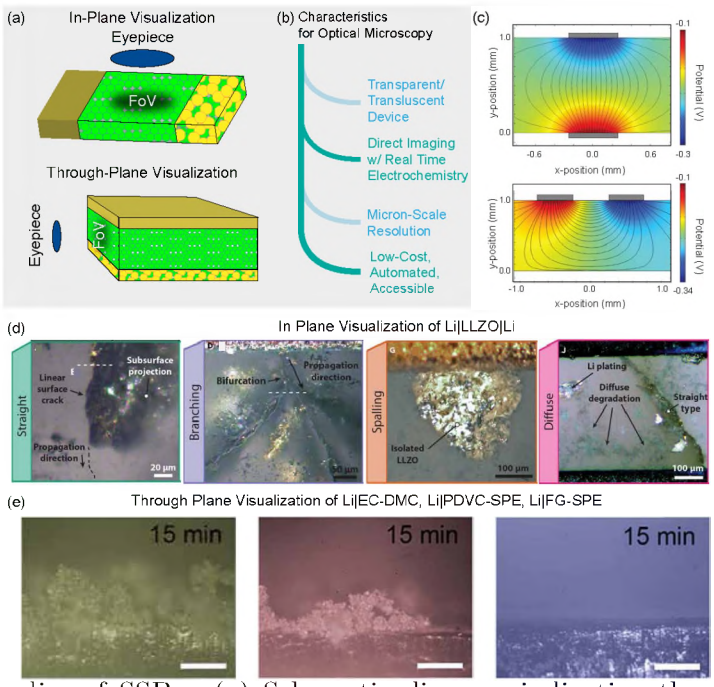

Figure 4: Optical studies of SSBs. (a) Schematic diagram indicating the two key architectures for optical studies. (b) Characteristics for optical microscopy. (c) Field effects for in-plane and through-plane configuration of investigation. Reprinted from[30] with permission from Elsevier. (d) In-plane optical images of straight, branching, spalling and diffuse type of filament growth in garnet solid electrolytes. Reprinted from[30] with permission from Elsevier. (e) Optical microscopy of Li deposition at 4 mA cm^2 on bare Li foil, diallyl carbonate (DAC)/vinylene carbonate (VC) based solid polymer electrolyte (PDVC) covered Li foil and a functionally graded solid polymer electrolyte covered Li metal (left to right). All the scale bars in the image are 100 μm. Reproduced from[111] with permission from The Royal Society of Chemistry.

was proposed as a root mechanism for unstable voltage profiles observed in plating/stripping experiments. Both studies indicate that filament growth was preceded by a crack-opening mechanism and dendrite growth rate was proportional to the current density consistent with the results from PEO-Li model systems and Chazalviel model[113]. Similar Li morphologies were identified in LPS solid electrolytes indicating an underlying fundamental mechanism dictating Li morphology evolution in solid electrolytes. Optical microscopy was also used to assess filament growth and fracture mechanisms of four types of solid electrolytes, glassy LPS, β-Li_3PS_4, polycrystalline and single-crystal Ta-doped $Li_7La_3Zr_2O_{12}$ (LLZTO)[60]. Glassy LPS did not show filament penetration through solid electrolyte thickness up to 5 mA cm^{-2}. In contrast, other materials showed filling and propagation of lithium filled cracks that were generated at surface defects. Experiment and modelling results indicate that Li plating over-potentials above a certain current density at surface defects can create mechanical stresses high enough to fracture the solid electrolyte material. A Griffith-like failure was proposed for brittle solid electrolytes. For Li|LPS system, interfacial cracks were identified in the solid electrolyte layer during electrodeposition at 2 mA cm^{-2}[67]. This behavior was consistent with a Griffith-like failure mechanism wherein a buried flaw in the SE could precipitate the crack formation at the interface. In addition to understanding Li filament growth, optical microscopy was also used to visualize Li plating morphology in certain cases. Li plating

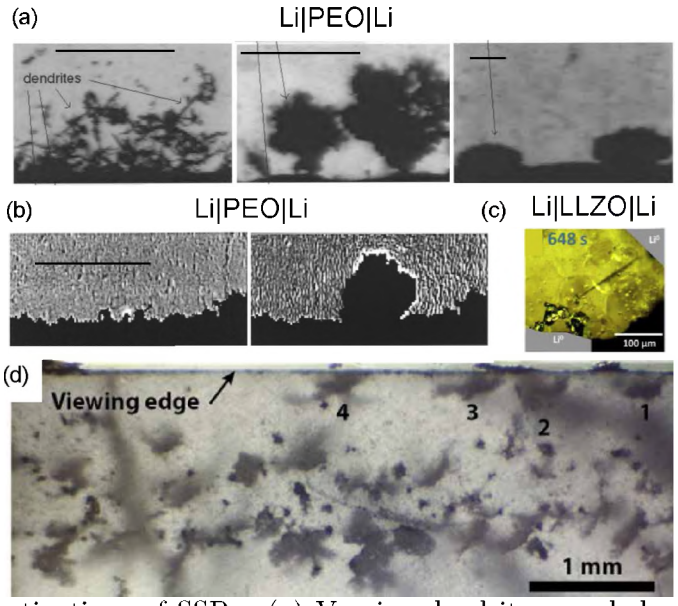

Figure 5: Optical Investigations of SSBs. (a) Varying dendrite morphology observed at different current density of 0.2 (needle-like), 0.7 (tree-like) and 1.3 (bush-like) mA cm^{-2}. The scale for the three figures are 950 µm, 420 µm and 200 µm from top to bottom. Reprinted from [113] with permission from Elsevier. (b) Concentration gradients at dendrite tips formed at 0.7 mA cm^{-2}. Dendrites are darker features, while the polymer electrolyte is the regions with lamellar features. Differences in contrast at the edge of the dendrite are attributed to concentration gradients. Reprinted from [115] with permission from Elsevier. (c) Optical microscopy of LLZO pellet with Li foil contacts (grey colored) during a long term stripping experiment. Reprinted from [112] with permission from Elsevier. (d) Shorted Li|LLZO|Li cell investigated by optical microscopy. Reprinted from [30] with permission from Elsevier.

morphologies in $Li_{1.3}Al_{0.3}Ti_{1.7}(PO_4)_3$ (LATP)| Li_3PO_4N (LiPON)|Cu cell show marked difference in morphology based on current density with the same quantity of plated Li (18 mC, 0.13 μm)[114]. At 5 μA cm^{-2}, plated lithium shows needle-like features at localized spots. Increasing the current density increases the coverage ratio as well as reduces the size of the plated Li features. Nucleation of Li on copper was identified as the rate determining step dictating the kinetics of the electrodeposition as observed from the voltage profiles during *operando* optical microscopy. Tailoring electrolyte composition can help stabilize Li deposition as evidenced by application of a functionally graded solid polymer electrolyte with Li metal (Fig. 4e)[56]. The functional gradient electrolyte comprises of ceramic and polymer-rich phases with the ceramic rich phase offering physical suppression to dendrite propagation as well depolarization effects to stabilize electrodeposition. Optical microscopy offers a unique avenue for characterization of optically transparent/translucent materials. Synchronous electrochemical measurements coupled with video microscopy and careful experimental design can generate important insight into the morphological evolution in solid-state batteries.

Some of the earliest work on characterization of solid-state batteries was carried out on Li-Polymer systems by optical microscopy[58,116,113,115,117,118]. Using a model PEO-LiTFSI system, dendrite formation in polymer system at low current densities was shown to occur at Sands time reflecting the time at which ion depletion at the negative electrode (Fig. 5a-b). At high current density, a local heating of the electrolyte was proposed that accelerates failure.

The dendrite propagation velocity in these measurements correlated with anion drift velocity and current density as predicted by Chazalviel[117]. Concurrent growth of several dendrites at similar velocity was anticipated. However, only one dendrite typically grows through the electrolyte thickness shorting the cell. Other dendrites typically show more in-plane growth. These studies also highlighted the implications of non-uniformity at the Li|SE interface resulting in local hot-spots of current density even while operating with low external circuit current. Additionally, using equivalent modelling of impedance spectra equivalent dendrite resistance in PEO systems was estimated as 30 mΩ[113]. Using an identical technique, several other studies have investigated dendrite formation in variety of solid electrolytes. Li powder electrodes were shown to possess improved dendrite suppressing capabilities than Li foils[119]. Surface treatment of Li powder with LiF and Li_2O_3 leads to additional improvements in rate performance and dendrite suppression. LiF and Li_2O_3 act to provide a stable, ionically conductive interphase leading to the improved performance. Filament formation in garnet oxide solid electrolytes was investigated with a similar sectional optical microscopy setup. Li penetration in the solid electrolyte was consistent with a voltage drop during galvanostatic charging as a result of three factors: (a) increase in interfacial area due to growth of dendritic growth leading to lower interfacial resistance; (b) decrease of inter-electrode distance and (c) formation of kinetically faster interfaces (Fig. 5d)[30].

4.2 Electron Microscopy

Scanning and transmission electron microscopy provides atomic and nano-scale imaging resolutions which makes these techniques ideal for interfacial characterization of solid-state batteries (Fig. 6a-b). With recent developments of techniques like high resolution TEM (HRTEM), high angle annular dark-field (HAADF) imaging, annular bright-field (ABF) imaging, electron energy-loss spectroscopy and electron holography (EH) information regarding chemical profiles, valency, local electric field can be obtained in addition to information regarding material structure and morphology. SEM/TEM measurements are extensively utilized for materials characterization due to their ease and availability. Herein, we include a discussion of some of the key representative results that are assessed by electron microscopy techniques mostly in *in situ* and *operando* conditions. Several recent reviews offer a thorough discussion of *ex situ* characterization of SSBs by electron microscopy methods[123,124,125]. SEM techniques are widely used to assess Li metal morphology due to the relatively low experimental effect of e- beam to Li[120,126,127,128]. *In situ* visualization of an all-solid LFP|PEO-LiTFSI|Li battery showed formation of Li dendrites as well as dead Li during electrochemical cycling (Fig. 6c)[120]. After extended cycling, a vastly different morphology of Li was observed from the pristine interface with new edges wherein polymer degradtion and filament growth was seen to progress successively into the cell. Grain boundaries in Li were identified as hot-spots where dendrites/dead Li forms. Dendrite formation was linked with decomposition of the polymer due to melting, reduction and thermal runaway. Isles in Li metal were also identified at high cycling rates that were isolated from the rest of the anode due to salt decomposition and increased activity in local regions. Thermal degradation of polymer electrolyte was also observed during Li filament formation previously[129]. High local currents that cause filament formation can also contribute to Joule heating and thermal degradation. Differences in morphology of electrodeposition and electrodissolution

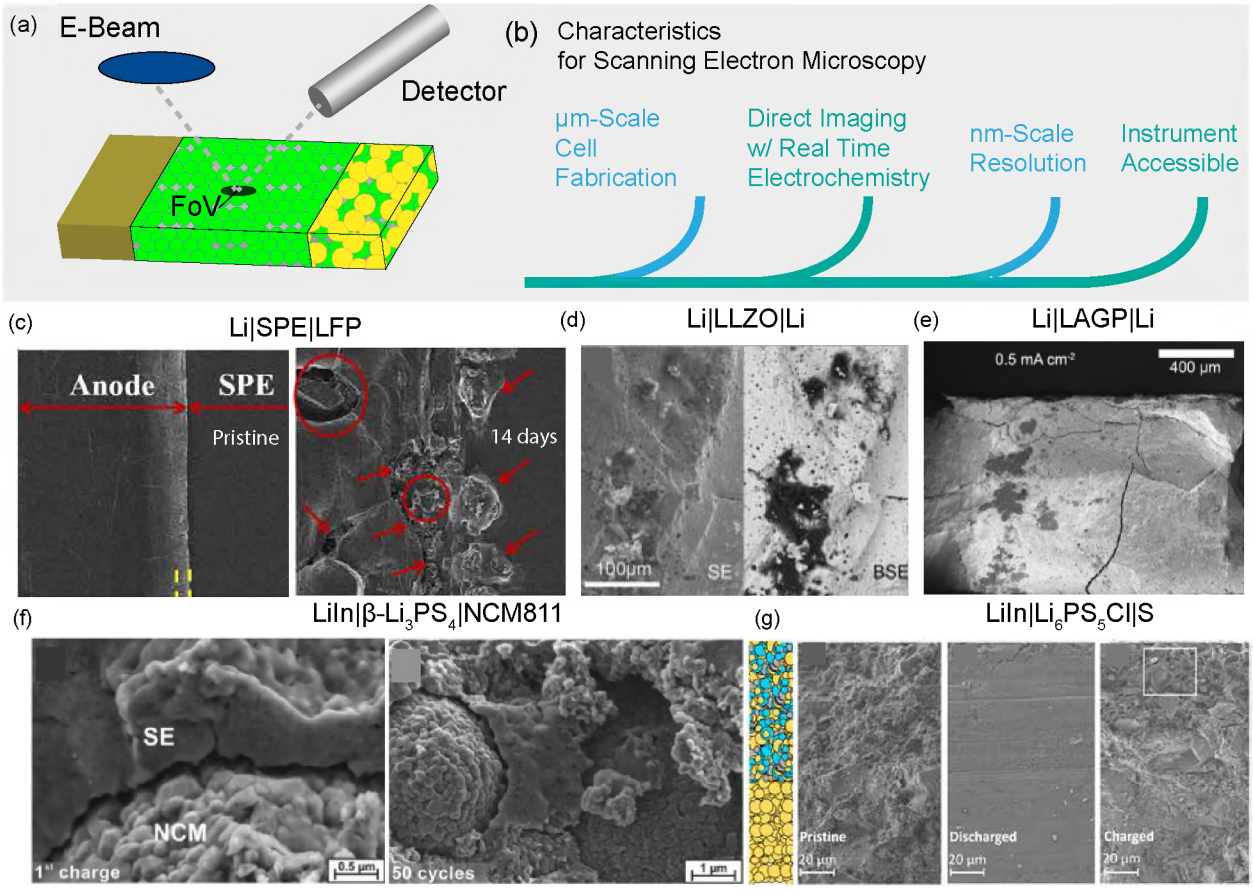

Figure 6: Summary of SEM studies in solid-state batteries. (a) Schematic diagram for SEM studies. (b) Characteristics for SEM investigations. (c) *in situ* SEM images of Li plating in a LFP|Polyether-LiTFSI|Li cell. SEM images are shown for pristine and after 14 days of cycling. Cycled samples show dendrites on the newly formed edge. All scale bars in the images are 100 μm. Adapted from[120] with permission from Springer. (d) Filament growth in Li|LLZO|Li system imaged with second electron (SE) and back-scattered electron (BSE) mode to differentiate Li deposition. Regions with darker contrast in BSE mode reflects the enrichment of lighter elements. Adapted from[61] with permission from Elsevier (e) Cross-sectional image of Li|$Li_{1+x}Al_xGe_{2-x}(PO_4)_3$ (LAGP)|Li cell cycled at 0.5 mA cm^{-2}. Extensive crack formation in LAGP electrolyte is observed as well as formation of reacted interphase (darker regions) is identified. Adapted with permission from[34]. Copyright 2019 American Chemical Society. (f) SEM image of degraded composite cathode of NCM811 and -Li_3PS_4 after 50 cycles. Adapted with permission from[121]. Copyright 2017 American Chemical Society. (g) SEM cross-section images of the pristine, discharged, and charged Li_6PS_5Cl/S-C-Li_6PS_5Cl cell. Adapted with permission from[122]. Copyright 2019 American Chemical Society.

of Li was investigated for LiPON|Cu interface[114]. At low current density (50 μA cm^{-2}), electrodeposited Li was distributed sparsely with a local growth rate of 6.8 mA cm^{-2}. At low stripping currents (50 μA cm^{-2}), no preferential stripping of electrodeposited Li was observed. At higher stripping currents, root regions of electrodeposited Li was preferentially removed leading to formation of dead Li and an overall Coulombic efficienty of 18 %. Cathode and Li morphology were tracked in an *in situ* SEM experiment for S|Polyether-LiTFSI|Li cell[130]. Cathode discharge products were observed as needle-shaped deposits that grow preferentially at electrode|interface. This leads to an increase in porosity of the cath-

ode which accelerates the failure. Lithium metal growth observed in the cell was consistent with the active material loading of the cathode. Contrast difference in electrolyte indicated irreversible dissolution of S species into the electrolyte leading to capacity decay of the cell.

In situ microscopy imaging also revealed kinetics of LLZO | Li interfaces[131]. Electrons are bombarded on the exposed LLZO surface in a Li|LLZO cell to develop a potential difference between the top and bottom surface of LLZO which can cause deposition of Li on the top surface of the solid electrolyte. This investigation indicated that fundamental kinetics of the LLZO|Li interface were extremely rapid with a local current density of several hundred mA cm^{-2}. Additionally, preferential deposition of Li along grain boundary as well as edge-features in the LLZO surface was observed. Minimization of 1D and 2D defects at the anode interface were proposed to enable stable electrodeposition of Li metal. Li/80Li_2S.20P_2S_5 SE/SS at 2 mA cm^{-2} shows local crack formation at the current collector | solid electrolyte interface through which Li filaments grow on shorting[67]. Cracks were focused in the regions where stainless steel (SS) current collector contacts the solid electrolyte. The authors propose that Li migrates through grain boundaries in the solid electrolyte and the soft solid electrolyte deforms to allow Li filament to grow through the thickness. These results suggest that in addition to controlling the anode|SE interface, the current collector|Li interface needs careful design to enable stable electrodeposition. *Ex-situ* SEM is mostly used to for postmortem analysis of solid state batteries to investigate features like electrodeposition morphology, electrolyte fracture as well as cathode microstructure (Fig. 6b-g). Li deposition in LLZO was evidenced by differing contrast mechanism in SEM imaging with back-scattering electron (BSE) mode showing higher contrast for low atomic number elements compared to second electron mode (Fig. 6d-e). Li deposition in LLZO was clearly identified by ex-situ SEM and filament formation was proposed to proceed through grain boundaries and inter-connected pores[61]. Similar filament formation and Li -rich pores were observed in top-view and cross-section images of LLZO solid electrolyte (Fig. 6d)[59]. Similarly, Li deposition in pores was attributed to degradation of Garnet oxides. Li deposition within the solid electrolyte can occur if the solid electrolyte exhibits trace electronic conductivity. Electron migration from the lattice (trace electronic conductivity) or by reduction of the oxygen sub-lattice were two possible sources of electron donation. In comparison to LLZO, $Li_{1+x}Al_xGe_{2-x}(PO_4)_3$ (LAGP) shows a more dramatic fracture mechanism with extensive crack formation (Fig. 6e)[34]. Darker regions in the cross-sectional image of the SE reflect the unstable interphase growth in LAGP. Non-uniform growth of this interphase can cause localized stress hot-spots that accelerate mechanical failure of the solid electrolyte. Unstable interphase generation at Li|LAGP interface was identified as a root cause for failure during electrochemical operation. SEM imaging is also used to investigate composite cathode microstructure evolution as the origin for capacity decay (Fig. 6f-g). Most composite cathodes suffer from chemo-mechanical degradation arising from electrochemical expansion/contraction of the active material[122,125,132,133,121]. The mismatch in mechanical properties of the constituents of composite cathode leads to stress concentrations and results in delamination, cracking and fracture of the composite cathode. FIB-SEM tomography of the composite cathode further highlights the importance of tailoring cathode microstructure and three phase boundary to improve rate performance and durability of the SSB[134].

TEM offers $\mathring{A}$ level resolution with ability to resolve chemical phase information and morphological evolution in SSBs (Fig. 7a-b). Typically, TEM requires extensive sample

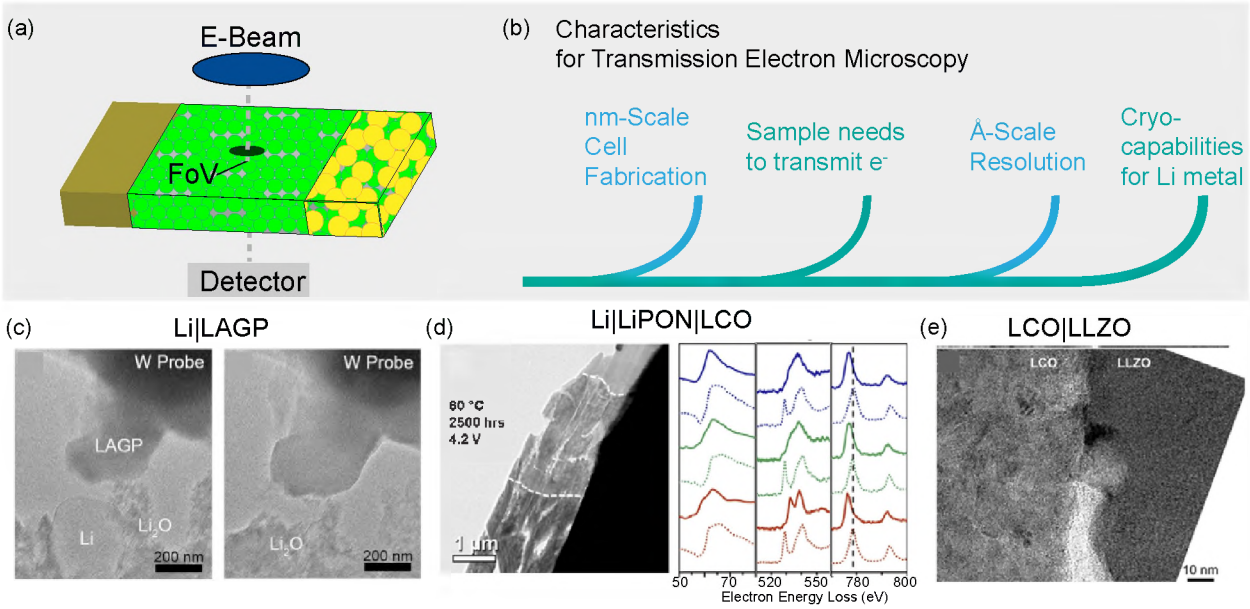

Figure 7: Transmission electron microscopy studies for solid-state batteries. (a) Schematic diagram for TEM investigations. (b) Characteristics of TEM investigations. (c) Image of an unreacted LAGP particle before contact with lithium. (e) TEM investigation of LAGP interphase formation. Pristine and reacted LAGP shows LAGP particle expansion and reduction of lithium volume upon contact. Adapted with permission from[34]. Copyright 2019 American Chemical Society. The particle expanded in volume and the lithium crystal disappeared. (d) Interphase growth at $LiCoO_2$ (LCO)|LiPON interface. TEM image of cell aged at 60 °C for 2500 h show growth of around 3 μm thick interphase. Electron loss energy spectra at Li-K/Co-M, O-K and Co-L edges. Reprinted from[135] with permission from Elsevier. (e) Interphase formation at LCO|LLZO interfaces observed by TEM. Adapted with permission from[136]. Copyright 2018 American Chemical Society.

preparation to ensure reliable data retrieval during measurement. TEM is highly versatile with a range of operating modes and configurations (Cryo-, SAED, EDS). This range makes it an excellent tool for probing solid|solid interfaces in SSBs. *In situ* testing of LAGP|Li system showcases the formation of interphase in LAGP[34]. The SE particle undergoes a 38% expansion on passive lithium contact, with a corresponding decrease in Li metal volume (Fig. 7a). These results showcase Li diffusion into the SE and formation of interphase on the SE particle. Selected area electron diffraction (SAED) pattern of uncontacted and reacted SE particle shows an amorphous reacted material compared to the crystalline material observed for the pristine sample. This reacted interphase formation was identified as the cause of cell failure of Li|LAGP|Li cells due to high interfacial resistance arising from the interphase formation.

In situ investigation of LiPON|$LiCoO_2$ (LCO) interface revealed the presence of an amorphous, disordered interface between the cathode and solid electrolyte (Fig. 7d). The disordered layer was supposed to comprise of solid solution of Li_2O and CoO[137]. The decomposition of $LiCoO_2$ to Li_2O and CoO was accompanied by oxygen evolution. Formation and growth of the Li_2O/Li_2O_2 layer shown by TEM measurements was identified as an intermediate compound of decomposition reaction. Growth of this layer can lead to rapid capacity decay due to loss of active material. Extensive Co/Li diffusion at the LCO|LLZO inter-

face was evidenced by *in situ* TEM with the formation of interfacial products like Li_2CO_3, $La_2Zr_2O_7$ and $LaCoO_3$ (Fig. 7e)[136]. These reacted interphases lead to charge transport resistance (8x) compared to a pristine interface. *In situ* TEM also offered insight into the lithiation/delithiation pathway of LCO and their differences compared to conventional liquid electrolyte batteries[138]. Due to the point/line contact between SE and cathode in SSBs, lithiation/delithiation occurs along grain boundaries and leads to formation of polycrystalline material with formation of coherent twin boundaries and antiphase domain boundaries. Fundamental differences in charge storage mechanisms in well-studied cathodes highlight the need to study nm-scale transport for SSBs.

Anode interphase for thiophosphate solid electrolyte was recently studied by *in situ* TEM[35,79]. Iodine doped (LiI) LPS material was imaged with TEM before and after electrochemical cycling (Fig. 8). No morphological changes in SE or lithium metal anode were observed on passive contact. On application of a reducing bias to the solid electrolyte (Li ions move from SE to anode), a void/pore formation was observed on the interface (Fig. 8e-f). This morphological pitting of the surface was electrochemically irreversible and stays after oxidation. This interfacial chipping/pore formation was proposed to be a fundamental chemo-mechanical response of the SE|Li interface[139]. Local stresses can impact electrodeposition and dissolution kinetics as well as ion transport pathways leading to hot-spots[140,19]. Directional ion flux was postulated to be equivalent to a concentrated load that can cause the chipping of the SE. In addition to the chemo-mechanical response of the interface, EDS maps of the SE shows uniform distribution of I, P and Sulfur. After electrochemical cycling, even the Li metal shows the presence of iodine (Fig. 8l). This iodine diffusion was observed under both passive contact and electrochemically cycling conditions. Iodine diffusion through the Li metal surface offers a uniform nano-scale conducting interface between Li metal and solid electrolyte leading to improved electrochemical performance.

Electron backscattering diffraction (EBSD) is another tool which has wide applicability in SSB studies due to its ability to map grain and grain boundaries for polycrystalline materials[141]. EBSD maps for *in situ* heat treated Li-Mg alloys showed formation of a stable passivation layer with fewer impurities as well as well-defined crystal faces at the Li metal interface[142]. Stable passivation layer and improved interfacial contact by thermal treatment was proposed as a formation step for SSBs to enhance performance and stability. EBSD and nano-indentation techniques were used in conjunction to assess the impact of grain microstructure on the mechanical anisotropy of LATP solid electorlyte[143]. Hardness and elastic modulus were found to decrease when measured from the basal plane to the prismatic plane indicating that the rotation angle ϕ was an important factor dictating mechanical anisotropy of NASICON type solid electrolyte.

4.3 X-ray Imaging

X-ray imaging relies on electron-density contrast within materials to assess the spatial distribution of components in a system. This technique can be employed in a 2D geometry (radiography) or by measuring radiographs at several sample rotation angles for 3D structural information (tomography). X-ray tomography is a non-destructive tool that can be used to investigate the morphological evolution of bulk materials in 3D and *operando* conditions (Fig. 9a-b). Configuration of the optics setup and sample can provide XRT resolutions

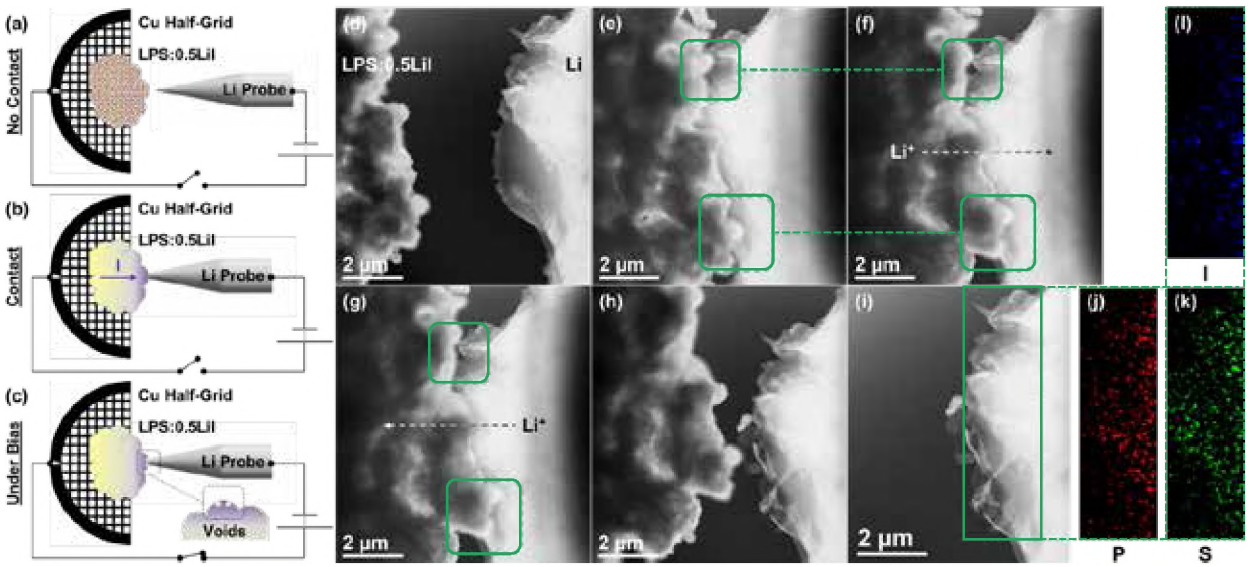

Figure 8: *In situ* investigation of interphase formation and chipping mechanism in thiophosphate solid electrolyte. (a)-(c) Schematic diagram depicting *in situ* testing procedure. (e)-(h) HAADF STEM images of Li probe and LiI–AN solid electrolyte prior to contact, upon contact, plating, stripping, and removal of contact. Region of interest is highlighted which shows irreversible void formation on plating. (i) HAADF STEM image of cycled Li with corresponding phosphorous (j), sulfur (k), and iodine (l). Reprinted from[85] with permission from Elsevier.

ranging from 20 nm to several μm (Fig. 9a). Resolution of X-ray imaging is determined by the optics employed in the measurement. For XRT, an optional monochromator selects the incident beam to the sample while down-stream scintillator and charge-coupled device camera is used to convert the transmitted photons to an optical image. This setup typically yields resolutions of $\approx \mu$m range. In contrast, transmission X-ray microscopy (TXM) employs a monochromator coupled with a capillary condenser to establish a micro-focused beam on to the sample. Fresnel zone plates, phase ring and CCD camera are used downstream to enable phase contrast, and turning the transmitted photons to an optical image (Fig. 9a). Thus, this tool is widely employed to study the meso-scale transformations in SSBs as well as microstructural transformations in bulk SE. Stresses coupled with volume changes of electrodes can lead to mechanical degradation in SEs. Significant studies have focused on characterizing the bulk microstructural changes in the SE in response to electrochemical cycling. For instance, XRT was used to investigate the role electrolyte (garnet oxide) microstructure had on dendrite or lithium filament formation[71,144]. Electrolytes processed at varying temperatures 1050, 1100 and 1150 °C exhibited different densities and pore size distributions. A more connected, tortuous pore network was observed for samples sintered at higher temperatures. Samples with more connected pores demonstrated faster filament growth and propagation and lower critical current densities. Failed samples showed a systemic increase in the X-ray transparent region which was identified as a potential evidence for Li plating in the bulk SE (Fig. 9c). Similarly, Li|LPS system was studied to assess the morphological changes in the anode as well solid electrolyte[145]. Comparison of cross sectional images from the XRT reconstructions at different cycles showed a decreasing thickness of lithium foil. Pristine cell showed Li thickness of 100 μm which reduced to 10-15 μm on the

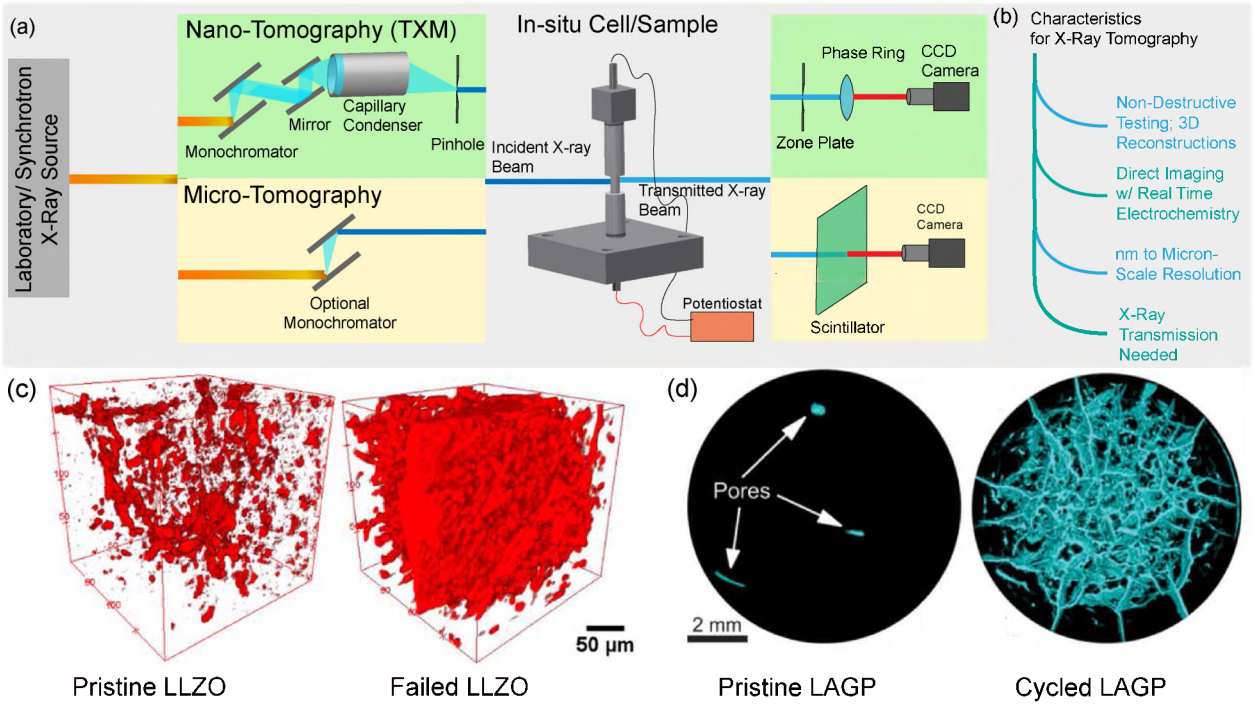

Figure 9: X-ray Imaging for Solid State Batteries. (a) Schematic diagram for X-ray tomography measurement highlighting the difference between micro- and nano- tomography experiments. (b) Characteristic for XRT imaging. (c) Differences in microstructure of pristine and failed garnet solid electrolyte. Increase in X-ray transparent phase is assumed to be evidence for Li plating. Adapted with permission from[71]. Copyright 2018 American Chemical Society. (d) Radial and circumferential crack generation in LAGP solid electrolytes. Adapted with permission from[33]. Copyright 2018 American Chemical Society.

first cycle and was indistinguishable from LPS for the subsequent cycles. Lithium insertion into the porous electrolyte matrix was proposed to modify the LPS material significantly giving rise to an increased concentration of dark gray, rounded features (lower density) at the Li|LPS interface compared to the pristine cell. *Operando* imaging further showcases monotonic increase of dark features identified as grain boundaries of LPS. The monotonic increase of the line features was proposed to be an evidence of growth of Li features within the LPS layer and propagation of the cracks in the LPS solid electrolyte. Lower beam energies used for this study, coupled with significant X-ray scattering limit the extraction of physical descriptors (porosity, tortuosity) of the Li|LPS cell. Both these reports showcase morphological changes occurring in the solid electrolyte during electrochemical operation which causes failure of the cell.

Similar studies have been carried out on Li|LAGP|Li system[33], Na|Na- β alumina | Na[146], In|$Li_{10}GeP_2S_{12}$|$LiCoO_2$[147] and Li|Li_6PS_5Cl|Li[148]. An extensive crack network growth was observed in the cell extending through the thickness of the LAGP pellet[33]. Distinct circumferential and radial cracks were observed in the LAGP pellet with the circumferential cracks forming at the outer perimeter of the pellet while radial cracks focused at the center of the pellet (Fig. 9d). The crack volume was found to correlate with the cell impedance with impedance rising from approximately 2.81 kΩ cm^{-2} to 256 kΩ cm^{-2}. The authors

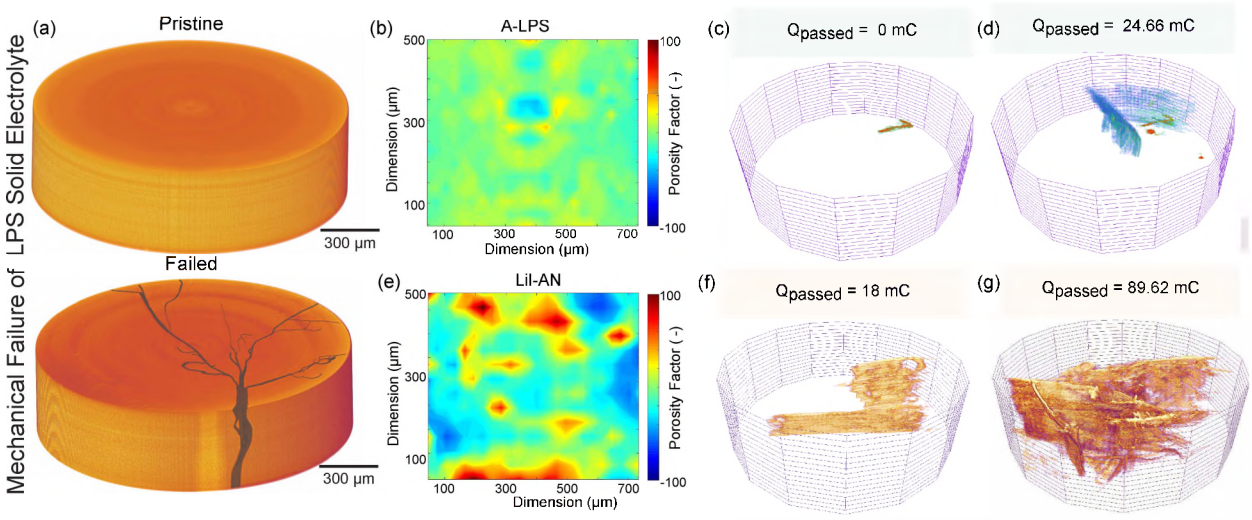

Figure 10: XRT study of failure in thiophosphate solid electrolyte. (a) 3D XRT images of pristine and failed LPS. Darker features in the failed electrolyte indicate cracks in the solid electrolyte. (b) Porosity factor variation in through-plane direction for amorphous LPS. Initial and final crack formation in samples for amorphous LPS (c)-(d). (e) Porosity factor variation in through-plane direction for annealed LPS. Initial and final crack formation in samples for annealed LPS (f)-(g). Adapted from[85] with permission from Elsevier.

indicate that mechanical fracture can be the source of the electrochemical failure of the cell. Fracture initiation was linked to the edges of the Li|LAGP contact area which was evidenced from the tomography reconstructions as well as simulations. Overall, the results indicated that the structure and morphology of the Li metal driven interphase formation dictated failure in LAGP. *In situ* XRT was used to investigate the role of interphase chemistry and microstructure has on failure propagation and chemo-mechanics of thiophosphate materials[85]. Metastable interphases in LPS materials were engineered by LiI addition and microstructural control was enabled by synthesis routes (milling, annealing). Extensive crack propagation in all investigated thiophosphate materials was visualized irrespective of the interphase chemistry and microstructure (Fig. 10a). *In situ* results highlight a common failure mechanisms for LPS materials wherein cracks were initiated by a chipping of the interfacial solid electrolyte and a subsequent growth of lateral crack through the material. The interfacial chipping mechanism was also observed at the nano-scale measurements with *in situ* TEM measurements confirming the validity of the mechanism across multiple length scales. The disparity in crack density between the materials with different microstructures was rationalized by the observed heterogeneity of the solid electrolyte. Electrolyte possessing higher structural heterogeneity leads to a tortuous pathway for ion motion thereby causing an extensive crack formation compared to solid electrolytes with a more homogeneous microstructure which showcases relatively local crack formation (Fig. 10b-c). Impact of microstructure on failure propagation was also evidenced in Na-based systems. A large crack in the Na- β alumina SE was proposed to act like a nucleation site for Na dendrite formation and eventual short-circuiting and failure of cell[146]. Crack formation was assumed to occur due to electrochemical stress arising from electrodeposition/electrodissolution of Na at the interface. Synchrotron radiography over long-term plating/stripping show electrode

thickness change and SE displacement consistent to the amount of Na cycled[147]. A tilt in the SE was observed that was anticipated to lead to stress generation in case of long-term stripping/plating due to uneven contact with the cell housing. Tomography results showed a densification of the $Li_{10}GeP_2S_{12}$ solid electrolyte during charging consistent with the pressure changes measured for the cell. The porosity of the solid electrolyte decreases from 5.5% for the pristine sample to 2.6% after cycling. Measured height fluctuations of the cell were consistent with the densification mechanism with a significant asymmetric change in cell height observed in the initial cycles. In addition, the charged cell shows a significant bending indicating a strong pressure build up at the electrode|electrolyte interfaces. The cells were assembled in absence of stack pressure and thus reflect the change in the shape of the cell reflects the mechanical forces acting on the cell during charging. The solid state battery showed bending towards the cathode side due to higher volume expansion at the anode. Further, cracking of the SE was observed at the edges of the charged cell. For Li_6PS_5Cl, tomography measurements show the presence of low density region within the bulk solid electrolyte consistent with dendrite formation[148].

Ex situ imaging of solid electrolytes can also provide important information regarding microstructure and phase distributions. Laboratory *in situ* XRT study of Li_6PS_5Br SE under high pressure was carried out to elucidate the influence of microstructure on ion transport properties of the solid electrolyte[149]. Ionic conductivity of LPSBr increased from ≈ 0.2 mS cm^{-1} to ≈ 0.8 mS cm^{-1} on increasing the pressure from 10 to 100 MPa. XRT images revealed that the porosity decreased, and particle|particle contact increased as the applied pressure increased from 8.4 to 100.3 MPa. The density of the solid electrolyte was monitored directly via monitoring the electrolyte thicknesses. As the pressure increased between 0 and 30 MPa, a large decrease in the electrolyte thickness was observed (large increase in density) owing to removal of pores from the system. Above 30 MPa there was less changes in the electrolyte density due to absence of pores. Further, at the high pressures, particle pulverization was observed which results in improved density by smaller particles filling the remaining pores. This also results in non-linear strain behavior with increasing pressure between 0-100 MPa. The results highlight the influence of microstructure on ion transport properties of solid electrolytes. Microstructure evolution was identically investigated for a series of LLZO-PEO-$LiClO_4$ hybrid electrolytes with varying ceramic loading to understand the agglomeration phenomena[86]. High degree of agglomeration as well as heterogeneous distribution of ceramic particles in the hybrid electrolytes was observed. Accessible particle surface area was found to correlate well with the ionic conductivity indicating that ion transport in hybrid electrolytes was dictated by interphase between the ceramic and polymer phases.

TXM-XANES offers a facile way for segmenting two phase crystalline systems quantitatively[150]. Lanthanum doping of $Na_{1+n}Zr_2Si_nP_{3-n}O_{12}$ ($0 \leq n \leq 3$), can improve the electrolyte's ionic conductivity. Introduction of a dopant can induce concentration gradients of mobile ions in the pristine phase, enhancing the density of the two-phase electrolyte and by creating faster grain boundary conduction pathways through formation of a second phase. TXM images of the composite solid electrolyte showed a heterogeneous distribution of the secondary phase ($Na_3La(PO_4)_2$) with considerable size disparity. La, P, Zr and Si elemental mapping showed that Zr and Si spatial distributions were anti-correlated with the La and P distributions confirming that Zr and Si both belong to the primary phase. Elemental distributions within material were also assessed by *operando* radiography in silver-ion

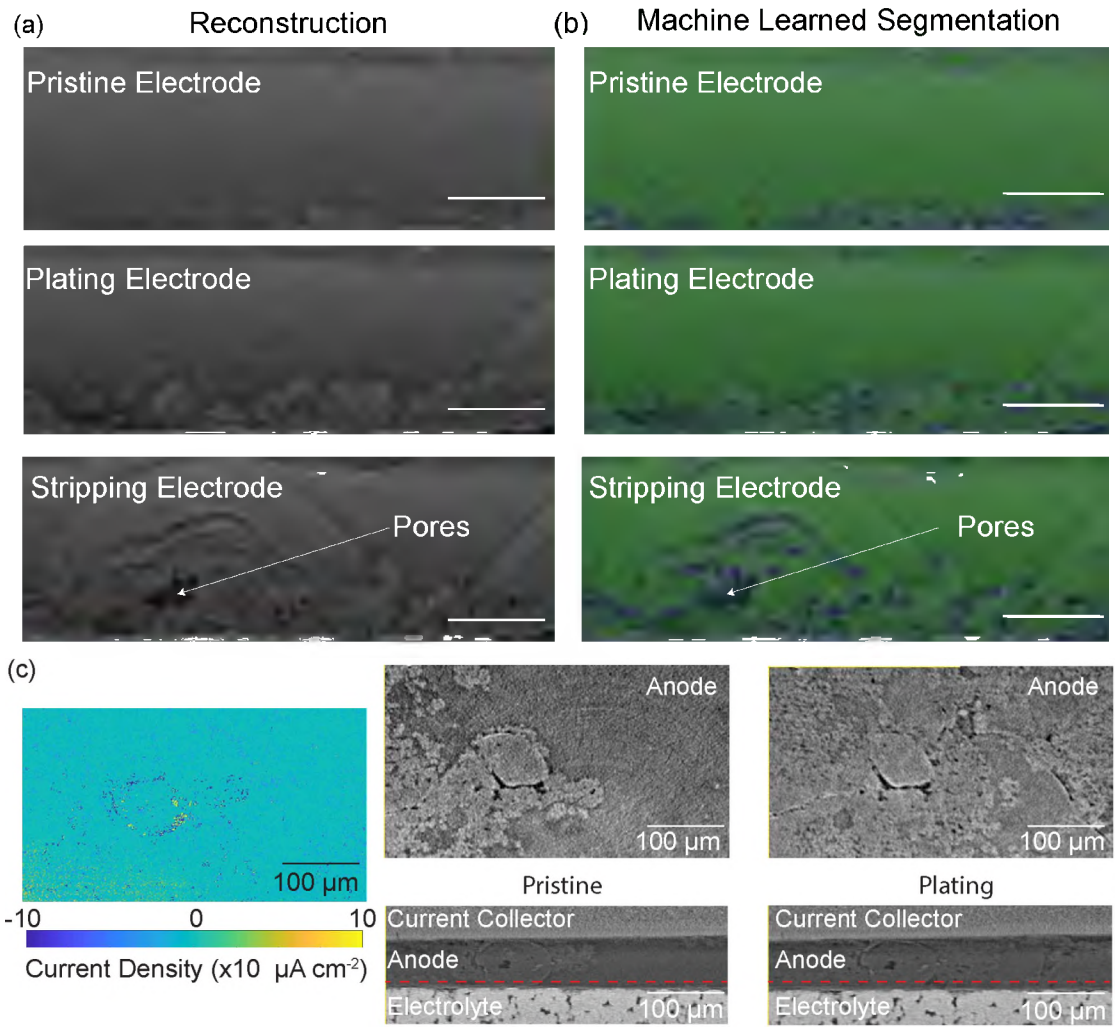

Figure 11: Li imaging by *in situ* XRT. (a) Raw XRT reconstructions for Li at different stages of cycling. Cross-section image shows evidence of hot-spot and pore formation in the Li electrode. (b) Convolution neural network enabled segmentation of Li and pore phases from the XRT images. (c) Local spatial current density maps highlighting hot spots in the Li metal and corresponding morphology. Adapted with permission from[84]. Copyright 2020 American Chemical Society.

conductors[151]. Silver ion system was leveraged to improve the absorption contrast (high Z leads to improved contrast compared to Li). No concentration gradient was measured within the solid electrolyte during cycling of the Ag|Ag symmetric cell. The absence of observed variation in transmission intensity through the sample was consistent with the near-unity transference numbers (t^+) reported. Radiography is sensitive to density variations within the material. However, it is unclear whether a concentration gradient of ionic species within the sample can generate enough contrast even at high current densities to be captured.

Tomography studies of solid electrolytes conclusively show evidence of severe chemo-mechanical degradation in bulk materials during electrochemical cycling. Stresses linked with electrodepostion/dissolution of the anode as well as intercalaction/de-intercalation reactions at the cathode can lead to failure of the battery by fracture of the solid electrolyte. Recent modelling efforts have focused extensively on understanding the chemo-mechanical

coupling of the anode|solid electrolyte interfaces using phase-field, continuum as well as finite-element methods[152,153,154,155]. All models concur that presence of irregularities at the interface (contamination, surface features like cracks) leads to generation of regions of very high stress exceeding the fracture toughness of solid electrolyte materials leading to fracture. A key aspect that was recently discussed in the literature is the application of stack pressure and its role in mitigating interfacial challenges and homogenizing interfacial stresses in solid-state batteries[28,29,31]. Certain modelling results indeed show that application of high stack pressure can lead to a more uniform Li|SE interfaces minimizing the chances for stress-driven failure[154,125]. However, other reports show that stack pressure has no effect on deposition stability at the anode|electrolyte interface[153]. XRT is an ideal characterization tool to investigate the meso-scale transformations expected in the solid electrolyte and the anode|electrolyte interface. However, designing experimental setups that are compatible with X-ray endstations while offering pressure and temperature ranges (1-20 MPa, 25-100 °C) required is challenging. These operating parameters typically require extensive instrumentation that are not compatible with constraints placed at the endstations. Indeed, most *in situ* experiments reported here work do not report operating stack pressures and are likely not in the MPa range based on the experimental cell designs. Future work on cell design that can enable controlled *in situ* and *operando* experiments is vital to assessing the chemo-mechanical response of solid electrolytes at relevant operating conditions.

Controlling the morphology of an metallic anode during cycling is crucial to achieving high coulombic efficiency batteries. Inherent interfacial resistance, slow kinetics as well as chemical decomposition at the SE|anode interface leads to non-uniform electrodeposition of Li metal. Typically, low density of the metallic anode makes X-rays a less promising alternative to observe morphological transformations during electrochemical cycling. However, XRT is still used in certain studies with Li metal as well as other anode materials (Na, Sn). Careful experimental design and parameter optimization enables tracking Li metal transformations in Li|LLZO|Li system with XRT[84]. Pore formation and local hotspot generation in lithium metal were clearly visualized in tomography reconstructions manifested as darker regions at the interface and semi-circular contours in the cross-sectional images (Fig. 11a). Leveraging convolutional neural networks for segmentation can enable distinguishing between low contrast phases of Li metal and pores enabling quantitative insight from the system (Fig. 11b). In addition, advanced image processing enabled isolating and characterization of hot-spots in the electrodes (Fig. 11c). Hot-spots in Li metal were correlated to sub-surface electrolyte microstructure where local regions possessing sub-optimal transport and mechanical properties can initiate failure. Na|Na β-Al_2O_3 interface was characterized using *operando* lab-scale XRT measurements[31]. Na metal anode showed porosity at the pristine interface in the tomography scans. Void number density as well as sizes increases during stripping while a complementary behavior was observed during plating (Fig. 12a). The interfacial contact between Na and SE shows a consistent decrease with increasing cycles with the total void volume showing a system increase during cycling. In addition, pore size distribution during cycling shows persistence of smaller pores even during plating cycles which suggests a partial filling of larger pores during the electrodeposition step. Persistence of the smaller pores indicate the mechanism for void growth and accumulation at the interface during cycling. Loss of active contact area of Na|SE can lead to increased local current density that can cause filament formation and cell short. A similar study was carried out

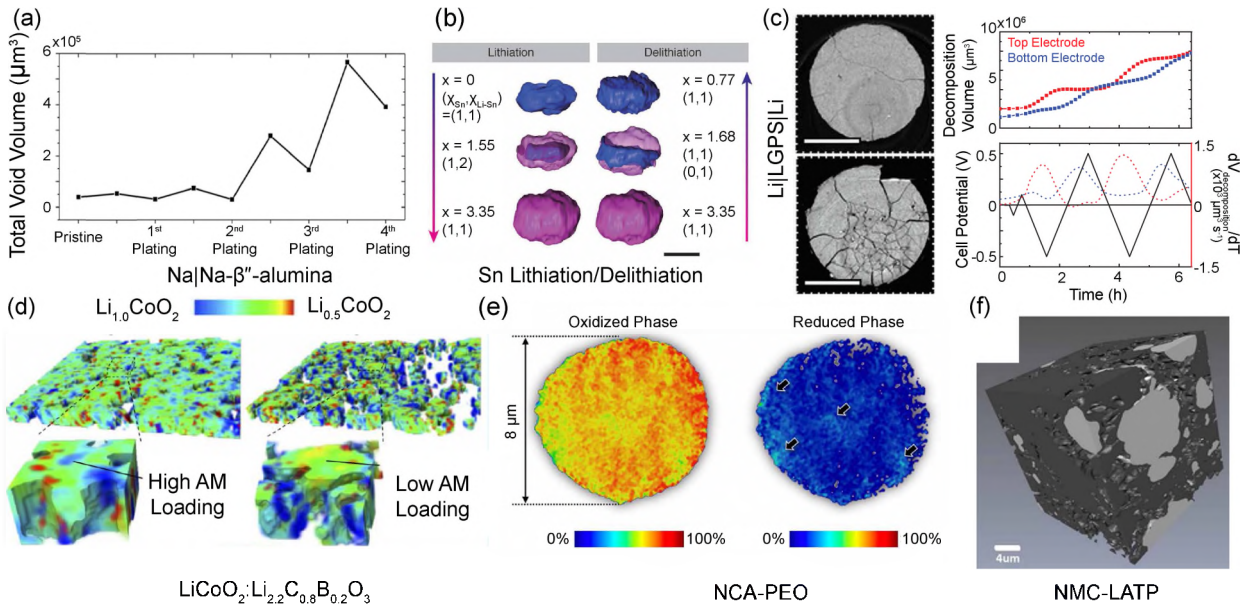

Figure 12: Summary of investigations on anode|SE and cathode|SE interface and electrode transformations. (a) Porosity in Na electrode during cycling measured by synchrotron XRT. Adapted with permission from[31]. Copyright 2020 American Chemical Society. (b) Sn structure transformation and oxidation state measured during electrochemical cycling. Adapted from[156] with permission from Wiley.(c) Mechanical degradation of $Li_{10}GeP_2S_{12}$ (LGPS) and corresponding quantitative interpretation of XRT data-set indicating growth of reacted interphase. Adapted from[157] with permission from Wiley. (d) Lithiation distribution and reaction front propagation in composite LCO cathodes based on loading differences. Adapted with permission from[96]. Copyright 2020 American Chemical Society. (e) Chemo-mechanical effects and SoC distribution of NCA cathode was investigated using *ex situ* XANES imaging. Adapted with permission from[133]. Copyright 2019 American Chemical Society. (e) Chemo-mechanical effects and SoC distribution of NMC-LATP composite cathode. Adapted with permission from[158]. Copyright 2018 American Chemical Society.

on Li|LPSCl|Li system[29]. Lower contrast offered by Li metal did not enable resolution of pores independently. Images averaged over cell thickness showed clear evidence of interfacial delamination and pore formation in Li metal at high stripping current density. These results highlight the morphological variations in anode|SE interface and its impact on failure mechanisms.

Morphological changes in composite Sn anode material in $InLi_x$|LPS|Sn solid state battery were tracked using *operando* synchrotron TXM studies (Fig. 12b)[156]. The solid-state battery was charged and discharged between 2 and 0.1 V. A strong correlation in the observed lateral strain in the working electrode was observed compared to the theoretical expansion of equivalent quantity of Sn. This indicated a strong influence of volume change of active material on macroscopic deformations of the electrode. Morphological evolution of the active material showed a strong spatial heterogeneity with the Z- axis showing preferential expansion (up to 90 %) compared to X- or Y- directions (approximately 10%). The preferential expansion might arise from cell constraints as well as electrode aspect ratio. Topological analysis of Sn particles indicated a core-shell evolution of the lithiation process. Furthermore, a reaction gradient was observed in the electrode with Sn particles near the separator showing higher concentration of Li-Sn, while those at the current collector remain

almost inactive. Horizontal (XY- plane) and shell voids were observed in the working electrode that showed a cyclic behavior during cycling. Lithiation caused an increase in the crack density, while delithiation caused the cracks to disappear. Horizontal cracking was proposed to occur due to z- oriented expansion of the active material, while the shell voids occur due to non-reversible morphological changes to the Sn particles. So far, XRT has seen limited use in characterization of Li metal plating. Recent work with XRF mapping and phase-contrast XRT has shown applicability of X-ray imaging towards characterization of Li metal anodes[159]. Further work on experiment design to characterize low Z- elements as well segmentation is expected to provide avenues for investigating anodes in solid-state batteries.

Effect of interlayer chemistry on stability of electrodeposition of Li in $Li_{10}GeP_2S_{12}$ (LGPS) solid electrolyte was investigated by XRT[157]. A decomposition threshold area of ≈150 μm was identified at the LGPS|Li interface that can cause fracture of the solid electrolyte (Fig. 12c). Addition of high concentration liquid electrolyte suppresses decomposition reaction significantly aiding in stabilization of the interface. Composite cathode offers an ideal material system for investigation through X-ray tomography. Understanding the relationship between composition, processing and resulting three-phase architecture is crucial for achieving high rate capability cathodes. Additionally, chemo-mechanical degradation (delamination, cracking) during cycling is also investigated by X-ray imaging. Impact of loading on active material utilization in composite cathodes was investigated by XRT[96]. $LiCOO_2$ (LCO) was used as cathode active material and $Li_{2.2}C_{0.8}B_{0.2}O_3$ (LCBO) was used as a solid electrolyte. Two cells were assembled with cathode compositions of LCO:LCBO = 5:5 and 8:2, LCBO solid electrolyte and Li metal anode. Cell with 8:2 cathode composition showed a specific discharge capacity of 57 mAh g^{-1} (48% theoretical capacity) while the 5:5 cathode composition cell showed a specific discharge capacity of 85 mAh g^{-1} (70% theoretical capacity).No reaction distribution in the through plane direction of the electrode was observed indicating a ion-diffusion limitation(Fig. 12d). This was contradictory to some other literature reports[133,160]. However, a heterogeneous distribution of in-plane AM utilization was observed. In particular, the 8:2 system shows larger AM aggregates with the central regions of these aggregates showing a lower degree of lithiation. In comparison, 5:5 system showed lower aggregation due to the reduced active material loading leading to smaller aggregates and a more homogeneous reaction distribution within the active material aggregates. Similar study was carried out on NCA-PEO cathode material[133]. The SSBs showed a significant drop in capacity over 20 cycles from 180.36 mAh g^{-1} to 83.09 mAh g^{-1}. The cathode materials were harvested from pristine, single-charged and cycled cells. TXM cross-sectional images for secondary particles from the cathode clearly show presence of irregular patterns throughout the particles ascribed to the cracking of the secondary particles. This cracking was concentrated in the center of the secondary particles. XANES imaging of 2D cross sections over the Ni K-edge clearly indicated presence of domains containing discharged cathode material even though the samples were harvested from a charged cell. 2D XANES imaging shows a heterogeneous utilization of the secondary particles with isolated, discharged domains that seem electrochemically inaccessible (Fig. 12e). Additionally, 3D-TXM-XANES images show a correlation between morphological cracking of the particle and the inactive domains identified in the 2D XANES maps. The results indicated loss of electrochemical activity in the core of the particle driven by loss of ionic diffusion pathways due to cracking of the particle.

Ensuring a three phase contact between the active material, solid electrolyte and electron

conducting additive is crucial for a composite cathode. X-ray imaging is used extensively to assess the spatial distribution of the individual phases and identification of transport bottlenecks in the structure of composite cathodes. Investigation of NMC : LTAP : Super-P carbon (47:47:6) composite cathode was carried out by *ex situ* TXM[161]. The composite cathodes were fabricated at 700 and 1300 psi. Geometric analysis showed poor three phase interface between the components that was required for achieving electrochemical access of the active material. LTAP coverage on NMC improves from 55% to 59% on increasing the assembly pressure from 700 to 1300 psi. Similarly, XRF imaging was used to investigate the Zr and Mn distribution of NMC infiltrated LLZO scaffolds[162]. Complementary distribution of Mn and Zr was observed indicating that NMC has infiltrated the voids present in the LLZO scaffold. Lab-scale XRT was used to image NMC-LPS based composite cathodes which were used for microstructure-resolved simulations[160]. Visual analysis of the reconstructed cathodes showed fluctuations in the in-plane composition. Lower electronic conductivity and preferential lithiation closer to the separator were identified as capacity fading mechanisms through simulations. Concentration gradients in a Ag | $Ag_6I_4WO_4$| $TiTe_2$ full cell was investigated by synchtrotron radiography[151]. $TiTe_2$ composite cathode also contained solid electrolyte and acetylene black to allow for ionic and electronic conduction. Full cells were cycled at 0.2C (1.05 mA cm^{-2}) and a reversible capacity of 32 mAh g^{-1} was obtained corresponding to 0.36x theoretical capacity of $TiTe_2$. Overall, the cathode shows an increase in X-ray transmission consistent with the extraction of Ag-ions. A decrease in X-ray transmission of solid electrolyte was observed and was attributed to the growth of silver dendrites from the anode. Additionally, a preferential reaction at cathode|electrolyte interface was observed indicating a ion- diffusion limitation in the cathode. While the methods used for silver ion conductor are not necessarily translatable to Li or Na systems, this study shows potentially important bottlenecks to ion transport in all solid-state system. These results highlight the importance of tailoring composite cathodes microstructures to facilitate fast ion transport to ensure high energy and power capacity of solid-state batteries.

4.4 Neutron Depth Profiling

Neutron depth profiling has been extensively employed to understand distribution of low Z- element, specifically Li in solid state batteries (Fig. 13a-b). Monte carlo simulation models in combination with NDP energy profiles are used to generate Li concentration depth profiles to generate further insight into the battery mechanisms. Li accumulation in the $LiPO_4$ (LPO) electrolyte was identified as the origin of aging mechanism in thin film SSBs[165]. This mechanistic origin identified by combining MC models with the measured energy profiles correlates very well with the electrochemical results. Li enrichment zone at garnet surface and adjacent depletion zones were identified in LLZO garnets undergoing atomic layer deposition (ALD) coating of Al_2O_3 by NDP[166]. Surface Li reaction with ALD precursor trimethyl alumina (TMA) and water generate a Li-Al-O layer adjacent to the Al_2O_3 layer which was observed as a sub-nm region in SAEED images. Al_2O_3 coated LLZO was shown to contain higher concentration of Li in the surface region compared to bare LLZO. This high concentration of Li near the interface enables a higher rate performance from the electrolyte by enabling consistent charge transfer at Li*vert*SE interface. Lithium deposition in bulk solid electrolytes was investigated by time resolved, *operando* NDP[77].

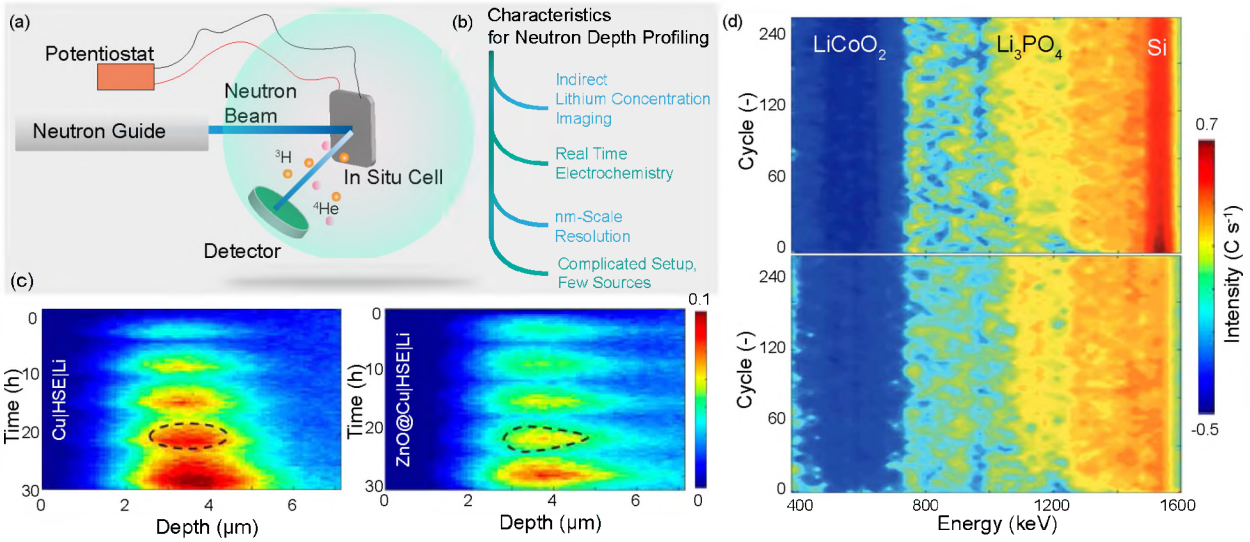

Figure 13: Summary of Neutron Depth Profiling Studies of Solid-State Batteries. (a) Schematic diagram showing the working principle of neutron depth profiling. (b) Characteristics of NDP studies. (c) Li plating in Cu|HSE|Li with and without a ZnO interlayer. Adapted with permission from[163]. Copyright 2020 American Chemical Society. (d) Lithiation and delithiation of LCO and Si electrodes. Adapted from[164] with permission from Wiley.

LCO|LiPON|Cu, Li|LLZO|Cu and Li|LPS|Cu cells were investigated. LiPON sample did not show any shorting behavior while LLZO sample shorted at 1.06 mA cm^{-2} after a cumulative charge of 4.6 mAh cm^{-2} (23 μm) and LPS sample shorted at 2 mA cm^{-2} after a cumulative charge of 1.2 mAh cm^{-2} (6 μm). *Operando* visualization of NDP energy profiles indicate nucleation and growth of Li dendrites inside LLZO and Li_3PS_4. High electronic conductivity of these materials was identified as the cause of lithium deposition in the SEs.

Similarly, impact of ZnO ALD layers on lithium metal electrodeposition stability on copper with a PEO-LAGP based hybrid solid electrolyte (HSE) was investigated by NDP (Fig. 13c)[163]. *Operando* NDP results show a that for the bare copper current collector, the average Li density, as well as the thickness of the deposits, rapidly increase upon cycling, reflecting buildup of inactive lithium- metal and Li-species at the HSE side. Introduction of ZnO layer on the current collector, results in improved affinity between the Li metal with the ZnO-covered current collector leading to a reduced accumulation of dead Li metal deposits. Additionally, integration of the observed density profiles allows for calculating plating/stripping efficiency which was approximately 45% for Cu current collector and 80% for ZnO@Cu current collector. Similar measurements to investigate electrodeposition stability at anode interfaces were carried out to understand plating/stripping behavior of Li in solid state battery working with Ti and carbon nanotube interlayers in Li|LLZO|Li[87,75] as well as for LCO|Li_3PO_4|Si thin film batteries[167]. Ti|LLZTO|Li cell was cycled up to a cumulative charge passed of 600 μAh[87]. NDP energy profiles as well as fitting results suggests Li preferentially deposits within the holes of the patterned Ti electrode as opposed to the Ti|SE interface. This architecture can significantly reduce interfacial stress due to electrode volume change and mitigate dendrite formation. Li plating behavior at the electrode|electrolyte interface was evaluated for Li|Li symmetric and Li|CNT asymmetric cells by NDP[75]. NDP

energy profiles indicate the formation of a reversible layer near the SE|CNT interface that shows reversible cycling. Plating in excess of this region was left behind and accumulates in the CNTs. At low current density (100 μA cm^{-2}) net change in charge passed in Li|Li symmetric cells and the integrated NDP counts turn out to be near zero at end of cycle indicating reversible plating/stripping behavior. At higher current density (200 and 400 μA cm^{-2}) no accumulation of Li at end of each cycle was observed until failure indicating complete reversibility. After short circuit, inner layers show an increase in counts indicating Li accumulation in garnet pellet. Lithiation and delithiation behavior in LCO|Li_3PO_4|Si thin film batteries were tracked using operando NDP (Fig. 13d)[167]. The intensity profiles for the initial formation cycles follow expected trends with respect to lithiation and delithiation. However, high lithium content cathode and Li- free anode were not realized after the first two cycles indicating presence of immobilized Li in the anode. In addition, an immobilized interlayer was also identified at the anode|electrolyte interface. *Operando* NDP scan of the charged battery over long term cycling highlight stability of the cathode over the duration of the cycle while a monotonic decrease in lithium content at the anode. In addition, a generation of increasingly concentrated immobilized Li containing interlayer at the anode|electrolyte interface was identified. NDP map of the discharged cell over the cycling duration show consistent behavior. Si-migration to the solid electrolyte was identified as the cause of generation of the Li rich interlayer by XPS measurements. Si-containing interfacial layer can trap higher amount of Li that cannot be extracted during normal battery operation limiting the capacity of the battery.

Lithium concentration in a thin film LCO|LiPON|Cu battery was investigated by neutron depth profiling[110]. The thin film battery was charged at 10 μA ($\approx$ 0.3C) to 4.2 V. To further understand the lithium migration between cathode and solid electrolyte, LCO was fabricated with 100% ^{6}Li which results in higher intensity for the cathode compared to the solid electrolyte. No interaction between cathode and electrolyte was observed during passive hold between fabrication and testing (one week). Upon charging a significant decrease in intensity at the cathode was observed consistent with depletion of Li from the cathode. In addition, the depletion was stronger at the SE|cathode interface which was proposed to arise from ^{6}Li migration from cathode to solid electrolyte as well as the charging reaction. Similar analysis was carried out on LMO|LiPON|LNO thin film battery[173]. NDP scans were take for fully charged and discharged battery. Comparison of the two scans indicate that most change in lithium concentration was observed in the two electrodes (approximately 14-16%) with minimal change in the electrolyte (0.1%). 31% of the total calculated lithium concentration was estimated to participate in the redox reactions. Spatial 2D imaging of NDP profile indicates inhomogeneous distribution of Li in the SSB with Li being concentrated near the center of one half of the sample (28% of lithium in 8% the total cell area). These results highlight the need to understand spatial distribution of lithium migration within solid state batteries.

4.5 Atomic Force and Scanning Probe Microscopy

Atomic Force/Scanning Probe microscopy (AFM/SPM) offer simultaneous multi-modal measurements of materials by physical contact of a nano-sized cantilever probe with the material (Fig. 14a). AFM/SPM can provide morphological information, mechanical property mea-

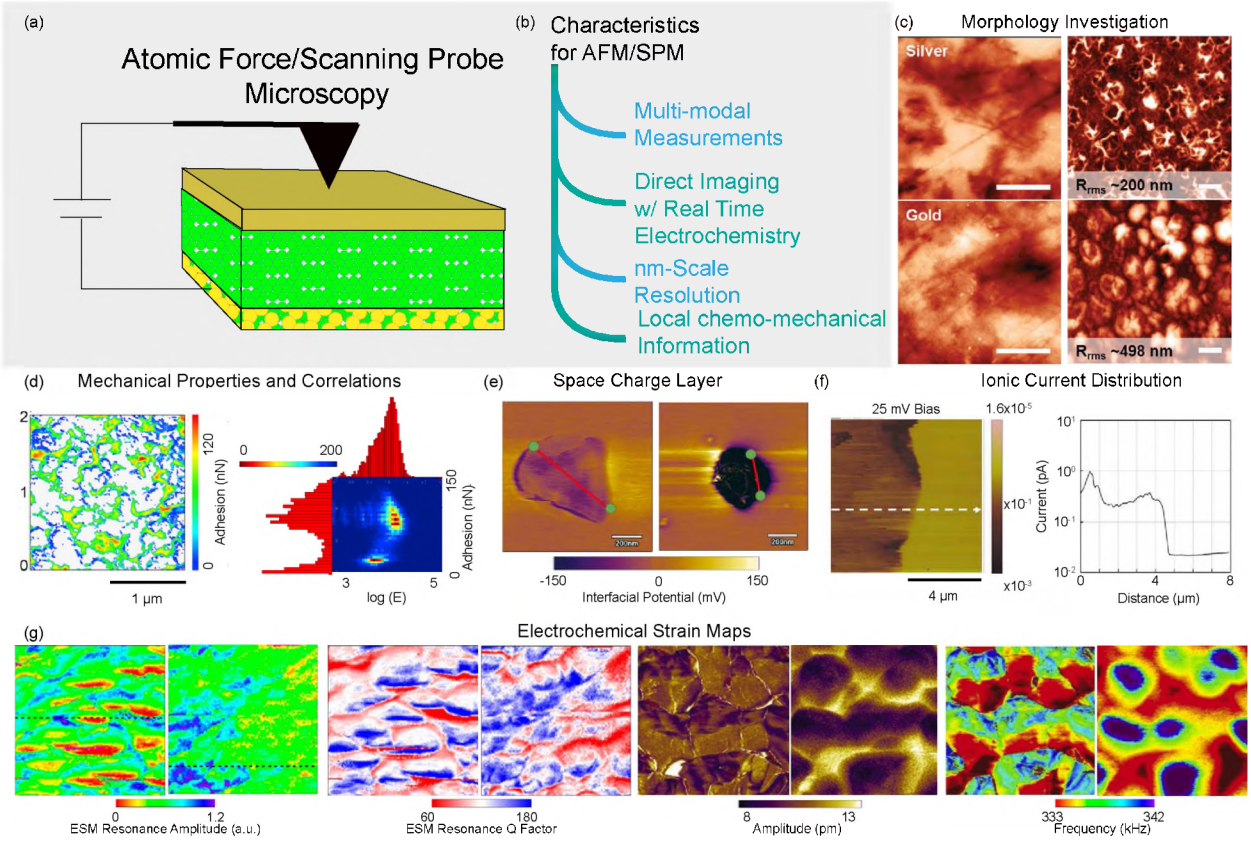

Figure 14: Summary of Atomic Force/Scanning Probe microscopy (AFM/SPM) Characterization in Solid State Batteries. (a) Schematic diagram showing AFM/SPM microscopy technique. (b) Characteristics of AFM/SPM investigations. (c) Investigation of Li plating morphology variations with different interlayer coating materials (Au, Ag). Adapted from[168] with permission from Wiley. (d) Mechanical property distribution and correlation between adhesion and Young's modulus for PEO-LLZO hybrid electrolytes. Adapted from[79] with permission from Elsevier. (e) Space charge layer in NMC particles embedded in SE matrix investigated by AFM. Adapted from[169] with permission from Elsevier. (f) Ionic current distribution at polymer|particle interface for a hybrid electrolyte. Adapted from[170] with permission from Wiley. (g) Electrochemical strain maps depicting resonance amplitude, Q-factor and resonant frequency for composite cathode (NMC) and solid electrolyte (LAGP). Adapted from[171] with permission from Elsevier. Adapted with permission from[172]. Copyright 2020 American Chemical Society.

surement and can also be used to assess electrochemical properties of the material with nm-level resolution (Fig. 14b). While, these techniques have seen limited application to SSBs so far, it is anticipated that careful design of experimental setup can enable wide applications of this technique to assess the electro-chemo-mechanical transformations in SSBs. The primary use of AFM is to assess morphological evolution during cycling (Fig. 14c). Li plating morphology during plating was investigated and the impact of interlayer chemistry (Au, Ag, Si) was investigated for LLZO garnets[168]. Li deposition on gold interlayer shows much larger electrodeposited nuclei with higher roughness compared to the silver interlayer system. In addition to higher roughness of electrodeposited Li, cycling efficiency was also identified to be lower with Au and Si systems compared to Ag interlayer system. Difference

in kinetics and activation barriers for electrodeposition between the three layers dictate the difference in cycling efficiencies. Mechanical properties like adhesion and Young's modulus were measured for extrinsic interfaces in hybrid electrolytes (Fig. 14d)[79]. Electrochemical performance of hybrid electrolytes processed with three different molecular weights of PEO (300K, 1M, and 5M) were correlated to the interfacial mechanical properties of the hybrid electrolyte. Specifically, the high adhesion of the 300K hybrid electrolyte leads to higher capacity and improved retention of SSBs. In addition to this, co-variation of adhesion and Young's modulus indicate that sub-surface distribution of ceramic particles in the hybrid electrolyte dictate the surface mechanical properties. Disparate sub-surface microstructure can also lead to differences in electrochemical properties[170]. AFM results showed two orders-of-magnitude difference in local ionic conductivity for polyimine-LPS hybrid electrolyte. In addition, a sharp change in ionic current was observed at the LPS|polyimine boundary with ion current decreasing with smaller polyimine particles as well as cycling (Fig. 14f). Origin of these differences was proposed to be the intrinsic anisotropic kinetic barriers along different material axes.

Electric potential differences across NMC particles were investigated by AFM (Fig. 14e)[169]. Differences in surface potentials investigated by AFM directly correlates to strength of the space charge layer in the cathodes. NMC in LLZO matrix shows a higher potential (-42.1 mV) compared to the composite cathode with NMC-Li_3PO_4-LLZO matrix (-144.3 mV). These results were consistent with DFT studies that indicate that careful interface engineering weakens the space charge layer and improves interfacial charge transfer across the SE|active material interface. AFM can also be used to evaluate electrochemical strain maps within materials where in electrochemical strain originated from a bias-induced ionic diffusion and related molar volume change in battery materials[174]. NMC thin films show differences in ionic mobility and electrochemical activity as observed by differences in distribution of the resonance amplitude and Q factor of the measurement (Fig. 14g). High Li- ion concentration areas in the cathode were identified at grain-boundary-like features and surface defects. Decrease in Li-ion concentration on cycling was also localized at grain boundary regions which was stronger in the initial cycles. Higher Q factor observed in the cycled sample also indicates an increased charge transfer barrier resulting in lower Li-ion diffusivity and electrochemical activity. Strong coupling between ionic/electronic diffusion, surface mechanical properties and capacity fade of the NMC cathodes was established. Similar investigation on LAGP solid electrolyte material indicate difference in mechanical properties of the LAGP crystalline domains and the glassy domains belonging to the amorphous interphase generated in the material[171]. Contact stiffness mismatch between these phases was proposed to cause crack formation in LAGP solid electrolytes.

5 Reciprocal Space Characterization

Reciprocal space studies typically provide information concerning phase, texture and stress within the investigated systems (Fig. 15a-b). Scattering-based techniques (X-ray, neutron based) probe the atomic length-scales within the material. While spatially resolved techniques can enable probing of samples over larger length-scales, the underlying information is typically obtained from length-scales associated to long-range and short-range order in the

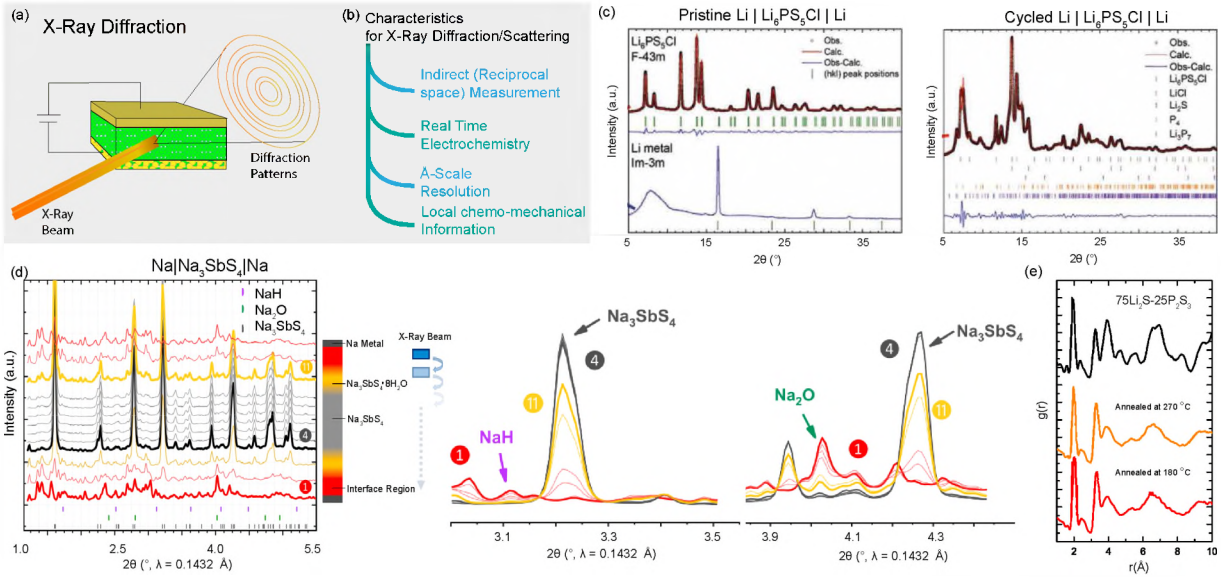

Figure 15: Summary of Reciprocal Space Characterization in Solid State Batteries. (a) Schematic diagram depicting diffraction investigation methodology. (b) Characteristics for diffraction studies. (c) Reitveld refinement of diffraction patterns obtained from pristine and cycled symmetric Li_6PS_5Cl cells. Strong decomposition of the cycled sample is observed from XRD studies. Adapted from[148] with permission from Wiley. (d) Spatial profile of Na| Na_3SbS_4|Na cells highlighting the stability of hydrated interfaces. Close up of regions of interest in the diffraction patterns. Adapted from[175] with permission from Elsevier. (e) Pair distribution function analysis for LPS based solid electrolytes during annealing. Adapted from[176] with permission from Springer.

investigated materials. While probing crystalline materials, Bragg reflections are generally tracked and these studies are broadly discussed here as diffraction studies. Scattering studies highlight the insight into the structure obtained from non-Bragg reflections from amorphous materials.

Coupled, *ex situ* XRT and diffraction measurements of pristine and cycled Li|Li_6PS_5Cl|Li cells was carried out to assess the impact of high pressure cycling to the phase as well as the microstructure to the solid electrolyte (Fig. 15c)[148]. Diffraction from the pristine bulk solid electrolyte shows only the presence of Li_6PS_5Cl while the cycled sample shows evidence of presence of numerous phases like LiCL, Li_2S, and reduced phosphorous species. Li dendrite growth through the solid electrolyte bulk introduces fresh Li|SE interfaces where solid electrolyte interphase (SEI) generation can lead to formation of decomposition products identified by the XRD results. Additionally, the impact of pressure on the performance of Li|Li_6PS_5Cl|Li cells was investigated. High stack pressures $>$ 25 MPa were shown to accelerate failure due to Li creep through electorlyte pores. An optimal stack pressure of 5 MPa was identified for the Li|Li_6PS_5Cl| (Lithium Niobate) LNO-coated NCA system that enabled long-term cycling with 80.9% retention at 100 cycles. A similar study using *ex situ* spatially resolved XRD was carried out for Na|Na_3SbS_4|Na cells to characterize the Na|SE interface (Fig. 15d)[175]. The work investigated the influence of hydration of Na_3SbS_4 solid electrolytes and its impact on stabilization of the Na|SE interface. XRD results show presence of decompsition products like NaH, Na_2O as well as $Na_3SbS_4.8H_2O$ in the layers closest to Na metal. Layers further in the bulk of the sample shows presence of combination

of the hydrated solid electrolyte with pristine Na_3SbS_4 and only the pristine solid electrolyte in the bulk. Hydrated solid electrolyte mitigates degradation of the Na metal anode against the Na_3SbS_4 solid electrolyte. Further, presence of Na metal was validated highlighting the protection of Na metal by hydration of the electrolyte.

X-ray diffraction was proposed as an indirect measure for state-of-charge (SOC) of SSBs[177]. In|Li_6PS_5Cl|NMC with uncoated as well as $LiNbO_3$ coated NMC were assembled and cycled between 2.3 and 3.8 V at C/20 rate. $LiNbO_3$ coated NMC delivered higher specific charge capacity and coulombic efficiency (165 mAh g^{-1}, 81%) compared to the uncoated NMC (154 mAh g^{-1}, 72%). High charge transfer resistance for the uncoated NMC due to side-reactions and partial contact loss with SE can lead to lower capacities for the initial cycles and poor coulombic efficiency. Presence of inactive cathode active material was identified by comparing *ex situ* and *operando* diffraction patterns of SSBs with conventional liquid electrolyte cells. Refinement of the XRD considering the inactive phase leads to estimation of SOC of the coated and uncoated materials as 173 and 162 mAh g^{-1} which were consistent with the experimental results. These results indicate that XRD is a potential tool for reliably assessing SOC of SSBs and to investigate presence of inactive CAM within the composite cathode. *In situ* XRD was used to estimate unit cell volume change for NCM, NCA and LCO cathode materials[41]. Unit cell volume reduction of 4-6% was observed for NCM and NCA electrodes, while a non-monotonic response (±2%) was observed for LCO material. Cathode expansions identified by XRD experiments were correlated to chemo-mechanical stress generation in SSBs. InLi|LSPS|Li_2S cell was investigated by*operando* energy dispersive X-ray diffraction and tomography[80].The cell was cycled at 1C, 0.5C, 0.25C and 0.1C during the *operando* measurement. During charge process, principle diffraction line of In disappears with the appearance of InLi diffraction peak. Additionally, volume change in the electrode cause build-up/release of stress at the electrode|electrolyte interface causing mechanical degradation.

Diffraction is also utilized to assess conduction pathways and mechanisms in solid electrolytes. The impact of annealing conditions on ion transport properties of Li_2S-P_2S_5 system was investigated using pair distribution function[176]. $75Li_2S$-$25P_2S_5$ glass system showed higher conductivity after annealing and lower conductivity after crystallization (Fig. 15e). The presence of mixed phases was reproduced by differential pair distribution function analysis. Presence of a minority nanocrystalline phase was identified during annealing which leads to an improvement of ionic conduction. High pressure XRD studies of Na_3SbS_4 were carried out to investigate pressure driven structural changes and its impact on ion transport[178]. Increasing pressure from 0.2 GPa to 2.0 GPa leads to shift of the diffraction peaks from Na_3SbS_4 to higher 2θ values and broadening of the peak widths. Tetragonal phase was identified at for all the measured diffraction patterns. a lattice parameter shows a monotonic decrease with pressure while c/a parameter shows a monotonic increase. This indicated an increase in the tetragonal distortion of the solid electrolyte framework. The lattice paramter trends also indicated aniostropic compressibility along the three principal directions with a being most compressible. Ionic conduction increases with pressure due to lower grain boundary resistances. Neutron powder diffraction was used to assess structural changes in Li_6PS_5Cl during *in situ* heating[179]. Room temperature mixture of precursors was amorphous with crystalline peaks of Li_2S adn LiCl. Crystalline argyrodite starts to form at 80 °C and remains crystalline up to 490 °C where it melts/becomes amorphous. The argyrodite

phase recrystallizes on cooling and was stable till 90 °C. Results indicate high annealing temperature and fast cooling were required to reach the nominal compositions. Exothermic reactions of LPS solid electrolyte with $LiNbO_3$ coated NMC111 were investigated by *in situ* high temperature synchrotron XRD[180]. Composite cathode consisting of LPS:NMC (25:75) was initially charged to 3.8 V against In at 0.13 mA cm^{-2}. The charged cathode sample was extracted and investigated by synchrotron XRD in a control N_2 atmosphere as well as vacuum. The diffraction patterns were obtained in the 2θ range of 5°-25° between temperatures of 20 °-500 °C. In N_2 atmosphere, $CoNi_2S_4$, Li_3PO_4, MnS, β-Li_3PS_4 and Li_2S phases appears after 300 °C with a reduction in the NMC phase peaks indicating exothermic reactions between LPS and NMC between 300 °-500 °C. In contrast, no reaction products were observed for the temperature study in vacuum. In particular, the formation of the LPO oxide phase was derived from the LPS reaction with the O_2 gas generated during NMC decomposition. These results dictate the necessity of oxygen tolerant solid electrolytes for practical solid state batteries. Assessing phase formation during processing conditions with diffraction can provide insight into structures that result in high ionic conduction properties and help tailor processing conditions.

Grain orientation and grain boundary misorientations of LLZO were investigated by Laue X-ray microdiffraction[181]. LLZO was synthesized by conventional solid state synthesis and samples with large (100-200 μm) and small (20-40 μm) grain sizes were obtained. Grain size control was afforded by varying the particle size distribution of the powders used for making the cold-pressed pellet. Sintering of green pellets formed by cold pressing of 1 μm size powder leads to larger grain size (100-200 μm) due to improved densification. Addition of larger particles (10 μm) to the green pellets leads to smaller grain sizes (20-40 μm) in the sintered pellets. Laue microdiffraction was carried out on two samples : LLZO with large grain size and LLZO with small grain size. Grain orientation for both samples were completely random and the misorientation angles between neighbouring grains for both samples were statistically identical. While, electrochemical measurements indicated that LLZO with smaller grain size showed improved critical current density (0.13 mA cm^{-2}) and area specific resistance (37 Ω cm^2) compared to LLZO with larger grains (0.04 mA cm^{-2}, 130 Ω cm^2). These results suggested that the difference in critical current density of the two samples did not arise from grain boundary or grain orientations in the two samples. Atomic level LPO|LNMP interface characterization was carried out by synchrotron X-ray crystal truncation rod scattering analysis[182]. LNMO (111) epitaxial thin film growth was verified by the CTR profiles and introduction of LPO amorphous solid electrolyte does not damage the cathode thin films. LPO introduction lowers the cubic lattice constant of the LNMO from 8.23± 0.02 Åto 8.18±0.01 Å. Lower lattice constant for LNMO without LPO deposition arises from lithium deficiency (30%) which gets slightly replenished on LPO deposition. Further quantitative analysis of the CTR profiles indicate an atomically sharp interface between LNMO and LPO that can facilitate Li^+ transport. Comparing LPO|LNMO(11) interface to LPO|LNMO(001) interface, spontaneous migration of Li was lower for the (111) system. Additionally, anisotropy in the interface was observed with (111) system interface showing 5x larger resistance than the (001) interface. Similar study was carried out on the interface of LPO|LCO system to understand the origin of the resistance[183]. Two samples were evaluated corresponding to different LPO deposition rates 105 nm/h at 5 Hz repetition rate and 450 nm/h at 20 Hz repetition rate. Impedance spectroscopy results show the 20 Hz-LPO|LCO

system has a significantly (33x) higher interfacial resistance than the 5 Hz-LPO|LCO system (5.5 Ω cm^{-2}). The origin of the high interfacial resistance was attributed to a dead layer in the 20 Hz-LPO|LCO system with low crystallinity at the interface. These results highlight the need for tailoring the cathode|electrolyte interface with atomic precision to facilitate Li^+ transport through the solid|solid interface.

In situ X-ray diffraction was used to study evolution of the electrode phases in Bi|LiPON|Li thin film solid state batteries[184]. The cell was charged potentiostatically at 0.8 V. Diffraction data indicates presence of a series of phase transitions from Li_3Bi-LiBi-Bi along with presence of phases like Li_2Bi. These results highlight the importance of phase transformations in alloy electrodes and XRD as a tool to investigate binary alloy systems. Similar study was carried out on an Li|Li_3YCl_6|LCO cell[185]. The cell was operated between 3.6-1.9 V at 135 μA cm^{-2} (0.1 C). LCO diffraction peaks show behavior similar to those observed in conventional liquid electrolyte systems with the (003), (006), and (104) peaks shifiting to lower angle while the (101) peak shifting to higher angle. No variation in the signal from LYC solid electrolyte indicated absence of side reactions within the system.

X-ray and neutron scattering has been used to investigate structure and macro-phase separation in polymer and hybrid solid electrolytes as well as for porous electrodes[186,187,188,67,189,190]. Appropriate fitting of the scattering signal provides insight into size and shape distributions of polymer and particle aggregations within hybrid electrolytes. Quasi-elastic Neutron Scattering (QENS) was used to elucidate conduction pathways in $LiBH_4/SiO_2$ aerogels[101]. The results indicate a presence of two different $LiBH_4$ fractions with one exhibiting high lithium and hydrogen mobilities. Presence of this phase might result from interaction with silica via reaction with the silanol groups.

6 Spectroscopic Studies

6.1 X-ray Photoelectron Spectroscopy

Due to the typical interphase formation at electrode | electrolyte interfaces, the surface phenomena plays a crucial role at prompting failures in solid electrolytes. X-ray photoelectron spectroscopy (XPS) is a powerful surface-based technique that enables extracting useful chemical information about surface inhomogeneity, irregularities, electrode nucleation and near-surface variation of composition (Fig. 16a-b). Ex-situ XPS technique is a frequent study to characterize SE coating layers and understand interfacial electrochemical reaction mechanisms. With the exception of garnet-based oxides, most solid electrolyte materials like sulfides, thiophosphates and argyrodites show noticeable chemical transformation during electrochemical cycling. However, *in situ* and *operando* probing in solid-state batteries via XPS can be challenging experimentally due to the buried interfaces. To tackle this challenge, in lab-scale XPS, metallic electrodes (Li, Al and Au) was electrodeposited *in situ* by ion-beam sputtering. *In situ* interphase evolution studies were carried out by XPS using Ar plasma to deposit limited quantity of target material (Li) on the sample(Fig. 16c). Interphase evolution on a thin-film LLTO was investigated with the depth-profiling in XPS (Fig. 16d)[191]. Results indicated that LLTO forms a mixed conducting interphase (MCI) by reaction of Li metal and solid electrolyte material. In case of LLTO, Ti^{4+} reduces to species

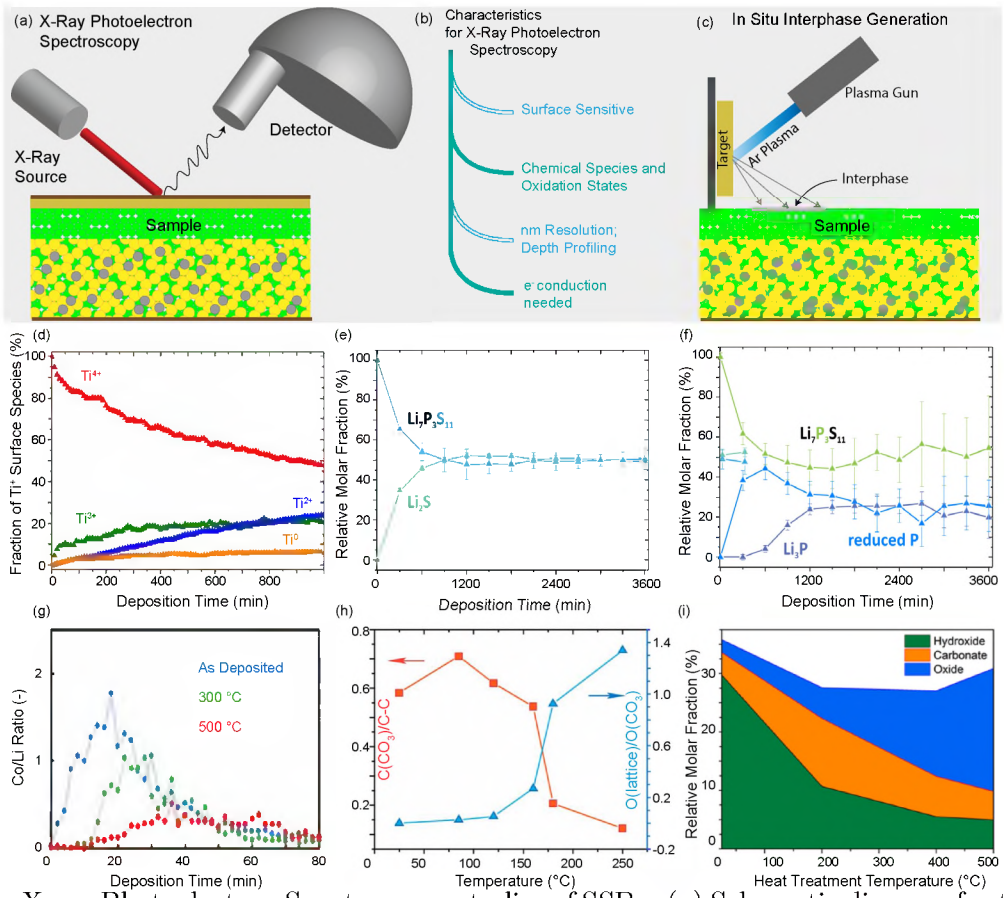

Figure 16: X-ray Photoelectron Spectroscopy studies of SSBs. (a) Schematic diagram for traditional XPS studies. (b) Characteristics of XPS measurements. (c) Schematic diagram of experimental setup devised to investigate interphase formation *in situ* using XPS. (d) Decomposition of LLTO and evolution of reduced Ti species on Li deposition on interface tracked with setup described in (c). Adapted from[191] with permission from Elsevier. (e-f) Decomposition of LPS solid electrolyte and evolution of decomposition products on *in situ* Li deposition. Adapted from[192] with permission from Elsevier. (g) Evolution of surface oxide, carbonate and hydroxide species with heat treatment temperature for LLZO solid electrolyte. Adapted from[193]. Copyright 2017 American Chemical Society. (h) Evolution of surface oxide and carbonate species with treatment temperature highlighting the required temperature to remove surface carbonates. Adapted with permission from[194]. Copyright 2018 American Chemical Society. (i) Depth profile of LCO|LLZO interfaces for thermally treated samples. Adapted with permission from[136]. Copyright 2018 American Chemical Society.

with Ti^{3+}, Ti^{3+}, and Ti^{0} oxidation states. The reduction of the solid electrolyte occurs without any electrochemical biasing and the MCI formation was driven completely by thermodynamic instability between the two materials. Similar characterization was performed on thiophosphate LPS electrolyte to study the gradually formed SEI (Fig. 16e-f). The thin interphases don't go through continuous evolution but was nonetheless, resistive due to the formation of Li_2S and Li_3P via chemical degradation[192,195]. Formation of the MCI in these materials severely limits their applications in SSBs due to the high interfacial resistances. Other amorphous solid electrolytes such as LiPON and NASICON have been probed via XPS as thin-film based battery study[16]. Lithium film was grown on to these surfaces by vapor deposition. In case of LiPON, surface sensitivity of XPS revealed formation of species

such as Li_3PO_4, Li_3P, Li_3N and Li_2O just by physical exposure. Various glass like NASICON ($Li_{1+x-y}Al_x^{3+}M_y^{5+}M_{2-x-y}^{4+}$) electrolytes, while in contact with Li, also undergo degradation reactions leading to an increase in interfacial impedance over time. Depth-profiling XPS showed various mixed conducting interphases, prompted by elemental (Ti, Ge) oxidation state change. It should exclusively be noted that, all of these interfacial changes occurs without any electrochemical contribution.

Garnet-type solid electrolytes such as LLZO ($Li_7La_3Zr_2O_{12}$) and its doped (Al, Ta, Nb, Ga) counterparts, owing to superior stability against electrodes, don't exhibit a distinct interphase region. But due to air-filled processing environment, a thin but insulating Li_2CO_3 layer forms on the pellet surfaces, causing high interfacial resistance from both cathodic and anodic side. The impact of carbonate layer in dictating the performance and characteristics of Li|LLZO interfaces was studied by direct surface probing via XPS[193]. Formation of the carbonate layer was linked to proton exchange of LLZO, formation of Lithium hydroxide and subsequent decomposition to the lithium carbonate (Fig. 16g). The carbonate layer impedes interfacial Li^+ transport, prompting voids formation at the interface and results in electrolyte failure. Quantification of CO_3^- layers showed nanometer scale thin surface region on bulk electrolytes, even after excessive surface conditioning[194]. *In situ* XPS studies on LLZO under varying temperatures have shown that decomposition of the surface carbonate species on LLZO was close to 150 °C (Fig. 16h). The onset temperature of this decomposition was significantly lower than the simple decomposition of Li_2CO_3 to CO_2, which was reported between 620 ° and 1000 °C. Exposing the cleaned surface to air again leads to formation of the carbonate layer suggesting that the process was reversible. These results highlight the need for careful handling and proper surface treatment procedures of garnet oxides to enable low-resistance, efficient Li|SE interfaces. Depth profiling XPS with thermal control was also used to investigate cathode|SE interface stability[136]. Co-sintering of LLZO and LCO materials leads to Co diffusion from the cathode into the LLZO matrix as confirmed by the depth profiling XPS (Fig. 16i). Typical decomposition products expected were Li_2CO_3, $La_2Zr_2O_7$ and $LaCoO_3$. Formation of these decomposition products impede ion transport and can contribute to capacity fade in SSBs.

6.2 X-ray Absorption Spectroscopy

X-ray absorption spectroscopy provides an accurate measure of X-ray absorption coefficient as a function of incident X-rays, in an energy range above and below the absorption range of a selected element of material under investigation. Thus, XAS is an element-specific, local-structure probe which provides information regarding local neighborhood of the element of interest (Fig. 17a-b). Due to the nature of electrochemical processes in a battery (intercalation of guest species into a host lattice), XAS offers a versatile tool to investigate local chemical structure. Investigation of local structure was used to elucidate the origin of performance enhancement of graphite-LPS composite anode prepared by spark-plasma-sintering process[196]. In comparison to a blended graphite, LPS composite, the cells run with SPS fabricated graphite-LPS composite showed improved energy density and rate capability ($\approx$ 600 mAh g^{-1}-Li_2S and $\approx$ 400 mAh g^{-1}-Li_2S respectively). The blended composite showed a broad peak at around 1.6 $\AA$ in the EXAFS spectrum and some long range structure up to 5 $\AA$. In contrast, the graphite-SE composite showed a similar broad peak at

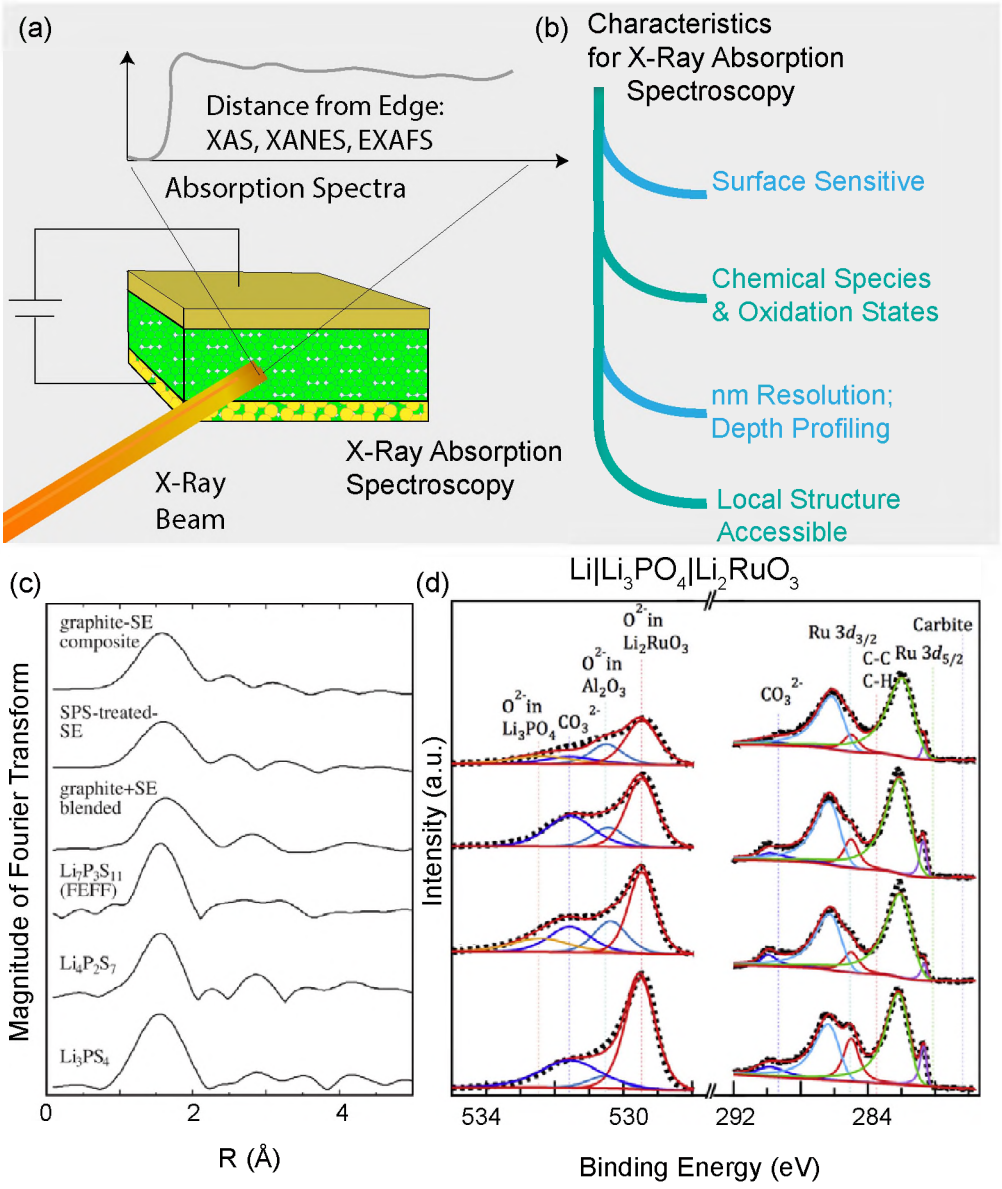

Figure 17: Absorption Spectroscopy Studies for SSBs. (a) Schematic diagram and (b) characteristics for X-ray absorption spectroscopy. (c) EXAFS investigation of composite and spark-sintering processed composite anodes of graphite and LPS solid electrolytes. Adapted from[196] with permission from Springer. (d) XAS investigation of O 1s and Ru 3d peaks for pristine and cycled $Li|Li_3PO_4|Li_2RuO_3$ cell. Adapted from[197] with permission from Elsevier.

1.6 $\AA$ but a different long-rage-order structure (Fig. 17c). This indicates a change in the structural environment around S atoms in the solid electrolyte by the synthesis process. Based on the spectra of reference materials (Li_3PS_4, $Li_4P_2S_7$, $Li_7P_3S_11$), it was proposed that the SPS process leads to an increase in amount of $P_2S_7^{4-}$ ditetrahedra. Such structural change leads to sulfur deficiency in the P_yS_x network leading to reduced coulombic attraction between Li and S atoms improving the mobility of Li ions in the SE. Local structure of

MoS_3 electrodes was investigated using XANES spectra[91]. XANES measurement indicated a reversible electronic structure changes of Molybdenum after cycling. However, S K-edge XANES profile indicated an irreversaible redox of S^{2-} and $S^{\delta-}$ on initial cycle leading to a non-recoverable first discharge. Subsequent cycles of MoS_3|LPSLiIn cell showed stable performance due to reversible redox reactions of Mo and S. Interactions between NMC and LPS materials with and without interlayer cathode coatings was investigated by XANES measurement[198]. XANES spectra of quiescent mixture of uncoated NMC and LPS show evidence of interaction between the materials arising from Li diffusion from SE to the cathode material and formation of an insulating interphase. In contrast, quiescent mixture of LNO-coated NMC and LPS does not show evidence of degradation indicating improved chemical stability. *Operando* XANES spectra of the bare NMC highlights LGPS decomposition to Li_2S during cycling which get successively severe with cycling. On the other hand, XANES spectra for LNO-coated NMC indicate a very stable LCO-LGPS interface in the initial cycles. Similarly, stability of lithium rich layered Li_2RuO_3 cathode with LPS was investigated using XANES measurement (Fig. 17d)[197]. Tracking O 1s and Ru 3d peaks across cycling for pristine Li_2RuO_3, pristine Li_3PO_4|Li_2RuO_3 thin film show no variation in binding energies indicating a stable interphase between the cathode and solid electrolyte.

6.3 Nuclear Magnetic Resonance Spectroscopy

NMR spectroscopy is a powerful probe to characterize ion dynamics and material imaging at atomic level for battery applications (Fig. 18a)[201]. Impact of material processing and cycling conditions on ion transport at electrode|electrolyte interfaces in Li_2S-Li_6PS_5Br and Li_2S system was investigated by NMR measurements[199]. Difference in chemical shift between Li in the cathode and SE phases enable 2D exchange NMR measurements (Fig. 18b). Results indicate an improved ion transport between the SE and composite cathode for the nano-sized SE-Cathode composite compared to the micro-sized cathode composite. Based on experimental results, the exchange current density between the electrode and electrolyte for the nano-sized composite cathode was estimated to be 1 mA cm^{-2} compared to 0.5 mA cm^{-2} for the micro-sized composite cathode. In addition, charging significantly modifies the ion exchange characteristics for the system leading to a less facile ion transport at the solid|solid interfaces. NMR coupled with MRI enables 3D spatial tracking of metallic filament growth through chemical shift imaging. Li filament growth through LLZO solid electrolyte was investigated using ^{7}Li CSI technique[78]. Filament growth was observed in the solid electrolyte continuously upon cycling even below the critical current density (Fig. 18c). In addition, growth of irregular features at both interfaces indicate unstable electrodeposition as well as dissolution. These results indicated heterogeneity at both interfaces suggesting formation of local hot spots during electrodeposition and dissolution. Similar technique was used to investigate heterogeneity of Li distribution in LGPS solid electrolytes[200]. NMR experiments showed a high Li loss at the Li|LGPS interface upon electrochemical cycling (Fig. 18d). This decrease was found to be asymmetric with the top interface showing a 40% decrease while the bottom interface shows a 20% decrease in Li content. In comparison, a PEO-coated system shows only ≈10% decrease in Li concentration at the interface. This decrease in interfacial Li content leads to increased interfacial resistance subsequently impacting the filament growth through the solid electrolyte. While no changes were observed in the bulk Li concentration,

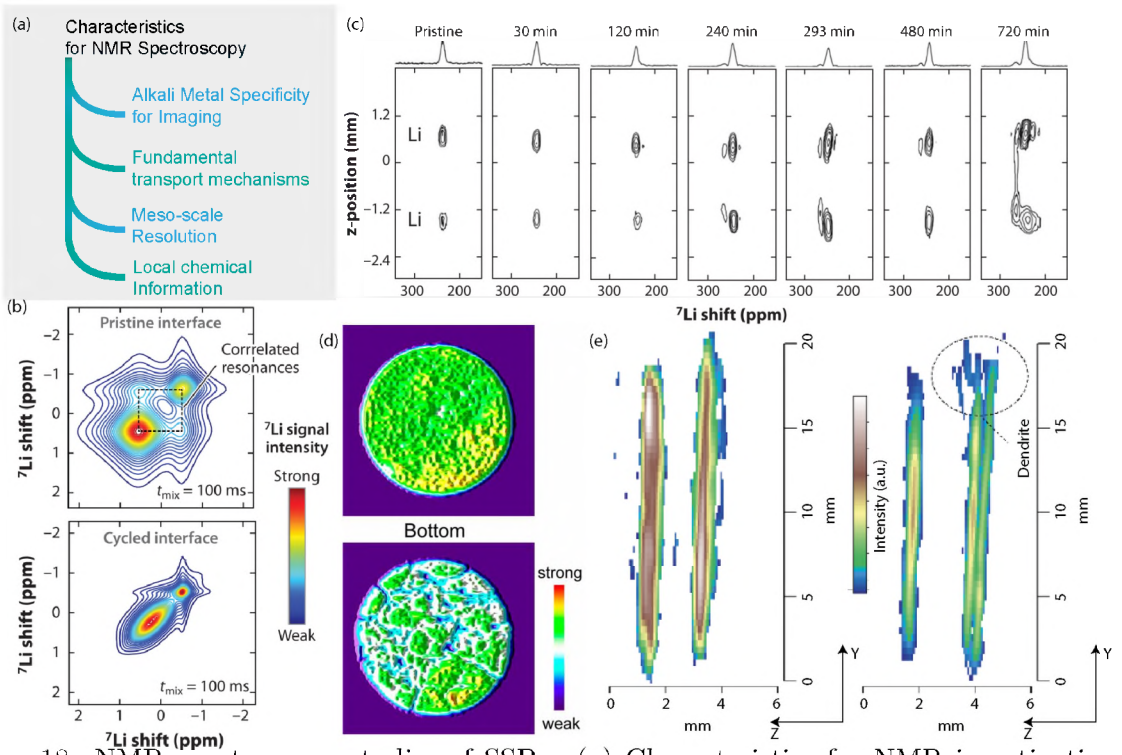

Figure 18: NMR spectroscopy studies of SSBs. (a) Characteristics for NMR investigations. (b) 2D EXSY plot for pristine and cycled Li_2S-Li_6PS_5Br and Li_2S system. Adapted from[199] with permission from Springer. (c) Li filament growth in LLZO solid electrolyte visualized by ^{7}Li chemical shift imaging. Adapted from[78]. Copyright 2019 American Chemical Society. (d) Li loss at LGPS|Li interfaces investigated by ^{7}Li chemical shift imaging. Adapted from[200]. Copyright 2018 American Chemical Society. (e) Na filament formation imaged in Na β-alumina solid electrolyte by ^{23}Na chemical shift imaging. Apapted from[172] with permission from Wiley.

homogeneity of Li distribution was largely affected after electrochemical cycling. Similar investigations were carried out for Na-based SSBs for Na β-alumina electrolyte[202]. Spin-spin (T_2) characteristics for bulk electrode (5-10 ms) and filaments (>12 ms) were appreciably different allowing for resolving dendrite growth in solid electrolytes. Results indicate presence of dendrite of length-scales corresponding to 10s to 100s of nm which were otherwise indistinguishable from other meso-scale characterization techniques (XRT).

6.4 Raman Spectroscopy

Raman spectroscopy is a powerful technique that can provide spatially and temporally resolved information regarding vibrational, rotation and other low-energy modes of surface molecules (Fig. 19a-b)[46]. This technique is particularly useful for carbon, oxygen and hydrogen as well as polysulfide surface species. Reaction distribution within composite LCO-LPS was investigated by Raman spectroscopy[203]. Upon charging of the composite cathode, Raman imaging showed presence of unreacted, low SOC LCO regions within the composite cathode (Fig. 19c). Improper contact between the solid electrolyte and cathode active material was identified as the cause of low utilization and heterogeneous reaction distribution. Modification of processing protocols to ensure optimal contact between SE

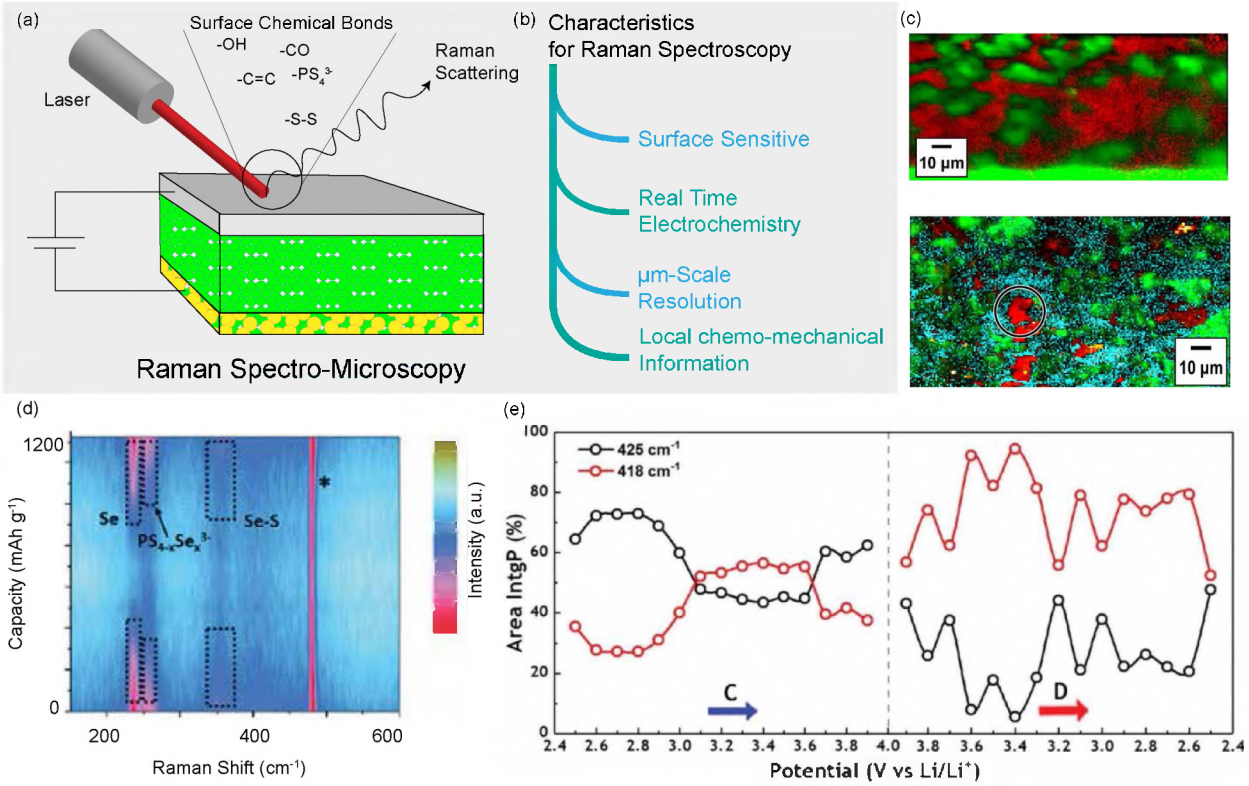

Figure 19: Summary of Raman spectroscopy characterization in Solid State Batteries. (a) Schematic and (b) characteristics of Raman spectroscopy studies. (c) Raman mapping of LCO composite electrode before and after charging. Adapted from[203] with permission from Elsevier. (d) *In situ* Raman contour plots for Se|LPS|C cells. Reproduced from[204] with permission from The Royal Society of Chemistry. (e) Interfacial changes in NCM|Li_6PS_5Cl|Li during cycling investigated by Raman spectroscopy. Adapted from[205] with permission from Wiley.

and cathode active material was required to achieve high utilization cathodes. Similarly, Raman spectroscopy of Li|LPS|LCO cells was carried out to assess the structural change in the cathode[206]. Raman measurements were carried out from front and back surface of the cell where in intensity and peak changes were observed in the Raman spectra reflecting the increase in c-axis lattice parameter of LCO. Additionally, a large hysteresis was observed in the charge-discharge maps which was proposed to arise from the diffusion time of Li ions within the cathode - reflecting the time delay of electrochemical and Raman measurements. Raman spectroscopy was used to investigate Se|Li_3PS_4|C system[204]. Raman spectra showcased the formation of an interphase containing $PS_{4-x}Se_x^{3-}$ species. During charging, Se_n chains and $PS_{4-x}Se_x^{3-}$ undergo different extent of lithiation as evidenced from Raman mapping. which was found to be reversible (Fig. 19d). This electrochemical mechanism was distinct from Se mechanisms in conventional liquid electrolyte systems and was unique to the solid-state system. Effect of space charge layer in NCM|Li_6PS_5Cl|Li was investigated by Raman spectroscopy[205]. *Operando* Raman spectroscopy revealed that structural change of solid electrolyte at the interface was limited to vibration of PS_4^{3-} tetrahedra in the early cycling stages (Fig. 19c). The stability of the interface was afforded by the presence of S^{2-} and PS_4^{3-} in the solid electrolyte crystal structure. On Long term cycling, characteristic

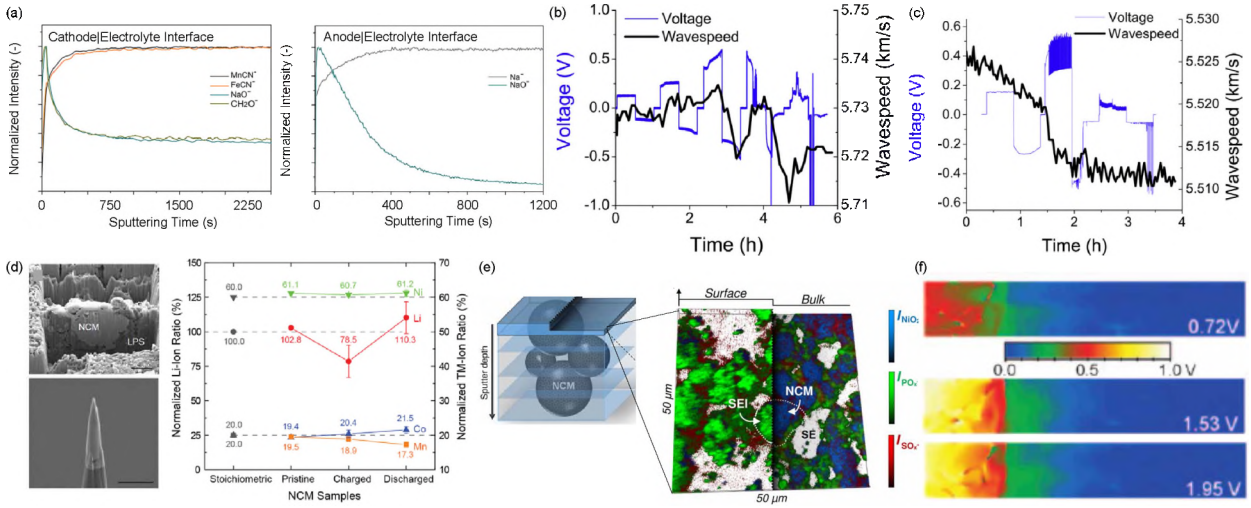

Figure 20: Summary of miscellaneous characterization techniques used for solid state batteries. (a) Anode and cathode interfaces for $Na_2MnFe(CN)_6|Na_3Zr_2Si_2PO_{12}|Na$ were investigated by TOF-SIMS. Nano-scale interphase formation is evidenced with species like $MnCN^-$, $FeCN^-$, NaO^- and CH_2O^-. Adapted from[207] with permission from Elsevier. (b) Acoustic investigation of Li filament formation in LLZO symmetric cells. Adapted from[208] with permission from Elsevier. (c) Atom probe tomography investigations of nano-scale lithiation differences in NMC samples. Adapted from[209] with permission from Elsevier. (e) TOF-SIMS depth profiling of composite cathodes indicating differences in lithiation and SEI formation at the interface and sub-surface regions in NCM-LPSCl cells. Adapted from[76]. Copyright 2019 American Chemical Society. (f) Electric potential variations during charging of a LCO|LATP solid state battery investigated by electron holography. Adapted from[68] with permission from Wiley.

response of the solid electrolyte units (PS_4^{3-}) were observed in the interior of NMC particles suggesting significant deterioration of the cathode particles and diffusion of SE into the interior. Similarly, degradation of LCO|LPSCl|Li was investigated by Raman spectroscopy[172]. During charging, Raman mapping showcased the formation of interphase in the system with decomposition products comprising of Li_2S, P_2S_5 and polysulfides.

7 Additional Characterization Techniques

In addition to conventionally known characterization techniques, several new techniques are being leveraged to study buried interfaces in SSBs. Time-of-flight secondary ion mass spectrometer (TOF-SIMS) is extensively used to assess chemical distribution at nm-level for ion distribution in cathodes, solid electrolytes and interfaces[210,211,212,213,214,36,215,216,217,218,219]. Anode and cathode interfaces in $Na_2MnFe(CN)_6|Na_3Zr_2Si_2PO_{12}|Na$ were investigated by TOF-SIMS[207]. Limited reaction between Na and solid electrolyte was observed with formation of a thin NaO^- interphase (Fig. 20a). The formation of this interphase was proposed to improve Na metal wettability and promote stable electrodeposition/dissolution during the working of the solid state battery. At the cathode interface, products of polymer degradation at high voltages (3.7 V vs Na^+/Na) were observed with $MnCN^-$, $FeCN^-$, NaO^- and CH_2O^- species. The interphase at the cathode was also thin and the decomposition products do not

show evidence of dissolution of transition metal from the cathode indicating protection of the cathode. Depth profiling of the interface by TOF-SIMS of an NMC|LPSCl|Li cell highlights that the SEI layer in these system comprises of PO_x^- and SO_x^- species (Fig. 20e)[76]. The interphase thickness around the NMC particles was estimated to be around 10 nm. Microstructural changes in solid electrolytes was investigated by acoustic characterization methods[208]. Acoustic wave speed in a medium is dependent on the elastic properties of the medium. On changes to the microstructure of the material with formation of cracks/filaments or other lower modulus defects, the wavespeed through the material decreases measurably allowing to reveal microstructural changes non-destructively. Acoustic techniques are also useful for determination of mechanical properties of materials[220]. A decrease in the stiffness of LLZO (reduction in wavespeed) in the minutes prior to failure, with the rate of stiffness decrease being proportional to the applied current density (Fig. 20b-c). The decrease in wavespeed (stiffness) was correlated to generation of fracture in the solid electrolyte. Such techniques are proposed to be useful for online battery management systems to isolate and mitigate failing cells from battery packs prior to short circuit.

Atomic level chemical resolution for elemental species is achieved by atom probe tomography (APT) which is recently being leveraged to investigate local features[209] . Difference in lithiation of NMC cathodes in solid state batteries were invesitgated by APT. A significant variation ($\approx$ 15%) was identified in Li-ion concentrations in different NMC specimens investigated (Fig. 20d). These variations were anticipated to arise from poor solid electrode-cathode active material contact in the composite cathode. Local Li concentration profiles in Pt|LATP-LAGP|LCO|Au battery was investigated using elastic recoil detection (ERD) and Rutherford backscattering spectrometry (RBS)[221]. RBS and ERD measurements were collected from the surfaces of both Au and Pt electrodes. Li reduction from LCO to a composition of $\approx$0.3 was identified during initial charging while an anomalous reduction was observed on further positive biasing. Discharging subsequently leads to enrichment of LCO over the depth of LCO. Insulating interphase formation between LATP and LCO (1.0 V) during initial charging and subsequent concentration gradient formation leads to counter flow of Li^+. Similar study was carried out on a Pt|LATP|LCO|Au thin film battery[222]. A lithium depletion region of 120$\pm$3 nm was identified in the solid electrolyte at the LATP|LCO interface at the charged conditions. Since the charging cut-off was lower than the decomposition voltage of LATP, the depletion region was anticipated in LATP without active decomposition. Additionally, H presence was detected around both electrodes which can potentially disrupt Li^+ transport and rate capabilities of SSBs.

Electron holography (EH)is a technique that can enable quantification of local electric potential within solid state battery with nm spatial resolution[223,69,224,225]. EH study of LCO|LATP interface during charging showed that potential drop was primarily focused at the interface and the electrolyte bulk potential does not vary during charging (Fig. 20f). EH showcases the formation of space charge layer dictated by the Debye length due to the difference in ion transport properties of electrolyte and the cathode material[68]. This results in a steep drop of potential at the electrode|electrolyte interface. APT and EH techniques were combined to investigate the impact of dopant impurities in the grain boundary of solid electrolytes on the space charge layer formation[69]. Grain boundary in a Sm-doped ceria material was found to possess a 20 nm thick grain boundary showing a positive space charge layer with a peak potential of 0.9 V. APT studies of the grain boundary shows an increased

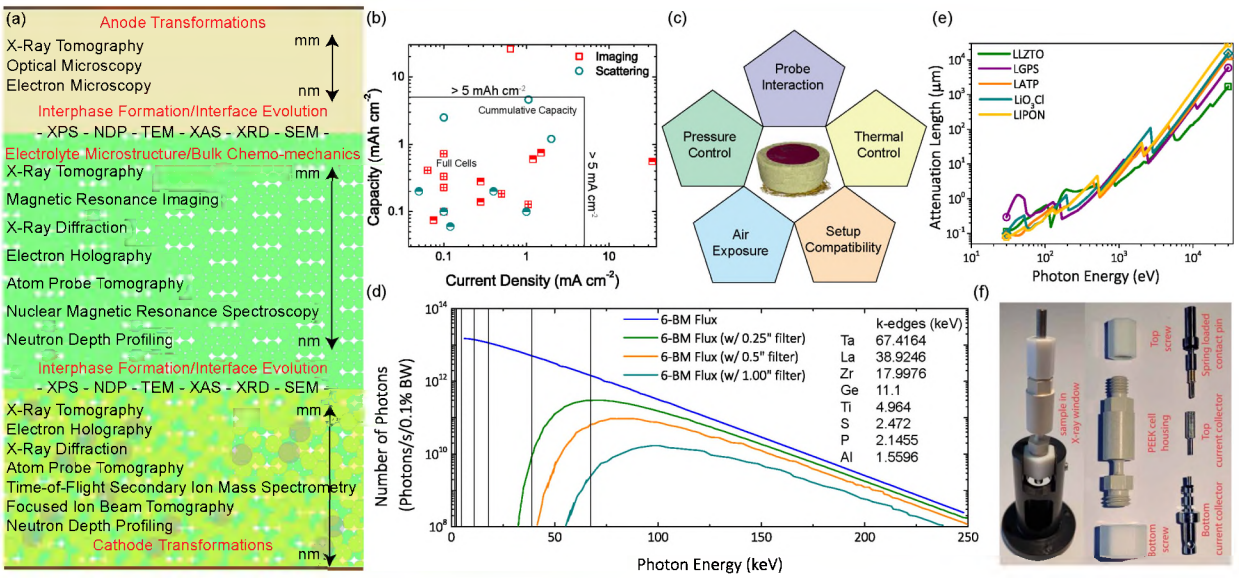

Figure 21: Experimental Design Considerations. (a) Summary of techniques used to investigate SSB components. (b) Experimental spread of current density and capacity charged employed in reported *in situ* and *operando* experiments. (c) Schematic diagram highlighting the different aspects that are important while designing *in situ*/*operando* experiments. (d) X-ray beam energy at a typical synchrotron endstation (6-BM, APS) with different filters. Absorption edges of typical SSB elements are also shown. (e) Attenuation length for typical solid electrolyte materials as a function of beam energy. (f) Typical *in situ* cell for X-ray experiment.

concentration of impurities like Si, Al, Ca as well as the dopant Sm, compared to the bulk. Such local hot-spots can drive failure in SSBs by driving preferential motion of ions through regions of high/low potential.

Thermal analysis of solid-state battery materials is typically carried out using thermal gravimetric analysis and differential scanning calorimetry measurements. These techniques involve heating the sample in a controlled environment while measuring mass change and/or heat release from the system. This measurement can be combined with a gas chromatograph-mass spectroscopy instrument to analyze the generated gases to identify thermal decomposition products. In situ heating can also be carried out during diffraction/scattering experiments to analyze structure and phase evolution in solid-state battery materials under different thermal environments.

8 Experimental Design

Underlying physical phenomena in SSBs occur over cascading length- and time- scales over several orders of magnitude. The current review highlights the range of techniques used to probe individual components and assembly of SSBs in *in situ* and *operando* conditions (Fig. 21a, Table 1). These techniques are employed to investigate specific time- or length- scales in SSBs which imparts certain restrictions in terms of operating parameters of the battery. It is imperative to understand the implications arising from battery geometries designed for specific *in situ* experimentation and their deviation from system-level batteries (coin-cells,

pouch cells). Particularly, of concern in SSB technology is the need for stack pressure and operating temperature at the lab-/system- scale that is difficult to translate to *in situ* or *operando* experiments. The differences in field configurations, operating conditions, electrochemical testing protocols can lead to misguided interpretation of experimental results from the characterization techniques. Survey of electrochemical performance metrics (capacity, current density) of *in situ/operando* measurements highlights this discrepancy (Fig. 21b). For SSBs to be technoeconomically competitive with conventional Li-ion batteries they need 5 mAh cm^{-2} capacity in a single charge/discharge at $\geq$ 5 mA cm^{-2} current density[26]. Most *in situ* and *operando* measurements are performed at one/two orders of magnitude lower capacities and current density. It is vital to design and conduct *in situ* and *operando* characterization at technologically relevant conditions in order to probe electro-chemo-mechanical phenomena of interest at conditions as close to actual systems as possible.

Experimental design for *in situ* and *operando* characterization needs to control and optimize in order to ensure representative studies of materials under investigation (Fig. 21c). A wide range of reports with different solid electrolyte materials have highlighted the need for high operating pressures as well as temperature for effective cycling of SSBs[28,29,31,84]. These operating conditions ($>$ 50 °C, 5-20 MPa) are typically significantly different from conditions of *in situ/operando* testing (RT, kPa). Operating pressure and temperature can significantly impact the kinetics, transport, chemical reaction as well as mechanical response of the SSBs. Thus, it is of particular interest in SSB to enable pressure and temperature control during characterization. In addition to this, the experimental design needs to be compatible with the experimental setup for characterization and maximize the material interactions with probe to enable high signal to noise ratios. In order to illustrate this, an example for cell design and parameter optimization for X-ray experiment is discussed. Synchrotron sources provide a near continuous energy spectrum of X-rays that can be leveraged as a broadband spectrum or a single wavelength can be selected for experiments (Fig. 21d)[71]. Whilst using a broadband spectrum, it is necessary to ensure that presence of photons at absorption edges of investigated material does not adversely effect the electrochemical performance of the system. For reference, energy spectrum at 6-BM beamline of Advanced Photon Source with different filter thicknesses is showcased along with absorption edges of elements from LLZTO material (Fig. 21d). Similarly, probe effects on the sample is of concern when carrying out experiments with probes like electron beams and neutrons which can cause degradation of investigated materials. Signal-to-noise ratio and sample size for X-ray experiments is determined by the attenuation length of the material (Fig. 21e). Accessible X-ray energy dictates the maximum sample sizes that can be employed to ensure a minimal required contrast for X-ray imaging. Careful optimization of such experimental parameters can enable accessing data-sets that are otherwise difficult to obtain[84]. Finally, the cell design is also a key aspect that needs to integrate the experiment design aspects discussed here into a functional cell that can reliably perform electrochemistry during *in situ/operando* testing. It should be noted that universal design criteria for experiment design are not possible due to the varied nature of techniques employed for investigation of SSBs. However, the aspects discussed here are vital to consider while designing and performing *in situ* and *operando* characterization of SSBs.

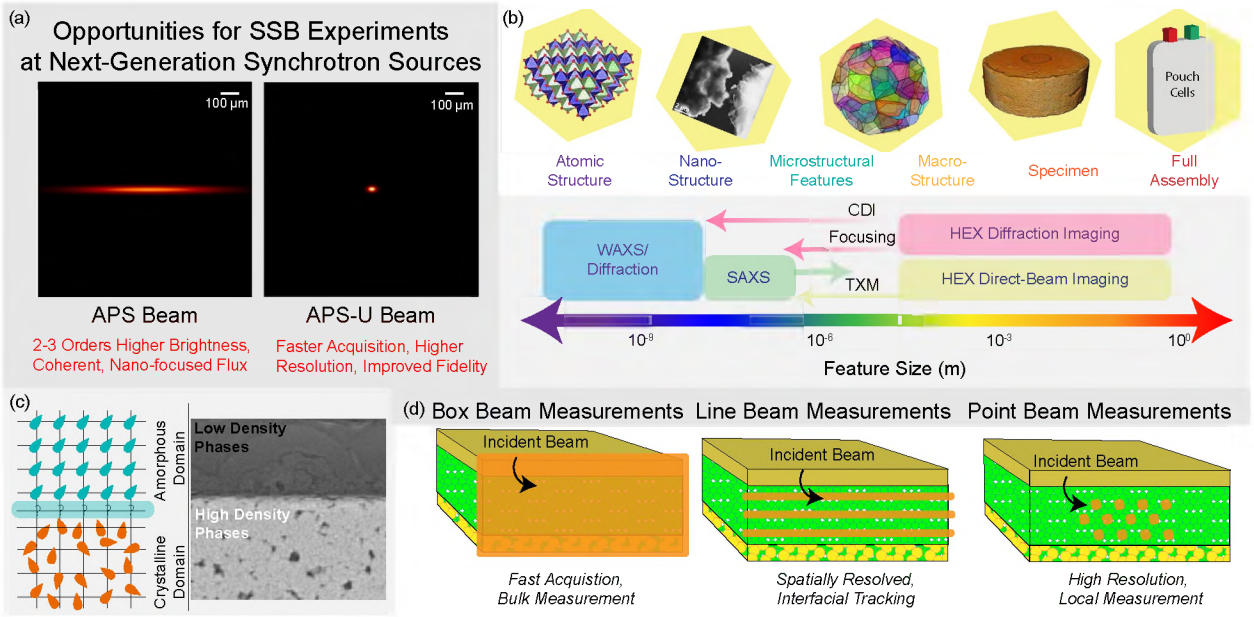

Figure 22: Emerging Characterization at synchrotron sources. (a) Beam configuration at APS with current storage ring configuration and the expected source after the upgrade. (b) Size and scale factors for key scattering techniques and the impact of upgrade on resolution of the techniques. (c) Key challenges in SSBs that require improved characterization techniques. (d) Experimental configuration and expected insight from the experiments. Individual or combination of such experiments in combined scattering, spectroscopy and imaging setting are expected to provide a facile method towards investigating the challenges identified.

9 Emerging Characterization Capabilities using Synchrotron Sources

Many synchrotron facilities around the world are pursuing technologies that will reduce the emittance of the stored beam thereby reducing the x-ray spot size and the improving the x-ray coherence, flux and brilliance[226,227,228]. Improved coherence, flux, and brilliance at these new generation synchrotron sources will enable a wide range of enhanced capabilities for existing techniques and provide opportunities to deploy new x-ray techniques that were previously inaccessible (Fig. 22b). This section outlines emerging and future capabilities at synchrotron sources relevant for SSBs. In this section, we focus on developments at the APS which are illustrative of emerging capabilities at synchrotron sources that are upgrading to a diffraction-limited storage ring. These new capabilities will provide new insight into how SSBs function and fail and help address technical challenges. X-ray techniques also have a favorable temporal frame when compared to the processes occurring in batteries. Timescales of typical x-ray experiments are ms to minutes which is comparable to cycling rate of a battery (2 hours for 1C charge-discharge). This allows for *operando* measurements to assess physical, chemical, and mechanical transformation occurring in SSBs[71,85,84]. In contrast, free electron laser sources typically are employed for very high temporal resolutions (fs-ns) over which no appreciable transformations are expected in SSBs[229]. Such sources may be employed for single-particle kinetic studies for lithiation/delithiation mechanisms.

One of the major experimental challenges in SSB community pertains to simultaneous

characterization of amorphous and crystalline materials (Fig.22 c). Crystalline|amorphous interfaces are expected to be an integral part of SSBs, especially within composite cathodes. Limited characterization techniques of such interfaces in bulk systems are available. Similarly, capturing the morphological evolution of low-Z and high-Z materials within proximity of each other in an anode interface is a considerable experimental challenge[84]. These challenges can be addressed with novel x-ray detector technologies with unprecedented dynamic range and temporal resolution[230]. These photon counting detectors are capable of observing both the intense Bragg peaks and their tails simultaneously. Furthermore, these detectors equipped with scintillation materials sensitive to high-energy x-rays are already available at synchrotron sources. The combination of high-energy x-rays and photon counting detectors that are sensitive to high-energy x-rays means that heterogeneous SSB systems can be investigated *operando* using XRD or PDF measurements as well as interface or surface scattering methods. Specialized optics components such as conical/spiral slits[231,54,232,233] for x-ray diffraction using monochromatic x-rays or energy dispersive diffraction[234,235] can also be leveraged to isolate a specific internal location in a sample to assess the transformations therein. The experimental techniques employing these specialized optics components will be significantly faster in the future.

Novel characterization techniques such as High-Energy Diffraction Microscopy (HEDM)[236,237] and Scattering Tomography[238,239,240,89] are capable of providing grain-resolved and grain-averaged 3D map of SSB systems. Currently, these techniques are capable of 10 um spatial resolution but require hours of scan time[55,241]. Novel detector technologies combined with focusing optics and improved source characteristics in the fourth generation synchrotron sources is anticipated to push the spatial resolution of these techniques to sub um scales and reduce the scan times by orders of magnitude thereby allowing *operando* and *in situ* studies. Box-beam measurements typically provide bulk information which are instrumental in assessing accurate phase information with high resolution scattering data. Similarly, full-field absorption or phase contrast tomographic imaging is always useful to acquire first order the internal morphology of the sample. APS-Upgrade (APS-U) is likely to provide improved resolution for CT techniques (100 nm from 1 m) while retaining the ability to scan mesoscale objects. It should be noted that region of interest (highest resolution section) scales with resolution however the total FoV is unhindered. Diffraction microscopy will show similar improvements at the new High Energy X-ray Microscopy (HEXM) beamline which employs a long "source-sample" distance to improve the focal size and coherence of the beam resulting in high resolutions and increased Q-space accessibility based on the configuration of the endstation. Current high energy diffraction microscopy is limited to samples with micron-level grain size to get grain resolved information with limited intra-granular information obtainable. With the improved coherence, coherence enhanced HEDM techniques wherein HEDM and Bragg coherent diffraction imaging (zoom-out / zoom-in feature) can be combined to obtain intra-granular information at nm length scale. While there is some work done from lower energy Bragg coherent diffraction imaging (BCDI) looking at battery material, it is typically not at bulk / functional size scale. Coherence enhanced HEDM will allow for probing larger samples which can reach meso-/macro- scale compatible with the increased instrumentation needed for SSB operation (high temperature, pressure requirements). Such techniques will be crucial for assessing inter/intra- phase boundaries due to the varying scattering signals emanated from the phase domains and boundaries. Scattering

tomography, dark field microscopy, HEDM as well as BCDI can help resolving intragranular information and resolve grain boundary evolution in bulk samples. With material systems with nano-crystalline components (composite cathodes, hybrid electrolytes), scattering tomography techniques can provide internal field (spatially heterogeneous phase composition / spatially heterogeneous orientation distribution / spatially heterogeneous internal strains). Faster detectors and increase in flux with APS-U will improve the availability of these techniques with the opportunity for *in situ* / *operando* work.

Increased lateral focus of the beam (Fig. 22a) will aid in pushing the resolution of imaging techniques to near TEM levels ($\approx$ 5 nm) with new beamlines (ATOMIC, Ptycho, ISN)[242]. These beamlines will employ nano-focused beams to carry out scattering assisted imaging techniques like ptychography and Bragg coherent X-ray imaging to assess particle morphology, phase and internal strain field. Typically, large acquisition times and need for nano-scale cell assembly makes these techniques difficult to probe SSBs that operate at higher pressures. Higher flux of the beam facilitates instrumentation/assembly required for *operando* studies (multi-component system, cell casing, electrical connections, pressure jigs). Transmission X-ray microscopy can be combined with spectroscopy techniques to provide chemical information about the samples. These techniques are crucial towards *operando* studies to assess transformation in single/few- particles within a system. Several reports for BCDI studies of cathode particles are reported that showcase the ability to assess spatial distribution of lithiation and strain fields in cathode materials. Improved coherence of the x-ray beam in the new synchrotron sources will also allow new *in situ* and *operando* imaging techniques. For instance, Bragg coherent diffraction imaging (BCDI) is currently available at lower energy x-rays. This technique has been used to map the shape and internal strain field of a nm length scale particle used in catalysts or batteries. With improved coherence at higher energy x-rays, BCDI can be used to map individual particle embedded in a complex system like SSB. In fact, HEDM combined with BCDI will provide a versatile probe where mesoscale the 3D map can be attained via HEDM to look for "bad-neighborhoods" in a SSB and BCDI can be used to study the individual particles in the "bad-neighborhood" in finer detail.

For crystalline materials, diffraction techniques at both low or high energies are available with length scale going from sample scale (wide angle x-ray scattering, WAXS) to grain-resolved (inter- and intra-granular) HEDM. Standard WAXS can be used to characterize the "bulk" behavior - strain / texture / peak width measurements. Additionally, if the lattice parameter or the feature of interest is large, high energy small angle x-ray scattering (SAXS) can be employed which will be available at long beamline (HEXM). For amorphous materials, high energy X-rays providing larger q- coverage can be leveraged to capture pair distribution functions to assess local structure within the materials. Using point beam measurement approach (Fig. 22d) 3D spatially resolved studies can help resolve crystalline|amorphous interfaces in SSBs. Surface as well as buried interfaces can be probed through low- and high-energy scattering studies in grazing incidence modes, along with techniques like X-ray depth profiling. It should be noted that this is not an exhaustive list of enhancements/capabilities expected with next generation light sources. Close interactions of instrument scientists with battery scientists are expected to yield facile techniques to study a specific aspect of the material system. Characterization techniques that use X-rays is anticipated to be integral in investigating operational transformations in SSBs in the future.

10 Data Analysis and Analytics

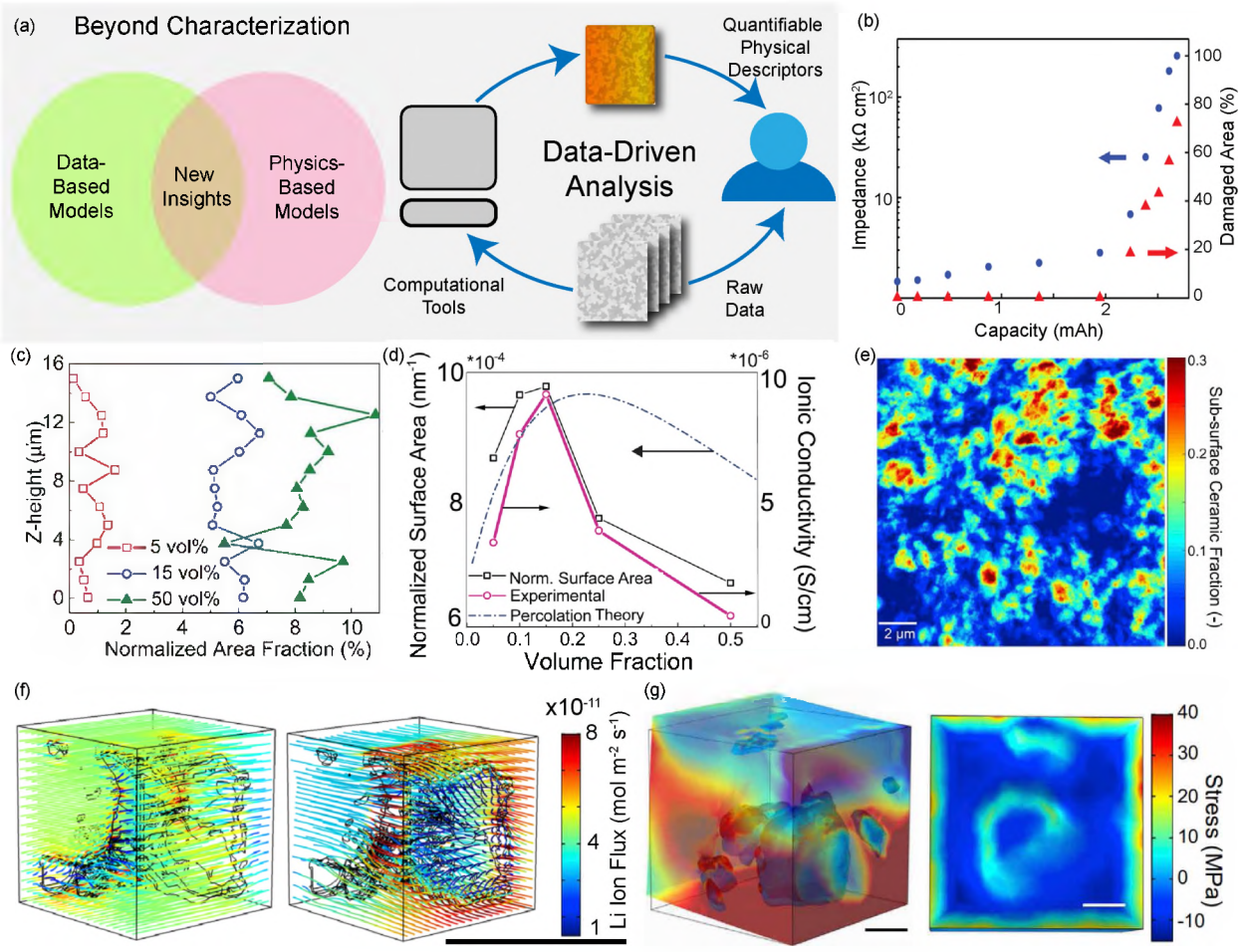

Figure 23: Summary of data analysis and analytics. (a) Schematic diagram motivating the need for advanced data-driven analysis and combining physics- and data- based models (b) Correlation between damaged area in LAGP solid electrolyte measured by *in situ* XRT and cell impedance. Adapted with permission from[34]. Copyright 2019 American Chemical Society. (c) Spatially resolved particle fraction in LLZO–PEO hybrid electrolytes with varying ceramic loading. Adapted with permission from[86]. Copyright 2019 American Chemical Society. (d) Correlation between measured ionic conductivity of hybrid electrolyte and the normalized surface area of ceramic particles measured by nano tomography. Adapted with permission from[86]. Copyright 2019 American Chemical Society. (e) Sub-surface distribution of ceramic particles in hybrid electrolyte identified by nano tomography. Adapted from[79] with permission from Elsevier. (f) Flux distribution around pore networks for LLZO sintered at different temperatures evaluated using CFD simulations. Adapted with permission from[72]. Copyright 2019 American Chemical Society. (g) Heterogenous mechanical response of hybrid electrolyte evaluated from experimental data obtained from nano tomography. Adapted from[79] with permission from Elsevier.

In situ and *operando* characterization typically generate extensive data-sets that are cumbersome to effectively analyze completely. Generally, snapshots of the data-sets are used to generate qualitative insight into the mechanism/physics being investigated. A typical example is of a tomography data-set: while a single tomography data-set provides 3D information

for regions as large as 1.2x1.2x1.2 mm^3; only a small sub-volume (0.3x0.3x0.3 mm^3) was evaluated to generate quantitative insight[71]. This utilizes a very small fraction of the available data set which can be leveraged to generate additional insight into the physics of the investigated material. This data discrepancy is anticipated to exist in most imaging experiments where available data-sets are significantly larger than the fraction used to generate qualitative insight into the mechanism. Combination of data-driven models and physics-based models is proposed to provide a way to leverage large data-sets to generate new insight into the physics of the material systems (Fig. 23a). The primary requirement in this context is to enable data-driven quantification that can enable dimensionality reduction of the raw data into quantities that can be correlated to measurable quantities evolving during cycling of the SSB (viz. capacity, resistance, current, potential, among others).

Damaged area of a LAGP imaged by XRT was evaluated during the course of cycling which shows a strong correlation with the measured cell impedance (Fig. 23b)[33]. Loss of contact with Li as well as increased tortuosity of the solid electrolyte from the cracking as evidenced by XRT leads to the increase in the cell impedance. Heterogeneity in ceramic loading in LLZO-PEO hybrid electrolytes was investigated by nano-tomography (Fig. 23c)[86]. Spatially resolved particle fraction profiles indicate large degree of agglomeration on increasing the ceramic loading. This leads to a loss of accessible particle area for higher loading hybrid electrolytes which correlates very well with ionic conductivity of the hybrid electrolytes. It was proposed that improvement of ionic conductivity of polymer electrolytes by ceramic addition occurs through Lewis acid interactions of the surface hydroxides with EO chains of the polymer leading to a dissociated Li^+ with improved mobility. Increasing loading of the ceramic leads to a maximum of accessible surface area (highest conductivity) beyond which agglomeration leads to loss of accessible area resulting in loss of ionic conductivity. The sub-surface heterogeneity of ceramic particle distribution was correlated to interfacial mechanical properties that dictate electrochemical performance of hybrid electrolytes (Fig. 23e)[79]. Impact of ceramic particle distribution of mechanical response was also investigated by CFD simulations which show disparate stress generation in hybrid electrolyte across the three dimensions due to anisotropic ceramic distribution (Fig. 23g). CFD simulations were also used to investigate Li flux distribution across LLZO sintered at different temperatures (Fig. 23f)[72]. Highly anisotropic flux distributions for the tortuous pore network leads to accelerated failure from filament growth and lithium nucleation in the pores.

Large data-sets also enable use of advanced computing methods like machine learning (ML) and image processing[84]. ML enables segmentation between low contrast phases of lithium metal and pores within Li|LLZO|Li cells (Fig. 24a). ML segmented images enable quantification of both electrodes that clearly show proof of pore formation within lithium metal during stripping and pore filling during electrodeposition steps (Fig. 24b). While *ex situ* evidence of this mechanism were reported previously[28,29], ML and tomography experiments enable meso-scale insight into Li metal transformations. Interfacial contact of Li and solid electrolytes can also be perceived by intensity maps that enable qualitative comparison of the interfacial evolution (Fig. 24e)[85]. Recently, thickness of Li metal was tracked to provide insight into charge cycled in symmetric LPS cells and was the variation in the charge cycled between the two electrodes was correlated to active Li present in cracks that grow through the thiophosphate solid electrolytes (Fig. 24c)[85]. Large-area evaluation of current density in Li metal was carried out which enabled identification of hot-spots in the system

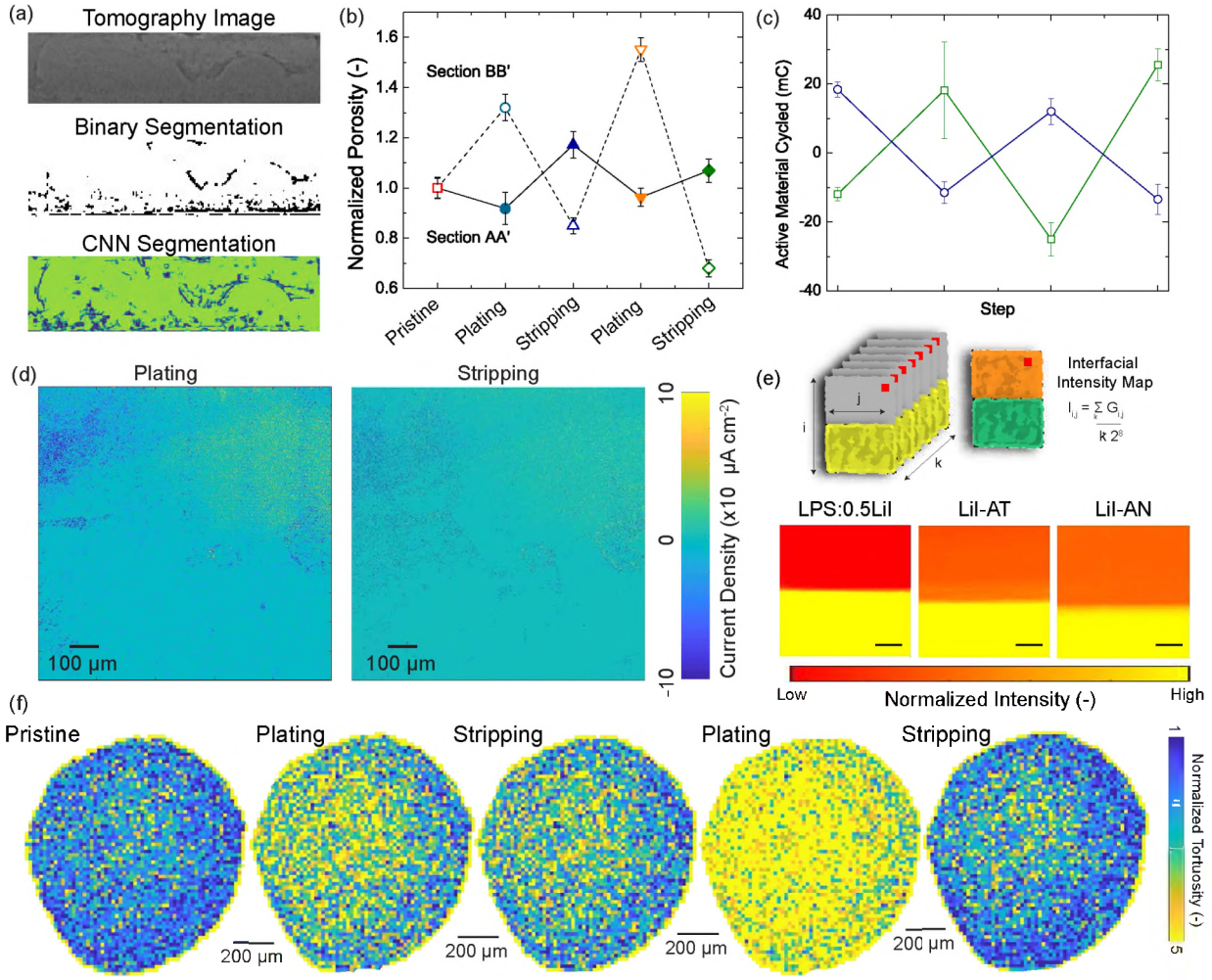

Figure 24: (a) Raw reconstruction, binarized image and CNN segmentation of Li metal electrodes imaged by XRT. (b) Pore formation in Li metal electrode for both working and counter electrodes measured from the ML segmented images during cycling. (c) Active material cycled in symmetric Li|LPS|Li cells measured from XRT data. (d) Spatial current density maps for plating and stripping steps for Li metal measured from XRT data. (e) Interfacial intensity maps for Li|solid electrolyte cross-sections highlighting conformal solid electrolyte and lithium metal. (f) Tortuosity maps of solid electrolyte during electrochemical cycling. Images adapted from[85,84]. With permission from Elsevier. Copyright 2020 American Chemical Society.

that could potentially lead to filament formation (Fig. 24d)[84]. These hot-spots were correlated to regions with disparate microstructure in the underlying solid electrolyte which were evaluated by mesoscale simulations. Piecewise tortuosity simulations of interfacial region of the solid electrolyte also reflects this behavior showing local variation in tortuosity as well as modulating tortuosity maps with cycling (Fig. 24f).

Material identities are crucial in dictating performance of solid-state batteries (SSB). As discussed extensively in this review, the electro-chemo-mechanical processes in SSBs are strongly dependent on the design of component interfaces across multiple length and time-scales. Combinatorial approach to selecting materials yields a non-exhaustive set that becomes unfeasible to experimentally evaluate. Data science methods can help in discovering,

uncovering underlying physics by interpolation / extrapolation of known data-sets. Multi-modal characterization and simultaneous electrochemical testing of exemplary solid-state battery materials is expected to generate an exascale, coupled, multi-dimensional data-set that can provide the basis of high-fidelity data-driven models. For example, a material database for solid electrolyte materials can include modalities/parameters like space group, lattice parameters, elemental composition, ionic conductivity, diffusion parameters, microstructure, grain orientations and sizes, surface mechanical properties, area specific resistance, among others. Compiling shared, standardized data-base can accelerate the solid-state battery research by enabling data-driven design strategies. It is proposed that this data-science driven approach can help in identifying new material candidates, understanding underlying physical processes and develop battery management systems for solid-state batteries.

11 Outlook and conclusions

In recent years, *in situ* and *operando* characterization of SSBs have provided significant insights into chemical, mechanical and electrochemical transformation in these material systems. SSB technology has leveraged a large palette of characterization technologies already to investigate length scales ranging from Å to mm scale and time scales from ns to hours. Currently, most characterization techniques are utilized to investigate singular physics of the material system. Extensive reports have shown strong interdependent interplay of chemical, mechanical and electrochemical transformation of materials in SSB systems. One aspect for future consideration is to enable multi-modal characterization that can enable probing binary/ternary interactions at a time in order to accurately characterize the interplay of various physics in SSBs. This can be carried out by employing novel multi-modal characterization techniques already available (AFM-Raman[243], AFM-IR[244], XRT-XANES[245], XRD-XRT[148]) or designing novel characterization tools (viz. pascalammetry)[246]. Additionally, it is vital to investigate material systems under cascading length and time scales in order to extrapolate scientific insight from model investigation systems to actual battery packs.

Several fundamental challenges regarding underlying physics of solid-state batteries are still unsolved. A key challenge is interrogating and probing Li metal processes: in terms of reaction kinetics, mass transport and mechanics: at the physical dimensions relevant to practical solid-state batteries (<100 μm thickness) are not understood well. Stable electrodeposition and electrodissolution of anode at these relevant physical dimensions require a strong understanding of these fundamental mechanisms of Li metal. Interplay of mechanics and transport in bulk solid electrolytes is expected to contribute significantly to degradation mechanism and needs dedicated study. Similarly, the nature of electric field distribution within the solid electrolyte is an open question that needs to be resolved to understand filament formation mechanisms in materials like garnet solid electrolytes. Optimization of composite cathode architecture will require assessing of stability, reaction kinetics and transport across three-phase boundaries within the cathode. While only limited phenomena are highlighted here, it is understood that SSBs offer a rich ground for developing targeted research questions aimed to elucidate fundamental processes and mechanisms occurring therein. These studies are anticipated to generate bottom-up design criteria for stable,

high energy density SSBs. Additionally, studies that look at end-to-end of the battery production line, from synthesis, processing and integration of battery components in a scalable fashion are needed.

It is evident from the discussion here that each method requires careful experimental planning and sample preparation. Based on individual material properties, some techniques are more conducive for certain materials than others and assessing this behavior can help efficient experiment design. Design and sharing of range of experimental set-ups, conditions and protocols can promote standardized testing and lead to consistent, repeatable results. An important factor that needs to be considered during in situ and operando experiment design, is to take into account technologically relevant benchmarks for SSBs in order to facilitate characterization in conditions as close to ideal as possible. Leveraging advanced computational techniques and combining data-driven and physics-driven modelling approaches are expected to generate new insight into the coupled physics of solid-state batteries.

Conflict of Interest

There are no conflicts to declare.

Acknowledgements

K.B.H and M.B.D. acknowledge support from National Science Foundation grant No. 1847029. This research used resources of the Advanced Photon Source, a U.S. Department of Energy (DOE) Office of Science User Facility operated for the DOE Office of Science by Argonne National Laboratory under Contract No. DE-AC02-06CH11357.

References

[1] E. P. Agency, *Inventory of U.S. Greenhouse Gas Emissions and Sinks: 1990-2009*, 36, 2020.

[2] Z. A. Needell, J. McNerney, M. T. Chang and J. E. Trancik, *Nature Energy*, 2016, **1**, 16112.

[3] S. Billimoria, L. Guccione, M. Henchen and L. Louis-Prescott, *Rocky Mountain Institute*, 2018.

[4] S. Nadel and L. Ungar, *ACEEE Report*, 2019.

[5] V. Gowrishankar and A. Levin, *Natural Resources Defense Council*, 2017.

[6] T. T. Mai, P. Jadun, J. S. Logan, C. A. McMillan, M. Muratori, D. C. Steinberg, L. J. Vimmerstedt, B. Haley, R. Jones and B. Nelson, *National Renewable Energy Laboratory*, 2018, 151.

[7] M. Howard, *Electric Power Research Institute*, 2018.

[8] O. M. Løvvik, T. Vegge, W. Wenzel, M. Hahlin, S. Hartmann and A. Latz, *Deliverable 2.1 BATTERY 2030+ Roadmap*, 2019.

[9] A. Thielmann, A. Sauer, R. Isenmann and M. Wietschel, *Fraunhofer Institute for Systems and Innovation Research ISI*, 2013, 32.

[10] I. E. Agency, *Glob. EV Outlook 2020*, 2020.

[11] S. Boyd, *Journal of The Electrochemical Society*, 2018, **165**, A3732–A3737.

[12] D. Howell, B. Cunningham, T. Duong and P. Faguy, *U.S. Dep. Energy Veh. Technol. Off.*, 2016, 24.

[13] D. Parikh, T. Christensen, C.-T. Hsieh and J. Li, *J. Electrochem. Soc.*, 2019, **166**, A3377–A3383.

[14] J. P. Schmidt, T. Chrobak, M. Ender, J. Illig, D. Klotz and E. Ivers-Tiffée, *Journal of Power Sources*, 2011, **196**, 5342–5348.

[15] W. Mai, M. Yang and S. Soghrati, *Electrochimica Acta*, 2019, **294**, 192–209.

[16] K. B. Hatzell, X. C. Chen, C. Cobb, N. P. Dasgupta, M. B. Dixit, L. E. Marbella, M. T. McDowell, P. Mukherjee, A. Verma, V. Viswanathan, A. Westover and W. G. Zeier, *ACS Energy Letters*, 2020, **5**, 922–934.

[17] J. Zheng and Y.-y. Hu, *ACS Applied Materials & Interfaces*, 2018, **10**, 4113–4120.

[18] E. Quartarone and P. Mustarelli, *Chemical Society Reviews*, 2011, **40**, 2525.

[19] T. Famprikis, P. Canepa, J. A. Dawson, M. S. Islam and C. Masquelier, *Nature Materials*, 2019, **18**, 1278–1291.

[20] L. Fan, S. Wei, S. Li, Q. Li and Y. Lu, *Advanced Energy Materials*, 2018, **1702657**, 1–31.

[21] L. Zhang, X. Guo, J. Huang, Y. Qu, C. Niu and Y. Chen, 2018, **6**, 16.

[22] M. Keller, A. Varzi and S. Passerini, *Journal of Power Sources*, 2018, **392**, 206–225.

[23] K. Kerman, A. Luntz, V. Viswanathan, Y.-M. Chiang and Z. Chen, *Journal of The Electrochemical Society*, 2017, **164**, A1731–A1744.

[24] A. Manthiram, X. Yu and S. Wang, *Nature Reviews Materials*, 2017, **2**, 16103.

[25] M. B. Dixit, W. Zaman, Y. Bootwala, Y. Zheng, M. C. Hatzell and K. B. Hatzell, *ACS Applied Materials & Interfaces*, 2019, **11**, 45087–45097.

[26] S. Randau, D. A. Weber, O. Kötz, R. Koerver, P. Braun, A. Weber, E. Ivers-Tiffée, T. Adermann, J. Kulisch, W. G. Zeier, F. H. Richter and J. Janek, *Nature Energy*, 2020, **5**, 259–270.

[27] T. Krauskopf, F. H. Richter, W. G. Zeier and J. Janek, *Chem. Rev.*, 2020, **120**, 7745–7794.

[28] M. Wang, J. B. Wolfenstine and J. Sakamoto, 2019, **296**, 842–847.

[29] J. Kasemchainan, S. Zekoll, D. Spencer Jolly, Z. Ning, G. O. Hartley, T. J. Marrow and P. G. Bruce, *Nature Materials*, 2019, **18**, 1105–1111.

[30] E. Kazyak, R. Garcia-Mendez, W. S. LePage, A. Sharafi, A. L. Davis, A. J. Sanchez, K. H. Chen, C. Haslam, J. Sakamoto and N. P. Dasgupta, *Matter*, 2020, **2**, 1025–1048.

[31] D. Spencer Jolly, Z. Ning, J. E. Darnbrough, J. Kasemchainan, G. O. Hartley, P. Adamson, D. E. Armstrong, J. Marrow and P. G. Bruce, *ACS Applied Materials and Interfaces*, 2020, **12**, 678–685.

[32] A. Sharafi, H. M. Meyer, J. Nanda, J. Wolfenstine and J. Sakamoto, *Journal of Power Sources*, 2016, **302**, 135–139.

[33] J. Tippens, J. C. Miers, A. Afshar, J. A. Lewis, F. J. Q. Cortes, H. Qiao, T. S. Marchese, C. V. Di Leo, C. Saldana and M. T. McDowell, *ACS Energy Letters*, 2019, **4**, 1475–1483.

[34] J. A. Lewis, F. Javier, Q. Cortes, M. G. Boebinger, J. Tippens, T. S. Marchese, N. Kondekar, X. Liu, M. Chi and M. T. Mcdowell, *ACS Energy Letters*, 2019, **4**, 591–599.

[35] N. Singh, J. P. Horwath, P. Bonnick, K. Suto, E. A. Stach, T. Matsunaga, J. Muldoon and T. S. Arthur, *Chemistry of Materials*, 2020, **32**, 7150–7158.

[36] M. Wang and J. Sakamoto, *Journal of Power Sources*, 2018, **377**, 7–11.

[37] W. S. LePage, Y. Chen, E. Kazyak, K.-H. Chen, A. J. Sanchez, A. Poli, E. M. Arruda, M. D. Thouless and N. P. Dasgupta, *Journal of The Electrochemical Society*, 2019, **166**, A89–A97.

[38] J. Lau, R. H. DeBlock, D. M. Butts, D. S. Ashby, C. S. Choi and B. S. Dunn, *Advanced Energy Materials*, 2018, **8**, 1–24.

[39] J. Ma, B. Chen, L. Wang and G. Cui, *Journal of Power Sources*, 2018, **392**, 94–115.

[40] A. N. Mistry and P. P. Mukherjee, *J. Electrochem. Soc.*, 2020, **167**, 082510.

[41] R. Koerver, W. Zhang, L. De Biasi, S. Schweidler, A. O. Kondrakov, S. Kolling, T. Brezesinski, P. Hartmann, W. G. Zeier and J. Janek, *Energy and Environmental Science*, 2018, **11**, 2142–2158.

[42] S. A. Pervez, M. A. Cambaz, V. Thangadurai and M. Fichtner, *ACS Applied Materials and Interfaces*, 2019, **11**, 22029–22050.

[43] X. Ke, Y. Wang, L. Dai and C. Yuan, *Energy Storage Materials*, 2020, **33**, 309–328.

[44] A. Jana and R. E. García, *Nano Energy*, 2017, **41**, 552–565.

[45] L. Frenck, G. K. Sethi, J. A. Maslyn and N. P. Balsara, *Frontiers in Energy Research*, 2019, **7**, 115.

[46] H.-K. Tian, A. Chakraborty, A. A. Talin, P. Eisenlohr and Y. Qi, *Journal of The Electrochemical Society*, 2020, **167**, 090541.

[47] M. Dirican, C. Yan, P. Zhu and X. Zhang, *Materials Science and Engineering R: Reports*, 2019, **136**, 27–46.

[48] K. Nie, Y. Hong, J. Qiu, Q. Li, X. Yu, H. Li and L. Chen, *Frontiers in Chemistry*, 2018, **6**, 1–19.

[49] J. Zhang, K. B. Hatzell and M. C. Hatzell, *Environmental Science and Technology Letters*, 2017, **4**, 470–474.

[50] M. Fingerle, R. Buchheit, S. Sicolo, K. Albe and R. Hausbrand, *Chemistry of Materials*, 2017, **29**, 7675–7685.

[51] J. Haruyama, K. Sodeyama, L. Han, K. Takada and Y. Tateyama, *Chemistry of Materials*, 2014, **26**, 4248–4255.

[52] M. W. Swift and Y. Qi, *Physical Review Letters*, 2019, **122**, 167701.

[53] N. J. J. D. Klerk and M. Wagemaker, *ACS Applied Energy Materials*, 2018, **1**, 5609–5618.

[54] J. S. Park, U. Lienert, P. R. Dawson and M. P. Miller, *Experimental Mechanics*, 2013, **53**, 1491–1507.

[55] Z. Stein, P. Kenesei, J.-S. Park, J. Almer, R. Naraparaju, U. Schulz and S. Raghavan, *Journal of Materials Research*, 2020, **35**, 2300–2310.

[56] D. Liu, Z. Shadike, R. Lin, K. Qian, H. Li, K. Li, S. Wang, Q. Yu, M. Liu, S. Ganapathy, X. Qin, Q. H. Yang, M. Wagemaker, F. Kang, X. Q. Yang and B. Li, *Advanced Materials*, 2019, **1806620**, 1–57.

[57] Y. Xiang, X. Li, Y. Cheng, X. Sun and Y. Yang, *Materials Today*, 2020, **36**, 139–157.

[58] C. Brissot, M. Rosso, J. hazalviel and S. Lascaud, *J. Electrochem. Soc.*, 1999, **146**, 4393–4400.

[59] F. Aguesse, W. Manalastas, L. Buannic, J. M. Lopez del Amo, G. Singh, A. Llordés and J. Kilner, *ACS Apllied Materials & Interfaces*, 2017, **9**, 3808–3816.

[60] L. Porz, T. Swamy, B. W. Sheldon, D. Rettenwander, T. Frömling, H. L. Thaman, S. Berendts, R. Uecker, W. C. Carter and Y. Chiang, *Advanced Energy Materials*, 2017, **7**, 1701003.

[61] C. E. Ren, K. B. Hatzell, M. Alhabeb, Z. Ling, K. A. Mahmoud and Y. Gogotsi, *Journal of Physical Chemistry Letters*, 2015, **6**, 4026–4031.

[62] C. Ma, Y. Cheng, K. Yin, J. Luo, A. Sharafi, J. Sakamoto, J. Li, K. L. More, N. J. Dudney and M. Chi, *Nano letters*, 2016, **16**, 7030–7036.

[63] L. Cheng, E. J. Crumlin, W. Chen, R. Qiao, H. Hou, S. Franz Lux, V. Zorba, R. Russo, R. Kostecki, Z. Liu, K. Persson, W. Yang, J. Cabana, T. Richardson, G. Chen and M. Doeff, *Phys. Chem. Chem. Phys.*, 2014, **16**, 18294–18300.

[64] M. Ebner, F. Geldmacher, F. Marone, M. Stampanoni and V. Wood, *Advanced Energy Materials*, 2013, **3**, 845–850.

[65] Y. Chen, Z. Wang, X. Li, X. Yao, C. Wang, Y. Li, W. Xue, D. Yu, S. Y. Kim, F. Yang, A. Kushima, G. Zhang, H. Huang, N. Wu, Y.-w. Mai, J. B. Goodenough and J. Li, *Nature*, 2020, **578**, 251–255.

[66] Z. Wang, D. Santhanagopalan, W. Zhang, F. Wang, H. L. Xin, K. He, J. Li, N. Dudney and Y. S. Meng, *Nano Letters*, 2016, **16**, 3760–3767.

[67] M. Nagao, A. Hayashi, M. Tatsumisago, T. Kanetsuku, T. Tsuda and S. Kuwabata, *Physical Chemistry Chemical Physics*, 2013, **15**, 18600–18606.

[68] K. Yamamoto, Y. Iriyama, T. Asaka, T. Hirayama, H. Fujita, C. A. J. Fisher, K. Nonaka, Y. Sugita and Z. Ogumi, *Angewandte Chemie - International Edition*, 2010, **49**, 4414–4417.

[69] X. Xu, Y. Liu, J. Wang, D. Isheim, V. P. Dravid, C. Phatak and S. M. Haile, *Nat. Mater.*, 2020, **19**, 887–893.

[70] S. Choi, B. N. Yun, W. D. Jung, T. H. Kim, K. Y. Chung, J. W. Son, B. I. Sang, H. G. Jung and H. Kim, *Scripta Materialia*, 2019, **165**, 10–14.

[71] F. Shen, M. Dixit, X. Xiao and K. Hatzell, *ACS Energy Letters*, 2018, **3**, 1056–1061.

[72] M. B. Dixit, M. Regala, F. Shen, X. Xiao and K. B. Hatzell, *ACS Applied Materials & Interfaces*, 2018, **11**, 2022–2030.

[73] P. R. Shearing, L. E. Howard, P. S. Jørgensen, N. P. Brandon and S. J. Harris, *Electrochemistry Communications*, 2010, **12**, 374–377.

[74] B. Song, I. Dhiman, J. C. Carothers, G. M. Veith, J. Liu, H. Z. Bilheux and A. Huq, *ACS Energy Lett.*, 2019, **4**, 2402–2408.

[75] X. Wang, M. Jiang, Z. Zhou, J. Gou and D. Hui, *Composites Part B: Engineering*, 2017, **110**, 442–458.

[76] F. Walther, R. Koerver, T. Fuchs, S. Ohno, J. Sann, M. Rohnke, W. G. Zeier and J. Janek, *Chem. Mater.*, 2019, **31**, 3745–3755.

[77] F. Han, A. S. Westover, J. Yue, X. Fan, F. Wang, M. Chi, D. N. Leonard, N. J. Dudney, H. Wang and C. Wang, *Nature Energy*, 2019, **4**, 187–196.

[78] L. E. Marbella, S. Zekoll, J. Kasemchainan, P. Emge, P. G. Bruce and C. P. Grey, *Chemistry of Materials*, 2019, **31**, 2762–2769.

[79] M. B. Dixit, W. Zaman, N. Hortance, S. Vujic, B. Harkey, F. Shen, W. Y. Tsai, V. De Andrade, X. C. Chen, N. Balke and K. B. Hatzell, *Joule*, 2020, **4**, 207–221.

[80] F. Sun, M. Osenberg, K. Dong, D. Zhou, A. Hilger, C. J. Jafta, S. Risse, Y. Lu, H. Markötter and I. Manke, *ACS Energy Letters*, 2018, **3**, 356–365.

[81] P. Willmott, *An Introduction to Synchrotron Radiation: Techniques and Applications*, Wiley, Germany, 2011, p. 368.

[82] F. Lin, Y. Liu, X. Yu, L. Cheng, A. Singer, O. G. Shpyrko, H. L. Xin, N. Tamura, C. Tian, T. C. Weng, X. Q. Yang, Y. S. Meng, D. Nordlund, W. Yang and M. M. Doeff, *Chemical Reviews*, 2017, **117**, 13123–13186.

[83] R. M. Leahy, R. Clackdoyle and F. Noo, *The Essential Guide to Image Processing*, 2009, pp. 741–776.

[84] M. B. Dixit, A. Verma, W. Zaman, X. Zhong, P. Kenesei, J. S. Park, J. Almer, P. P. Mukherjee and K. B. Hatzell, *ACS Applied Energy Materials*, 2020, **3**, 9534–9542.

[85] M. B. Dixit, N. Singh, J. P. Horwath, P. D. Shevchenko, M. Jones, E. A. Stach, T. S. Arthur and K. B. Hatzell, *Matter*, 2020, **3**, 2138–2159.

[86] W. Zaman, N. Hortance, M. B. Dixit, V. De Andrade and K. B. Hatzell, *Journal of Materials Chemistry A*, 2019, **7**, 23914–23921.

[87] Z. Li, K. Jiang, F. Khan, A. Goswami, J. Liu, A. Passian and T. Thundat, *Sci. Adv.*, 2019, **5**, 1–9.

[88] W. A. Paxton, E. K. Akdoan, I. Sąvkliyildiz, A. U. Choksi, S. X. Silver, T. Tsakalakos and Z. Zhong, *Journal of Materials Research*, 2015, **30**, 417–423.

[89] D. P. Finegan, A. Vamvakeros, C. Tan, T. M. Heenan, S. R. Daemi, N. Seitzman, M. Di Michiel, S. Jacques, A. M. Beale, D. J. Brett, P. R. Shearing and K. Smith, *Nature Communications*, 2020, **11**, 1–11.

[90] K. C. Kirshenbaum, D. C. Bock, A. B. Brady, A. C. Marschilok, K. J. Takeuchi and E. S. Takeuchi, *Physical Chemistry Chemical Physics*, 2015, **17**, 11204–11210.

[91] T. Matsuyama, M. Deguchi, K. Mitsuhara, T. Ohta, T. Mori, Y. Orikasa, Y. Uchimoto, Y. Kowada, A. Hayashi and M. Tatsumisago, *Journal of Power Sources*, 2016, **313**, 104–111.

[92] A. T. S. Freiberg, A. Siebel, A. Berger, S. M. Webb, Y. Gorlin, M. Tromp and H. Gasteiger, *The Journal of Physical Chemistry C*, 2018, **122**, 5303–5316.

[93] S. M. Bak, Z. Shadike, R. Lin, X. Yu and X. Q. Yang, *NPG Asia Materials*, 2018, **10**, 563–580.

[94] V. Shutthanandan, M. Nandasiri, J. Zheng, M. H. Engelhard, W. Xu, S. Thevuthasan and V. Murugesan, *Applications of XPS in the Characterization of Battery Materials*, 2019.

[95] Y.-C. Lu, E. J. Crumlin, G. M. Veith, J. R. Harding, E. Mutoro, L. Baggetto, N. J. Dudney, Z. Liu and Y. Shao-Horn, *Scientific Reports*, 2012, **2**, 715.

[96] Y. Kimura, M. Fakkao, T. Nakamura, T. Okumura, N. Ishiguro, O. Sekizawa, K. Nitta, T. Uruga, M. Tada, Y. Uchimoto and K. Amezawa, *ACS Applied Energy Materials*, 2020, 7782–7793.

[97] T. Liu, Y. Zhang, R. Chen, S. X. Zhao, Y. Lin, C. W. Nan and Y. Shen, *Electrochemistry Communications*, 2017, **79**, 1–4.

[98] C. Masquelier, *European Physical Journal: Special Topics*, 2012, **213**, 213–224.

[99] T. Thompson, J. Wolfenstine, J. L. Allen, M. Johannes, A. Huq, I. N. David and J. Sakamoto, *Journal of Materials Chemistry A*, 2014, **2**, 13431–13436.

[100] B. K. Annis, Y. S. Badyal and J. M. Simonson, *Journal of Physical Chemistry B*, 2004, **108**, 2554–2556.

[101] J. Lefevr, L. Cervini, J. M. Griffin and D. Blanchard, *Journal of Physical Chemistry C*, 2018, **122**, 15264–15275.

[102] J. Wind, R. A. Mole, D. Yu and C. D. Ling, *Chemistry of Materials*, 2017, **29**, 7408–7415.

[103] W. Zhou, S. Wang, Y. Li, S. Xin, A. Manthiram and J. B. Goodenough, *Journal of the American Chemical Society*, 2016, **138**, 9385–9388.

[104] J. B. Siegel, X. Lin, A. G. Stefanopoulou, D. S. Hussey, D. L. Jacobson and D. Gorsich, *Journal of The Electrochemical Society*, 2011, **158**, A523.

[105] J. E. Owejan, J. P. Owejan, S. C. Decaluwe and J. A. Dura, *Chemistry of Materials*, 2012, **24**, 2133–2140.

[106] H. Schmidt, B. Jerliu, E. Hüger and J. Stahn, *Electrochemistry Communications*, 2020, **115**, 106738.

[107] M. V. Avdeev, A. A. Rulev, E. E. Ushakova, Y. N. Kosiachkin, V. I. Petrenko, I. V. Gapon, E. Y. Kataev, V. A. Matveev, L. V. Yashina and D. M. Itkis, *Applied Surface Science*, 2019, **486**, 287–291.

[108] A. Ronneburg, M. Trapp, R. Cubitt, L. Silvi, S. Cap, M. Ballauff and S. Risse, *Energy Storage Materials*, 2019, **18**, 182–189.

[109] S. Whitney, S. R. Biegalski, Y. H. Huang and J. B. Goodenough, *Journal of the Electrochemical Society*, 2009, **156**, 886–890.

[110] J. F. Oudenhoven, F. Labohm, M. Mulder, R. A. Niessen, F. M. Mulder and P. H. Notten, *Advanced Materials*, 2011, **23**, 4103–4106.

[111] J. Liu, J. Zhou, M. Wang, C. Niu, T. Qian and C. Yan, *J. Mater. Chem. A*, 2019, **7**, 24477–24485.

[112] W. Manalastas, J. Rikarte, R. J. Chater, R. Brugge, A. Aguadero, L. Buannic, A. Llordés, F. Aguesse and J. Kilner, *J. Power Sources*, 2019, **412**, 287–293.

[113] M. Rosso, C. Brissot, A. Teyssot, M. Dollé, L. Sannier, J. M. Tarascon, R. Bouchet and S. Lascaud, *Electrochim. Acta*, 2006, **51**, 5334–5340.

[114] F. Sagane, R. Shimokawa, H. Sano, H. Sakaebe and Y. Iriyama, *J. Power Sources*, 2013, **225**, 245–250.

[115] C. Brissot, M. Rosso, J. N. Chazalviel, P. Baudry and S. Lascaud, *Electrochim. Acta*, 1998, **43**, 1569–1574.

[116] M. Rosso, T. Gobron, C. Brissot, J. N. Chazalviel and S. Lascaud, *J. Power Sources*, 2001, **97-98**, 804–806.

[117] C. Brissot, M. Rosso, J. N. Chazalviel and S. Lascaud, *Stud. Surf. Sci. Catal.*, 2001, **132**, 947–952.

[118] C. Brissot, M. Rosso, J. N. Chazalviel and S. Lascaud, *J. Power Sources*, 2001, **94**, 212–218.

[119] W. S. Kim and W. Y. Yoon, *Electrochim. Acta*, 2004, **50**, 541–545.

[120] M. Golozar, A. Paolella, H. Demers, S. Bessette, M. Lagacé, P. Bouchard, A. Guerfi, R. Gauvin and K. Zaghib, *Commun. Chem.*, 2019, **2**, 1–9.

[121] R. Koerver, I. Aygün, T. Leichtweiß, C. Dietrich, W. Zhang, J. O. Binder, P. Hartmann, W. G. Zeier and J. Janek, *Chemistry of Materials*, 2017, **29**, 5574–5582.

[122] S. Ohno, R. Koerver, G. Dewald, C. Rosenbach, P. Titscher, D. Steckermeier, A. Kwade, J. Janek and W. G. Zeier, *Chemistry of Materials*, 2019, **31**, 2930–2940.

[123] S. Lou, Z. Yu, Q. Liu, H. Wang, M. Chen and J. Wang, *Chem*, 2020, **6**, 2199–2218.

[124] D. H. Tan, A. Banerjee, Z. Chen and Y. S. Meng, *Nat. Nanotechnol.*, 2020, **15**, 170–180.

[125] Y. Zhang, Y. Shi, X. C. Hu, W. P. Wang, R. Wen, S. Xin and Y. G. Guo, *Adv. Energy Mater.*, 2020, **10**, 1–8.

[126] W. b. d. Tang, B.-M. b. Goh, M. Hu, C. Wan, B. b. Tian, X. Deng, C. b. Peng, M. Lin, J. Hu and K. b. Loh, *Journal of Physical Chemistry C*, 2016, **120**, 2600–2608.

[127] S. H. Kim, K. H. Kim, H. Choi, D. Im, S. Heo and H. S. Choi, *Journal of Materials Chemistry A*, 2019, **7**, 13650–13657.

[128] L. Sang, R. T. Haasch, A. A. Gewirth and R. G. Nuzzo, *Chemistry of Materials*, 2017, **29**, 3029–3037.

[129] M. Dollé, L. Sannier, B. Beaudoin, M. Trentin and J. M. Tarascon, *Electrochem. Solid-State Lett.*, 2002, **5**, A286.

[130] H. Marceau, C. S. Kim, A. Paolella, S. Ladouceur, M. Lagacé, M. Chaker, A. Vijh, A. Guerfi, C. M. Julien, A. Mauger, M. Armand, P. Hovington and K. Zaghib, *J. Power Sources*, 2016, **319**, 247–254.

[131] T. Krauskopf, H. Hartmann, F. H. Richter, G. Wolfgang, T. Krauskopf, R. Dippel, H. Hartmann, K. Peppler, B. Mogwitz, F. H. Richter and W. G. Zeier, *Joule*, 2019, **3**, 2030–2049.

[132] W. Zhang, F. H. Richter, S. P. Culver, T. Leichtweiss, J. G. Lozano, C. Dietrich, P. G. Bruce, W. G. Zeier and J. Janek, *ACS Applied Materials and Interfaces*, 2018, **10**, 22226–22236.

[133] M. M. Besli, S. Xia, S. Kuppan, Y. Huang, M. Metzger, A. K. Shukla, G. Schneider, S. Hellstrom, J. Christensen, M. M. Doeff and Y. Liu, *Chemistry of Materials*, 2019, **31**, 491–501.

[134] K. H. Choi, D. B. Ahn and S. Y. Lee, *ACS Energy Letters*, 2018, **3**, 220–236.

[135] Z. Wang, J. Z. Lee, H. L. Xin, L. Han, N. Grillon, D. Guy-bouyssou, E. Bouyssou, M. Proust and Y. Shirley, *Journal of Power Sources*, 2016, **324**, 342–348.

[136] G. Vardar, W. J. Bowman, Q. Lu, J. Wang, R. J. Chater, A. Aguadero, R. Seibert, J. Terry, A. Hunt, I. Waluyo, D. D. Fong, A. Jarry, E. J. Crumlin, S. L. Hellstrom, Y. M. Chiang and B. Yildiz, *Chem. Mater.*, 2018, **30**, 6259–6276.

[137] Z. Wang, D. Santhanagopalan, W. Zhang, F. Wang, H. L. Xin, K. He, J. Li, N. Dudney and Y. S. Meng, *Nano Letters*, 2016, **16**, 3760–3767.

[138] Y. Gong, J. Zhang, L. Jiang, J. A. Shi, Q. Zhang, Z. Yang, D. Zou, J. Wang, X. Yu, R. Xiao, Y. S. Hu, L. Gu, H. Li and L. Chen, *J. Am. Chem. Soc.*, 2017, **139**, 4274–4277.

[139] C. Fu, V. Venturi, J. Kim, Z. Ahmad, A. W. Ells, V. Viswanathan and B. A. Helms, *Nature Materials*, 2020, **19**, 758–766.

[140] C. Masquelier, *Nature Publishing Group*, 2011, **10**, 649–650.

[141] X. Xu, C. Carr, X. Chen, B. D. Myers, R. Huang, W. Yuan, S. Choi, D. Yi, C. Phatak and S. M. Haile, *Adv. Energy Mater.*, 2021, **2003309**, 2003309.

[142] S. Kaboli, P. Noel, D. Clément, H. Demers, A. Paolella, P. Bouchard, M. L. Trudeau, J. B. Goodenough and K. Zaghib, *Sci. Adv.*, 2020, **6**, 1–9.

[143] G. Yan, S. Yu, W. Yang, X. Li, H. Tempel, H. Kungl, R. A. Eichel, M. Krüger and J. Malzbender, *J. Power Sources*, 2019, **437**, 226940.

[144] M. B. Dixit, D. Moreno, X. Xiao, M. C. Hatzell and K. B. Hatzell, *ACS Materials Letters*, 2019, **1**, 71–76.

[145] N. Seitzman, H. Guthrey, D. B. Sulas, H. A. S. Platt, M. Al-Jassim and S. Pylypenko, *Journal of The Electrochemical Society*, 2018, **165**, A3732–A3737.

[146] R. Haas, C. Pompe, M. Osenberg, I. Manke, U. Maitra and D. Langsdorf, *Energy Technology*, 2019, **7**, 1801146.

[147] W. Zhang, D. Schröder, T. Arlt, I. Manke, R. Koerver, R. Pinedo, D. A. Weber, J. Sann, W. G. Zeier and J. Janek, *Journal of Materials Chemistry A*, 2017, **5**, 9929–9936.

[148] J. M. Doux, H. Nguyen, D. H. Tan, A. Banerjee, X. Wang, E. A. Wu, C. Jo, H. Yang and Y. S. Meng, *Advanced Energy Materials*, 2020, **10**, 1903253.

[149] M. Kodama, S. Komiyama, A. Ohashi, N. Horikawa, K. Kawamura and S. Hirai, *Journal of Power Sources*, 2020, **462**, 228160.

[150] W. Zhang, D. Schröder, T. Arlt, I. Manke, R. Koerver, R. Pinedo, D. A. Weber, J. Sann, W. G. Zeier and J. Janek, *Journal of Materials Chemistry A*, 2017, **5**, 9929–9936.

[151] K. Kandori, H. Yamashige, N. Furuta, T. Nonaka and Y. Orikasa, *Electrochemistry*, 2019, **87**, 182–187.

[152] F. Hao and P. P. Mukherjee, *Journal of The Electrochemical Society*, 2018, **165**, A1857–A1864.

[153] Q. Tu, L. Barroso-Luque, T. Shi and G. Ceder, *Cell Reports Physical Science*, 2020, **1**, 100106.

[154] H.-K. Tian and Y. Qi, *Journal of The Electrochemical Society*, 2017, **164**, E3512–E3521.

[155] S. Narayan and L. Anand, *Journal of The Electrochemical Society*, 2020, **167**, 040525.

[156] X. Wu, J. Billaud, I. Jerjen, F. Marone, Y. Ishihara, Y. Adachi, C. Villevieille and Y. Kato, *Advanced Energy Materials*, 2019, **9**, 1901547.

[157] K. E. Madsen, K. L. Bassett, K. Ta, B. A. Sforzo, K. E. Matusik, A. L. Kastengren and A. A. Gewirth, *Adv. Mater. Interfaces*, 2020, **7**, 1–12.

[158] T. Li, H. Kang, X. Zhou, C. Lim, B. Yan, V. De Andrade, F. De Carlo and L. Zhu, *ACS Applied Materials and Interfaces*, 2018, **10**, 16927–16931.

[159] K. R. Adair, M. N. Banis, Y. Zhao, T. Bond, R. Li and X. Sun, *Advanced Materials*, 2020, **32**, 2002550.

[160] A. Neumann, S. Randau, K. Becker-Steinberger, T. Danner, S. Hein, Z. Ning, J. Marrow, F. H. Richter, J. Janek and A. Latz, *ACS Applied Materials and Interfaces*, 2020, **12**, 9277–9291.

[161] H. Li, M. Li, S. H. Siyal, M. Zhu, J. L. Lan, G. Sui, Y. Yu, W. Zhong and X. Yang, *Journal of Membrane Science*, 2018, **555**, 169–176.

[162] H. Shen, E. Yi, M. Amores, L. Cheng, N. Tamura, D. Y. Parkinson, G. Chen, K. Chen and M. Doeff, *Journal of Materials Chemistry A*, 2019, **7**, 20861–20870.

[163] M. Liu, C. Wang, Z. Cheng, S. Ganapathy, L. A. Haverkate, S. Unnikrishnan and M. Wagemaker, *ACS Materials Letters*, 2020, 665–670.

[164] C. Chen, J. F. Oudenhoven, D. L. Danilov, E. Vezhlev, L. Gao, N. Li, F. M. Mulder, R. A. Eichel and P. H. Notten, *Advanced Energy Materials*, 2018, **8**, 1801430.

[165] D. L. Danilov, C. Chen, M. Jiang, R. A. Eichel and P. H. Notten, *Radiation Effects and Defects in Solids*, 2020, **175**, 367–382.

[166] X. Han, Y. Gong, K. Fu, X. He, G. T. Hitz, J. Dai, A. Pearse, B. Liu, H. Wang, G. Rubloff, Y. Mo, V. Thangadurai, E. D. Wachsman and L. Hu, *Nature Materials*, 2017, **16**, 572–579.

[167] L. Chen, Y. Li, S. P. Li, L. Z. Fan, C. W. Nan and J. B. Goodenough, *Nano Energy*, 2018, **46**, 176–184.

[168] S. Kim, C. Jung, H. Kim, K. E. Thomas-Alyea, G. Yoon, B. Kim, M. E. Badding, Z. Song, J. M. Chang, J. Kim, D. Im and K. Kang, *Adv. Energy Mater.*, 2020, **10**, 1–11.

[169] Z. Zhao, Z. Wen, X. Liu, H. Yang, S. Chen, C. Li, H. Lv, F. Wu, B. Wu and D. Mu, *Chem. Eng. J.*, 2021, **405**, 127031.

[170] C. S. Jiang, N. Dunlap, Y. Li, H. Guthrey, P. Liu, S. H. Lee and M. M. Al-Jassim, *Adv. Energy Mater.*, 2020, **10**, 1–10.

[171] Q. Sun, L. He, F. Zheng, Z. Wang, S. J. An Oh, J. Sun, K. Zhu, L. Lu and K. Zeng, *J. Power Sources*, 2020, **471**, 1–9.

[172] Y. Zhou, C. Doerrer, J. Kasemchainan, P. G. Bruce, M. Pasta and L. Hardwick, *Batter. Supercaps*, 2020, 647–652.

[173] I. Tomandl, J. Vacik, T. Kobayashi, Y. Mora Sierra, V. Hnatowicz, V. Lavreniev, P. Horak, G. Ceccio, A. Cannavo, M. Baba and R. Ye, *Radiation Effects and Defects in Solids*, 2020, **175**, 394–405.

[174] J. Zhu, L. Lu and K. Zeng, *ACS Nano*, 2013, **7**, 1666–1675.

[175] Y. Tian, Y. Sun, D. C. Hannah, Y. Xiao, H. Liu, K. W. Chapman, S. H. Bo and G. Ceder, *Joule*, 2019, **3**, 1037–1050.

[176] S. Shiotani, K. Ohara, H. Tsukasaki, S. Mori and R. Kanno, *Scientific Reports*, 2017, **7**, 6972.

[177] T. Bartsch, A. Y. Kim, F. Strauss, L. De Biasi, J. H. Teo, J. Janek, P. Hartmann and T. Brezesinski, *Chemical Communications*, 2019, **55**, 11223–11226.

[178] H. Wang, M. Yu, Y. Wang, Z. Feng, Y. Wang, X. Lü, J. Zhu, Y. Ren and C. Liang, *Journal of Power Sources*, 2018, **401**, 111–116.

[179] R. P. Rao, N. Sharma, V. K. Peterson and S. Adams, *Solid State Ionics*, 2013, **230**, 72–76.

[180] H. Tsukasaki, T. Uchiyama, K. Yamamoto, S. Mori, Y. Uchimoto, H. Kowada, A. Hayashi and M. Tatsumisago, *Journal of Power Sources*, 2019, **434**, 226714.

[181] L. Cheng, W. Chen, M. Kunz, K. Persson, N. Tamura, G. Chen and M. Doeff, *ACS Applied Materials & Interfaces*, 2015, **7**, 2073–2081.

[182] H. Kawasoko, T. Shirasawa, S. Shiraki, T. Suzuki, S. Kobayashi, K. Nishio, R. Shimizu and T. Hitosugi, *ACS Applied Energy Materials*, 2020, **3**, 1358–1363.

[183] S. Shiraki, T. Shirasawa, T. Suzuki, H. Kawasoko, R. Shimizu and T. Hitosugi, *ACS Applied Materials and Interfaces*, 2018, **10**, 41732–41737.

[184] D. Goonetilleke, N. Sharma, J. Kimpton, J. Galipaud, B. Pecquenard and F. Le Cras, *Frontiers in Energy Research*, 2018, **6**, 1–9.

[185] T. Asano, A. Sakai, S. Ouchi, M. Sakaida, A. Miyazaki and S. Hasegawa, *Advanced Materials*, 2018, **30**, 1803075.

[186] J. R. Nykaza, A. M. Savage, Q. Pan, S. Wang, F. L. Beyer, M. H. Tang, C. Y. Li and Y. A. Elabd, *Polymer*, 2016, **101**, 311–318.

[187] A. Agrawal, S. Choudhury and L. A. Archer, *RSC Advances*, 2015, **5**, 20800–20809.

[188] T. C. Mendes, N. Goujon, N. Malic, A. Postma, J. Chiefari, H. Zhu, P. C. Howlett and M. Forsyth, *Journal of The Electrochemical Society*, 2020, **167**, 070525.

[189] H. M. Kao and C. L. Chen, *Angewandte Chemie - International Edition*, 2004, **43**, 980–984.

[190] P. E. Trapa, Y.-Y. Won, S. C. Mui, E. A. Olivetti, B. Huang, D. R. Sadoway, A. M. Mayes and S. Dallek, *Journal of The Electrochemical Society*, 2005, **152**, A1.

[191] S. Wenzel, T. Leichtweiss, D. Krüger, J. Sann and J. Janek, *Solid State Ionics*, 2015, **278**, 98–105.

[192] S. Wenzel, S. Randau, T. Leichtweiß, D. A. Weber, J. Sann, W. G. Zeier and J. Janek, *Chemistry of Materials*, 2016, **28**, 2400–2407.

[193] A. Sharafi, C. G. Haslam, R. D. Kerns, J. Wolfenstine and J. Sakamoto, *Journal of Materials Chemistry A*, 2017, **5**, 21491–21504.

[194] M. Cheng, Y. Jiang, W. Yao, Y. Yuan, R. Deivanayagam, T. Foroozan, Z. Huang, B. Song, R. Rojaee, T. Shokuhfar, Y. Pan, J. Lu and R. Shahbazian-Yassar, *Advanced Materials*, 2018, **30**, 1800615.

[195] S. Wenzel, S. Randau, T. Leichtweiß, D. A. Weber, J. Sann, W. G. Zeier and J. Janek, *Chemistry of Materials*, 2016, **28**, 2400–2407.

[196] T. Takeuchi, H. Kageyama, K. Nakanishi, T. Ohta, A. Sakuda, T. Sakai, H. Kobayashi, H. Sakaebe, K. Tatsumi and Z. Ogumi, *Solid State Ionics*, 2014, **262**, 138–142.

[197] Y. Zheng, M. Hirayama, S. Taminato, S. Lee, Y. Oshima, K. Takayanagi, K. Suzuki and R. Kanno, *Journal of Power Sources*, 2015, **300**, 413–418.

[198] X. Li, Z. Ren, M. Norouzi Banis, S. Deng, Y. Zhao, Q. Sun, C. Wang, X. Yang, W. Li, J. Liang, X. Li, Y. Sun, K. Adair, R. Li, Y. Hu, T. K. Sham, H. Huang, L. Zhang, S. Lu, J. Luo and X. Sun, *ACS Energy Lett.*, 2019, **4**, 2480–2488.

[199] C. Yu, S. Ganapathy, E. R. Eck, H. Wang, S. Basak, Z. Li and M. Wagemaker, *Nat. Commun.*, 2017, **8**, 1–9.

[200] P. H. Chien, X. Feng, M. Tang, J. T. Rosenberg, S. O'Neill, J. Zheng, S. C. Grant and Y. Y. Hu, *J. Phys. Chem. Lett.*, 2018, **9**, 1990–1998.

[201] P. H. Chien, K. J. Griffith, H. Liu, Z. Gan and Y. Y. Hu, *Annu. Rev. Mater. Res.*, 2020, **50**, 493–520.

[202] G. J. Rees, D. S. Jolly, Z. Ning, J. Marrow, G. Pavlovskaya and P. G. Bruce, *Angew. Chemie Int. Ed.*, 2020, 2138–2143.

[203] M. Otoyama, Y. Ito, A. Hayashi and M. Tatsumisago, *J. Power Sources*, 2016, **302**, 419–425.

[204] X. Li, X. Li, J. Liang, C. Wang, J. Luo, R. Li and X. Sun, *Energy Environ. Sci.*, 2018, **11**, 2828–2832.

[205] J. Zhang, C. Zheng, L. Li, Y. Xia, H. Huang, Y. Gan, C. Liang, X. He, X. Tao and W. Zhang, *Adv. Energy Mater.*, 2020, **10**, 1–12.

[206] Y. Matsuda, N. Kuwata, T. Okawa, A. Dorai, O. Kamishima and J. Kawamura, *Solid State Ionics*, 2019, **335**, 7–14.

[207] H. Gao, S. Xin, L. Xue and J. B. Goodenough, *Chem*, 2018, **4**, 833–844.

[208] R. D. Schmidt and J. Sakamoto, *J. Power Sources*, 2016, **324**, 126–133.

[209] S. Choi, B.-n. Yun, W. Dum, T. Hyun, K.-y. Chung, J.-w. Son, B.-i. Sang, H.-g. Jung and H. Kim, *Scr. Mater.*, 2019, **165**, 10–14.

[210] K. Park, B. C. Yu, J. W. Jung, Y. Li, W. Zhou, H. Gao, S. Son and J. B. Goodenough, *Chem. Mater.*, 2016, **28**, 8051–8059.

[211] F. J. Simon, M. Hanauer, A. Henss, F. H. Richter and J. Janek, *ACS Appl. Mater. Interfaces*, 2019, **11**, 42186–42196.

[212] X. Wu, Y. Zhang, J. Zhang, R. Liu, J. Yang, B. Yang, H. Xu and Y. Ma, *Journal of Alloys and Compounds*, 2020, **823**, 153793.

[213] P. Hofmann, F. Walther, M. Rohnke, J. Sann, W. G. Zeier and J. Janek, *Solid State Ionics*, 2019, **342**, 115054.

[214] R. Pfenninger, M. Struzik, I. Garbayo, E. Stilp and J. L. Rupp, *Nat. Energy*, 2019, **4**, 475–483.

[215] J. Liang, X. Li, Y. Zhao, L. V. Goncharova, W. Li, K. R. Adair, M. N. Banis, Y. Hu, T. K. Sham, H. Huang, L. Zhang, S. Zhao, S. Lu, R. Li and X. Sun, *Advanced Energy Materials*, 2019, **9**, 1–10.

[216] X. G. Yang, T. Liu, Y. Gao, S. Ge, Y. Leng, D. Wang and C. Y. Wang, *Joule*, 2019, **3**, 3002–3019.

[217] R. H. Brugge, F. M. Pesci, A. Cavallaro, C. Sole, M. A. Isaacs, G. Kerherve, R. S. Weatherup and A. Aguadero, *J. Mater. Chem. A*, 2020, **8**, 14265–14276.

[218] H. Masuda, N. Ishida, Y. Ogata, D. Ito and D. Fujita, *J. Power Sources*, 2018, **400**, 527–532.

[219] J. Sastre, X. Chen, A. Aribia, A. N. Tiwari and Y. E. Romanyuk, *ACS Appl. Mater. Interfaces*, 2020, **12**, 36196–36207.

[220] Z. Wang, M. Kotobuki, L. Lu and K. Zeng, *Electrochim. Acta*, 2020, **334**, 1–8.

[221] K. Morita, B. Tsuchiya, H. Tsuchida and T. Majima, *Solid State Ionics*, 2020, **344**, 115135.

[222] B. Tsuchiya, J. Ohnishi, Y. Sasaki, T. Yamamoto, Y. Yamamoto, M. Motoyama, Y. Iriyama and K. Morita, *Advanced Materials Interfaces*, 2019, **6**,.

[223] K. Yamamoto, Y. Iriyama and T. Hirayama, *Microscopy*, 2017, 50–61.

[224] K. Yamamoto, Y. Iriyama, T. Asaka, T. Hirayama, H. Fujita, K. Nonaka, K. Miyahara, Y. Sugita and Z. Ogumi, *Electrochem. commun.*, 2012, **20**, 113–116.

[225] Y. Aizawa, K. Yamamoto, T. Sato, H. Murata, R. Yoshida, C. A. Fisher, T. Kato, Y. Iriyama and T. Hirayama, *Ultramicroscopy*, 2017, **178**, 20–26.

[226] N. Martensson and M. Eriksson, *Nuclear Instruments and Methods in Physics Research Section A: Accelerators, Spectrometers, Detectors and Associated Equipment*, 2018, **907**, 97–104.

[227] P. F. Tavares, E. Al-Dmour, Å. Andersson, F. Cullinan, B. N. Jensen, D. Olsson, D. K. Olsson, M. Sjöström, H. Tarawneh, S. Thorin and A. Vorozhtsov, *Journal of Synchrotron Radiation*, 2018, **25**, 1291–1316.

[228] P. F. Tavares, S. C. Leemann, M. Sjöström and Å. Andersson, *Journal of Synchrotron Radiation*, 2014, **21**, 862–877.

[229] D. H. Cho, Z. Shen, Y. Ihm, D. H. Wi, C. Jung, D. Nam, S. Kim, S.-Y. Park, K. S. Kim, D. Sung, H. Lee, J.-Y. Shin, J. Hwang, S. Y. Lee, S. Y. Lee, S. W. Han, D. Y. Noh, N. D. Loh and C. Song, *ACS Nano*, 2021, **15**, 4066–4076.

[230] R. Ballabriga, J. Alozy, F. N. Bandi, M. Campbell, N. Egidos, J. M. Fernandez-Tenllado, E. H. M. Heijne, I. Kremastiotis, X. Llopart, B. J. Madsen, D. Pennicard, V. Sriskaran and L.Tlustos, *IEEE Transactions on Radiation and Plasma Medical Sciences*, 2020, 1–1.

[231] R. V. Martins, C. Ohms and K. Decroos, *Materials Science and Engineering A*, 2010, **527**, 4779–4787.

[232] D. R. Haeffner, J. D. Almer and U. Lienert, *Materials Science and Engineering A*, 2005, **399**, 120–127.

[233] S. F. Nielsen, A. Wolf, H. F. Poulsen, M. Ohler, U. Lienert and R. A. Owen, *Journal of Synchrotron Radiation*, 2000, **7**, 103–109.

[234] V. Honkimäki and P. Suortti, *J Synchrotron Radiat*, 2007, **14**, 331–338.

[235] K. P. C. Yao, J. S. Okasinski, K. Kalaga, I. A. Shkrob and D. P. Abraham, *Energy Environ. Sci.*, 2019, **12**, 656–665.

[236] U. Lienert, J. Lind, C. M. Hefferan, W. Pantleon, M. J. Mills, M. P. Miller, R. M. Suter, S. F. Li, M. C. Brandes, J. V. Bernier, B. Jakobsen and N. R. Barton, *JOM*, 2011, **63**, 70–77.

[237] R. M. Suter, D. Hennessy, C. Xiao and U. Lienert, *Review of Scientific Instruments*, 2006, **77**, 123905.

[238] M. E. Birkbak, H. Leemreize, S. Frølich, S. R. Stock and H. Birkedal, *Nanoscale*, 2015, **7**, 18402–18410.

[239] M. Lvarez-Murga, P. Bleuet and J. L. Hodeau, *Journal of Applied Crystallography*, 2012, **45**, 1109–1124.

[240] D. P. Finegan, A. Vamvakeros, L. Cao, C. Tan, T. M. Heenan, S. R. Daemi, S. D. Jacques, A. M. Beale, M. Di Michiel, K. Smith, D. J. Brett, P. R. Shearing and C. Ban, *Nano Letters*, 2019, **19**, 3811–3820.

[241] X. Zhang, C. Xu, Y. Chen, W.-Y. Chen, J.-S. Park, P. Kenesei, J. Almer, J. Burns, Y. Wu and M. Li, *Acta Materialia*, 2020, **200**, 315–327.

[242] O. Schmidt, E. Benda, D. Capatina, T. Clute, J. Collins, M. Erdmann, T. Graber, D. Haeffner, Y. Jaski, J. Knopp, G. Navrotski, R. Winarski and L. Beamlines, 10th Mech. Eng. Des. Synchrotron Radiat. Equip. Instrum., 2018, pp. 324–326.

[243] J. P. C. Fernandes, V. H. Mareau and L. Gonon, *International Journal of Polymer Analysis and Characterization*, 2018, **23**, 113–119.

[244] A. Dazzi and C. B. Prater, *Chemical Reviews*, 2017, **117**, 5146–5173.

[245] J. Conder, C. Marino, P. Novák and C. Villevieille, *Journal of Materials Chemistry A*, 2018, **6**, 3304–3327.

[246] J. M. Larson, E. Gillette, K. Burson, Y. Wang, S. B. Lee and J. E. Reutt-Robey, *Sci. Adv.*, 2018, **4**, 1–10.